FREQUENCY CONTROL, MODELING, ALIGNMENT ADAPTATION, AND SAFETY CONCERNS FOR THE WIRELESS CHARGING OF ELECTRIC VEHICLES

by

YABIAO GAO

(Under the Direction of Zion Tsz Ho Tse)

ABSTRACT

Wireless power transfer (WPT) is a promising way to reduce the inconvenience of electric vehicle (EV) charging, which has been considered one of the major issues hindering widespread adoption of EVs. This dissertation includes four parts aiming to solve key issues associated with control, modeling, misalignment and safety concerns of wireless EV charging.

Part 1 of this dissertation addresses the output voltage variation and efficiency drop caused by misalignment; a uniform voltage gain control for a series–parallel resonant converter is implemented to improve the alignment robustness of wireless chargers. The uniform gain control is achieved by analyzing the voltage gain and impedance across the frequency domain, and an embedded program is developed to tune the switching frequency for a stable output voltage based on phase angle feedback of the primary inverter. Experimental results show that the efficiency of fixed frequency control dropped from 82% to 34% when the misalignment was changed from 0 to 200 mm, while the efficiency of uniform gain control dropped from 81% to 60%.

Part 2 of this dissertation describes modeling a series–series topology WPT system for maximum power transmission efficiency. A frequency-spacing model is proposed to calculate the unity-gain switching frequency when the coil geometry and displacements are known. The experimental results show that the unity-gain frequency can be predicted with varying loads and air gaps (75mm to 250mm), and a demonstrated unity-gain error of <6%.

Part 3 of this dissertation introduces a parking alignment system for wireless EV chargers. The alignment detection system is low cost because it uses the existing charging facility and only four auxiliary coils to determine the direction and magnitude of required parking adjustments. An alignment system for wireless EV chargers should be a fundamental approach to solve the misalignment issues in EV wireless charging by making it easy for the EV driver to park properly. The coil positioning accuracy of the system is <3cm.

Part 4 of the dissertation investigates safety concerns regarding exposure to strong electromagnetic (EM) fields present during WPT. The body of work examines that a metal debris placed on the primary pad have a temperature rise of 81℃ under 3.1kW WPT, and the EM field between the two charging pads can reach 1.656 mT, which largely exceeds the safety guideline imposed by the ICNIRP standard.

The methodology of this work can provide a fundamental theory that allows for efficient, robust, and safe wireless EV charging.

INDEX WORDS: Wireless Power Transfer, Inductive Power Transfer, Wireless Charging, Electric Vehicles, Vehicle Alignment, Controls, Modeling, Resonant Converter, Magnetic Coupler, Magnetic Emissions, Safety Concerns.

FREQUENCY CONTROL, MODELING, ALIGNMENT ADAPTATION, AND SAFETY CONCERNS FOR THE WIRELESS CHARGING OF ELECTRIC VEHICLES

by

YABIAO GAO

B.E., Tianjin University, China, 2009

M.E., Tianjin University, China, 2012

A Dissertation Submitted to the Graduate Faculty of The University of Georgia in Partial Fulfillment of the Requirements for the Degree

DOCTOR OF PHILOSOPHY

ATHENS, GEORGIA

2016

FREQUENCY CONTROL, MODELING, ALIGNMENT ADAPTATION, AND SAFETY CONCERNS FOR THE WIRELESS CHARGING OF ELECTRIC VEHICLES

by

YABIAO GAO

Major Professor:	Zion Tsz Ho Tse
Committee:	Javad Mohammadpour
	Qun Zhao
	Antonio Ginart

Electronic Version Approved:

Suzanne Barbour
Dean of the Graduate School
The University of Georgia
May 2016

ACKNOWLEDGEMENTS

I would like to thank my major advisor Dr. Zion Tsz Ho Tse for his support and advisement. Without his effort, I could not have gone so far and finished the Ph.D. program. I would like to express my sincere gratitude and respect to my committee members: Dr. Antonio Ginart, Dr. Javad Mohammadpour, and Dr. Qun Zhao for their insights and suggestions to the dissertation. Moreover, I would like to express my gratefulness to my current and previous lab fellows including Alex Squires, Yue Chen, Dr. T. Stan Gregory, Kevin Wu, Huawei Yang, Adam Wineland, Austin Taylor, and Aleff Oliveira. Especially, I would like to offer my appreciation to Aleff for his help in my experiment. Meanwhile, I would like to give my special thanks to Mr. Chen Duan and Dr. Nan Liu for their kind support and insight to my research. I would also like to appreciate those who have assisted me in building experimental platform: Ms. Blair Farley, Mr. Chris Mershon, Mr. Matt Tiffany, and Mr. Terrance Walsh. Finally, I would like to offer my deepest gratitude to my parents for their unconditional love and care.

TABLE OF CONTENTS

LIST OF TABLES

LIST OF FIGURES

Page

CHAPTER 1

INTRODUCTION

Wireless communication has significantly changed human life in almost every aspect of society since Guglielmo Marconi, the 1909 Nobel laureate in recognition of his contribution to wireless telegraphy, invented the first radio telegraph system in 1895 [2]. Compared with wireless communication, wireless power transfer (WPT) via electromagnetic waves has had limited influence on the world although the concept of WPT was originally proposed by Nikola Tesla in the 1890s [3-5].

Unlike wireless power delivery, wireless signal transmission does not emphasize transfer efficiency because the signal content is preserved when modulated on an electromagnetic wave, and can be successfully demodulated by a radio receiver even though it is greatly attenuated over a long distance. In addition, wireless signals usually transmit on extremely high frequency carriers ranging from several GHz to hundreds of GHz. High carrier frequency means high antenna quality factor, which guarantees the signal strengths can remain within an acceptable range over a long distance. WPT, however, has limited transfer distance considering the efficiency and high attenuation and cannot operate on high frequencies for high volumes of power transmission due to the limitations of existing power transistor technology. Normally the frequency of WPT is limited to 300 kHz for high power applications including electric transportation [3, 6, 7]. The operating frequency in some studies is above 1 MHz but only in low power applications [8].

The following introduces currently available wireless power transfer techniques, the wireless charging of electric vehicles (EV), research motivation, and the scope of research of the dissertation.

1.1 WIRELESS POWER TECHNOLOGIES

Wireless power transfer technologies fall into two categories, one is radiative far-field including microwave coupling and laser beaming, and the other is non-radiative near-field including capacitive and inductive coupling [9-12]. Figure 1.1 demonstrates the structure of a typical WPT system that consists of an energy/wave transmitter, a power conversion module for driving the transmitter, an energy receiver, and a power conversion module which regulates the received power suitable for loads such as batteries [12].

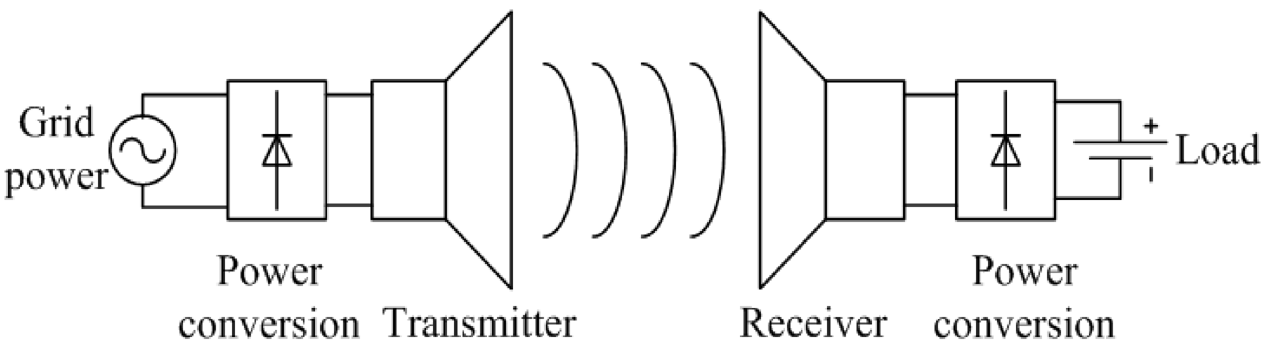

Figure 1.1. WPT system structure

WPT has a wide range of potential applications such as digital devices and electric vehicle charging, household appliances, medical implants, space solar power, etc., which has drawn great attention and attracted a large number of researchers in the past few years [13-18]. Dr. Ron Hui has focused on low power inductive coupling for more than one decade and his planar printed circuit board transformer is available on the market nowadays for wirelessly charging consumer electronics [19]. Dr. Paul Jaffe researched a space solar conversion and transmission module to transfer sunlight energy to the earth via microwaves, and demonstrated a 12%

combined conversion efficiency on a prototype in a space-like environment [13, 20]. Dr. Patrick Aiguo Hu et al. presented a wirelessly powered implantable device and its frequency control method for effective power delivery under variations in load, alignment, coupling, and other circuit parameters [17]. Dr. Joshua R. Smith's team demonstrated a WiFi router-powered system that transfers wireless power to sensors, smart devices, and cameras as long as these devices are equipped with 2.4GHz antennas for communication via WiFi, Bluetooth, or ZigBee, allowing for network and power transmission simultaneously. They have experimentally showcased battery-free temperature and camera sensors powered with Wi-Fi at ranges of 17 and 20 feet separately [18].

1.1.1 Radiative WPT

Radiative WPT is the transmission of energy over a distance which is much larger than the radio wavelength [12]. The transmitter emits electromagnetic (EM) waves and the receiver in somewhere else converts the radio waves to power its load. The radiation arriving at the receiving surface is a certain proportion of the radiation emitted from the source. The power density of the far-field operation declines by $1/r^2$, where r is the distance from the power source to receiver antenna, indicating that the efficiency becomes much lower as the distance r increases and making it suitable for low power level applications [12, 21]. To improve the efficiency of radiative power transfer, high frequency EM waves in the microwave range or even visible spectrum are employed to keep the energy beam narrow, which allows the energy transferred to focus on the receiver antenna.

The microwave power transmission era began in 1958 when the Raytheon Company studied a microwave-powered aircraft which could stay up in the air for communication or surveillance purposes [5]. Unfortunately, the microwave-powered platform looked promising but was not successfully developed [5]. Microwave power transmission is only suitable for low power level application such as powering a sensor remotely in conditions where a battery exchange or recharge is not convenient [12, 22]. This limited use takes human exposure to EM fields into account since a high power density of microwaves can cause health risks to human body.

Laser power beaming is a type of radiative WPT that uses laser light as a medium to transfer energy. The laser beam can maintain an intense energy concentration even at a long distance. The basic principle is that a laser light beam from a laser source arrives at receiving photovoltaic cells (PV) to produce electricity. Although laser power beaming seems a promising wireless power transfer solution, the efficiency of PV for light to electricity conversion is <50%, resulting in an even smaller overall efficiency considering the power losses in the stage of electricity-laser at the transmitter side [12]. The laser beam can be blocked by solid dielectrics and can damage eyes of humans and animals or even kill living objects. These negative effects strongly discourage the use of laser power beaming on a mass scale.

1.1.2 Capacitive WPT

Capacitive WPT was first proposed and demonstrated by Nikola Tesla in 1891 [4]. The basic principle is that alternating current (AC) can flow through a capacitor and achieve wireless power transmission when the capacitor is configured as two conductive plates facing each other at a certain distance. Figure 1.2 shows the typical capacitive WPT structure, which consists of an AC source, four conductive sheets, a rectifier and power conditioner, and loads [23]. The energy stored in the capacitor can be expressed by $E = 0.5CU^2$ where C is capacitance and U is voltage across the two plates. The maximum allowed electric field is restricted to 30kV/cm to prevent air ionization, indicating that the voltage across the two plates is limited to some value, which reduces the power-delivering capability of the capacitive WPT system [24]. Therefore, capacitive WPT should be more suitable for low power applications due to restriction of electric field strength.

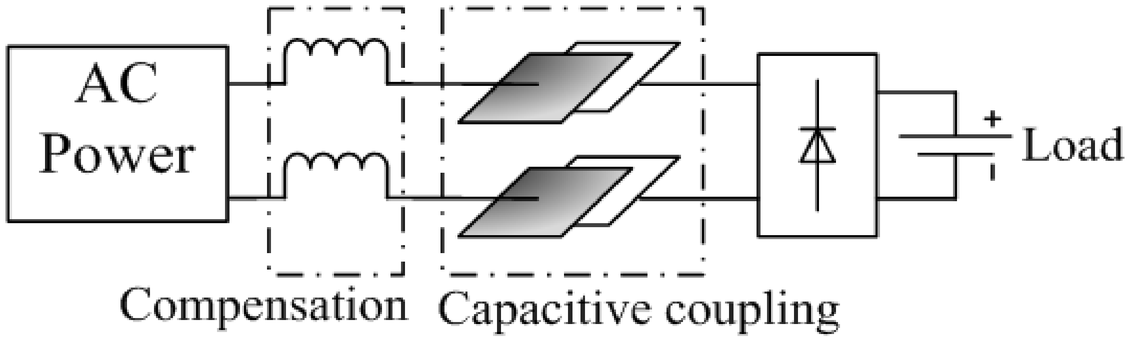

Figure 1.2. Capacitive WPT structure

In contrast to inductive WPT, capacitive WPT delivers power via electric field rather than magnetic field. Unlike inductive WPT, metal debris between two capacitive WPT pads will not influence the efficiency of power delivery since the metal sheet separates the capacitor into two capacitors in series with each other. This might be one of the best known benefits capacitive power transfer can bring over inductive [12, 25, 26]. Addtionally, capacitive coupling has greater misalignment tolerance than inductive, and the electric field is confined between the plates [26]. These advantages of capacitive systems are inspiring researchers to overcome the above design challenges and investigate high power applications with large distance between the transmitter and receiver.

1.1.3 Inductive WPT

The idea of inductive WPT can date back to the discovery of electromagnetic waves by German physicist Heinrich Hertz who created a spark gap transmitter and receiver and saw through a microscope a small spark which was energized by a spark from the transmitter [5, 27]. Inspired by Hertz’s work, Nicolas Tesla, who also proposed the capacitive wireless power transfer solution, demonstrated and patented inductive WPT in the 1890s [5, 28]. Figure 1.3 shows a picture taken in the 1890s of his experimental setup for powering a lamp wirelessly by using magnetic resonance [28]. Unfortunately, inductive WPT did not become a fast growing research topic or reality in industry until the beginning of 21st century, accompanying the availability of high-frequency switching transistors, popularity of mobile network and digital devices, and electric transportation [6, 16]. In many literatures, inductive WPT or inductive power transfer (IPT) is simplified as WPT due to the prevalence of inductive coupling in the wireless power field. Since power is delivered across an air gap in IPT, it is also called a loosely coupled IPT/WPT system which is compared with a transformer.

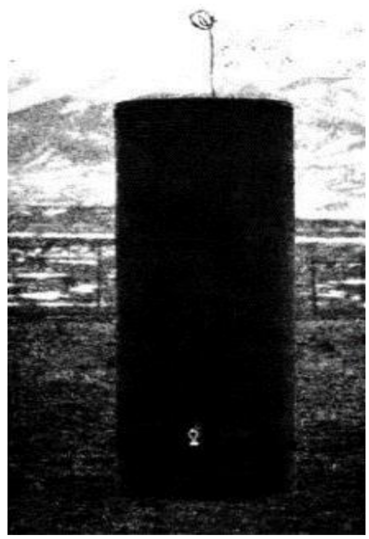

Figure 1.3. Tesla coils illuminating the phosphorescent lamp close to bottom of the picture by using magnetic resonance coupling

Today's inductive WPT systems use the basic system structure and principle Tesla created more than one century ago. The basic theory of IPT systems relies on Faraday's and Ampere's Laws. The primary coil is energized by AC to produce a magnetic field, which in turn induces a voltage/current in the secondary coil which is placed within proximity of the field. Since the transmitter and receiver coils are loosely coupled due to a much lower coupling factor than a traditional transformer, the air gap at which the power can be delivered is increased if both the coils are compensated by capacitors to form resonance at a certain frequency. This energy transferring process is also referred to as magnetic resonance coupling, or simply as magnetic/inductive coupling. In Figure 1.4, an inductive WPT system typically includes a transmitter coil (also called primary), an RF power supply for driving the primary, a receiver coil (also called secondary or pickup), compensation capacitors, and power regulation electronics for powering loads.

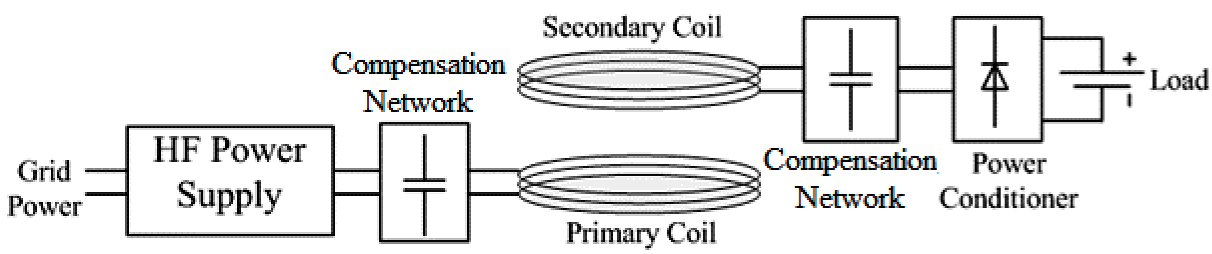

Figure 1.4. Block diagram of an inductive WPT system

Normally, the air gap of IPT systems is set at less than the radius of the primary or secondary coils to maintain a decent efficiency, so they are categorized as near-field WPT in comparison to far-field WPT such as laser or radiative coupling. The energy transferring distance of IPT can be extended by applying a higher quality factor, which means a higher operating frequency. However, a very high switching frequency (MHz level) could cause large power losses and challenge power regulation; a very high quality factor means the power transferred can significantly decrease even for a minor coil detuning, which is quite common in application. Therefore, an IPT system operating from 10kHz – 200kHz should be suitable for high power applications (kW level) including electric vehicle charging, and is a good compromise between power transfer capability and efficiency, and system robustness.

1.2 WIRELESS ELECTRIC VEHICLE CHARGING

Electric vehicles (EVs), usually refueled by plug-in chargers, are becoming increasingly popular due to concerns about greenhouse gas and air pollutant emissions, predicted fossil fuel crisis, and a desire to move towards renewable energy [3, 6, 7, 16, 29]. Although zero emission EVs are highly attractive, people are apprehensive of the shorter travelling range of a single charge and a much longer refueling time than that of engine vehicles. Besides, they require the user to change his or her behavior by remembering to plug in the EV, and their ground charging infrastructure is at risk of vandalism and electrocution and can be vulnerable to harsh weather such as heavy rain and snow.

Wireless charging (WC) using magnetic coupling is a promising way to address the above issues with EVs. EVs can be recharged whenever a public charging station is available. Because of its non-contact manner, WC improves upon EV convenience and charging safety; users simply park their EV over a charger. WC infrastructure can be buried underground, making it waterproof and safe from vandalism and electric shock.

1.2.1 A brief history

Although Nicolas Tesla proved the possibility of power delivery across an air gap through magnetic coupling in the 1890s, WPT research and application did not make significant progress until the early 1990s [3, 5, 16, 30, 31].

In 1994, researchers from UC Berkeley released a 60kW inductive charger powering a 35-passenger bus in both static and mobile modes [31, 32]. The speed was set at 18 and 24 km/hr respectively during the mobile testing. The efficiency for both operating modes was around 60% at output power of 60kW. The switching frequency was 400 Hz due to the limitation of high power transistors, which greatly limits the performance of the charger. This demonstration was supported by California Partners for Advanced Transit and Highways (PATH) and showcased great potential for wirelessly charging EVs [31, 32]. In the same year of 1994, an inductive power distribution was patented by Dr. John Boys from Auckland University [30]. The IPT prototype operated at 10kHz with output power level of 500W. From then on, researchers from Auckland University directed by Dr. John Boys and Dr. Grant Covic have been working on IPT systems for rail transportation, EVs, etc [33]. Based on Dr. Boys and Dr. Covic’s research on IPT, HaloIPT was created to provide EV wireless chargers and was acquired by Qualcomm in 2011.

In 2009, Korea Advanced Institute of Science and Technology (KAIST) launched an online electric vehicle (OLEV) that is fed with electricity by road embedded IPT tracks while the vehicle is on the move [34, 35]. KAIST announced that more than 180 patents have been filed on the OLEV and related technologies [36, 37]. A 60kW bus was tested by the road embedded track with an efficiency of 60% in the first demo. In 2013, two buses were delivered for a 24km inner city transit route of Gumi, South Korea, with 85% efficiency in transferring 100kW electricity at 20kHz via a 20cm air gap from track surface to bus chassis. Generally, 5-15% of the bus route needs to be rebuilt and equipped with segmented charging strips to allow the bus to receive enough energy to power the entire route. The OLEV was chosen as one of the 50 best inventions of the year 2010 the Time Magazine [37]. Researchers from KAIST claimed that the battery size can be reduced by 80% with in-motion charging, aiming to solve the low density, high weight, and long charging time of battery issues with current EVs [36]. OLEV Technology Inc. was established in Boston MA, 2011, to commercialize the road powered EV solution.

Research on IPT technologies for powering EVs has drawn increasing public attention in the last decade and a number of institutions from both academia and industry are involved in the effort to popularize electric transportation. There are research groups from Virginia Tech, Georgia Tech, U. of Michigan, New York U., Utah State U., etc. that are working on wireless EV charging [6, 38-41]. Researchers from Virginia Tech developed a 4 kW contactless EV charger and designed an asymmetrical coupler for maintaining the coupling under air gap and lateral distance variations [38, 42]. The research group led by Dr. Chris Mi from U. of Michigan developed a double-sided LCC network and a bipolar coupler for efficient EVWC [43, 44]. Researchers from Georgia Tech designed a universal inductive charger to be suitable for charging multiple EV models [39]. The team from New York U. studied a multi-level type multi-phase resonant converter for EVWC [45]. Utah State U. Power Electronics Lab (UPEL) are implementing an in-motion wireless charging project for EVs and evaluated its economic and environmental feasibility [46]. Oak Ridge National Laboratory (ORNL) developed and improved EVWC technology for both stationary and in-motion charging [47-49]. They evaluated and tested this technology in terms of power flow control, power converter design, EM exposure to human body, and standardization of EVWC [50-52]. Another interesting in-motion wireless charging concept, proposed by a research group led by Dr. Takashi Ohira at Toyohashi University of Technology in Japan, applies dielectric coupling to transfer power from the roadway to a steel belt installed inside vehicle tires [53]. They also demonstrated the wheel WPT concept via a 1/32 scale EV model [53]. The power transmission efficiency was reported up to 76% at an operating frequency of 52MHz [54]. Since the vehicle tire and roadway surface are in close contact with each other, a human or pet would have limited access to the electric field between the WPT electrodes. Some start-ups that are providing EVWC solutions include Momentum Dynamics (Figure 1.5a), WiTricity (Figure 1.5b), EVATRAN Plugless (Figure 1.5c), and HEVO Power (Figure 1.5d) [16].

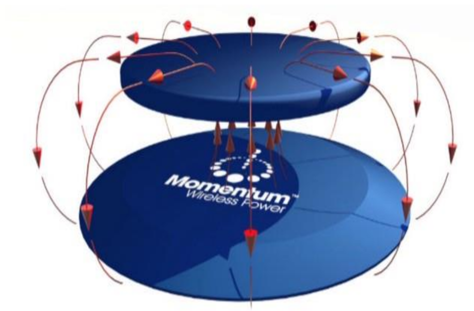

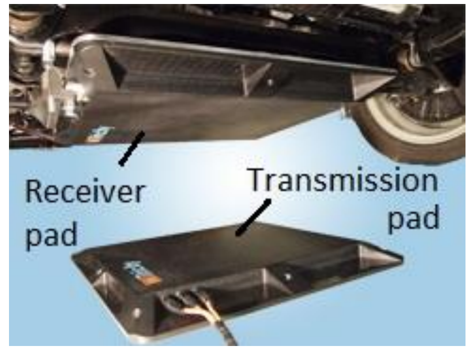

(a) (b)

(c) (d)

Figure 1.5. (a) Momentum Dynamics WC setups; (b) WiTricity EVWC system; (c) Plugless EVWC charging demo; (d) HEVO's EVWC manhole.

Nowadays, EVWC has arrived at the stage of standardization; various groups have set general requirements and specifications for IPT systems that suppliers need to follow into production. The SAE (Society of Automotive Engineers) released SAE-J2954 in 2013 to standardize IPT technology for charging EVs, including communication, alignment and foreign object detection, power electronics topologies, testing procedures, and interoperability [55]. UL2750 is a EVWC safety standard outlined by Underwriters Laboratories (UL) [56]. A collaborating group from International organization for Standardization (ISO) and International Electrotechnical Commission (IEC) works on a technical specification document, PT61980, to define requirements of EM field, safety, and communication associated with EVWC [49, 57].

1.2.2 IPT systems for EV charging

Figure 1.6 illustrates the components of a typical wireless charging system used for EVs. The grid power is first rectified to DC, then a resonant inverter converts the DC power to high frequency AC to drive the primary coil and produce a magnetic field. According to Faraday's law of electromagnetic induction, another AC with the same frequency as the magnetic field is induced in the secondary coil. Additional power conversion is required to convert the high frequency circulating current into DC to charge a battery pack. The on-board electronics consist of a rectifier, a DC-DC converter, a battery management system (BMS), as well as sensing modules. As the AC load is not purely resistive, a phase shift between the grid voltage and current will occur, which will lower the power delivery. Thus, a power factor correction (PFC) at the grid power input is used to decrease the apparent power and total current drawn from the grid. The driver interface displays all of the system’s electrical and mechanical parameters such as charging monitor, alignment information, and existence of metal and living things. These monitoring data can be transmitted to the primary controller via radios to enable, disable, and control the power delivery.

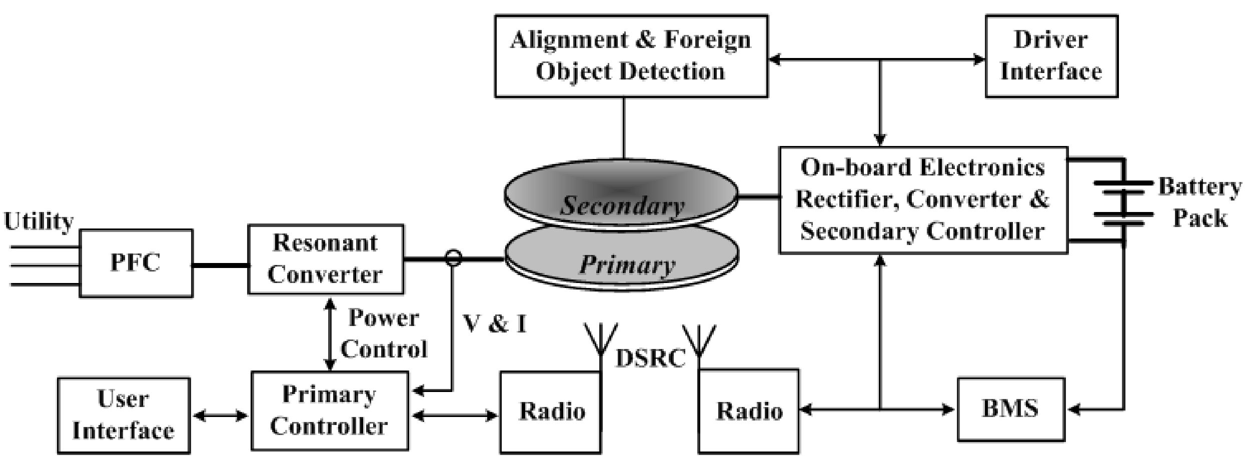

Figure 1.6. Functional diagram of an IPT charger for EVs

In a commercial wireless EV charger, Dedicated Short Range Communications (DSRC) are recommended to be used as the wireless communication mechanism between the ground stations and the vehicle side due to its fast response, and will be applied widely in cars as required by the U.S. department of transportation and the SAE communications committee [49, 58, 59]. The EV can communicate with a wireless charging station as long as it enters the zone where the DSRC signal is available.

Figure 1.7 shows four topologies which are commonly used in IPT systems, including Series-Series compensated (SS), Series-Parallel compensated (SP), Parallel-Parallel compensated (PP) and Parallel-Series compensated (PS) setups [39, 60-62]. The series-compensated secondary is equivalent to a voltage source, while the parallel-compensated secondary acts as a current source suitable for battery charging. For the primary side, a series-compensated primary has several benefits over parallel. First, the primary tuning capacitor is more robust over the range of magnetic coupling coefficients or quality factors. On the other hand, the tuning capacitor in a parallel-compensated primary setup should be adjusted if there is a magnetic coupling or quality factor change caused by horizontal misalignment, vertical gap, parameter drifts of electronic components, etc., which are quite common in real circumstances. Hence, the series-compensated primary topology contributes to an easier way to achieve the resonance of the WC system. Second, unwanted harmonics could occur due to parasitic components caused by loose magnetic coupling. A series-compensated primary setup can reduce harmonic effects and keep the system stable.

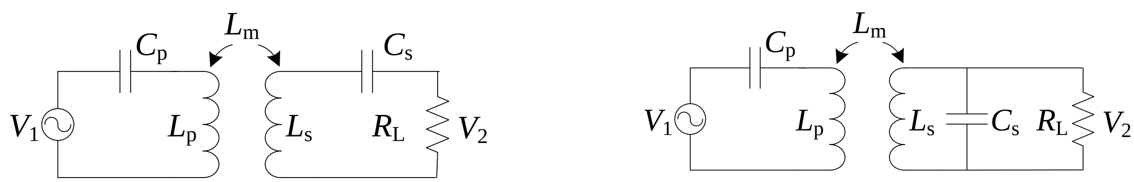

(a) (b)

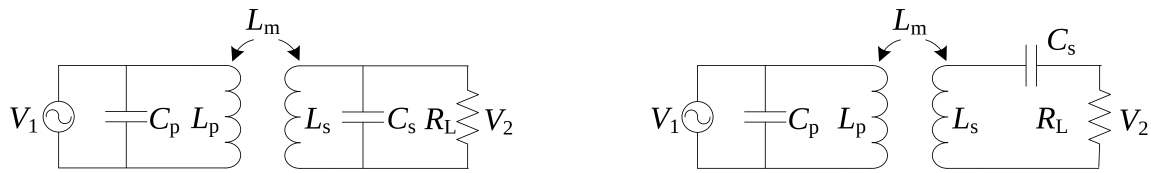

(c) (d)

Figure 1.7. Topologies for IPT. (a) SS; (b) SP; (c) PP; (d) PS.

In addition to the four basic IPT compensation topologies, advanced compensation topologies such as LCC and LCL are proposed to lower the circulating current of coils and increase the rail voltage of the primary inverter, which can further decrease the conduction loss by power transistors and capacitor voltage stress. Detailed assessment of LCC is covered in depth by Li et al. in [43], while Wu in [63], Huang in [64], and Hao in [65] discuss the LCL compensation network.

Three types of coil structures and shapes are presented in the literature, including circular, flux-pipe, and bipolar topologies [7, 56, 66, 67]. The circular coil structure is commonly used with an efficiency as high as 90% [63]. Although the circular topology needs a bigger coil diameter than the other two methods to achieve the same power transfer capabilities, its simplicity and low cost make it a preferred option for our experimental setup. For the flux-pipe topology, the coil is wound along an H-shaped ferrite bar [68, 69]. This coil structure has a double-sided magnetic flux path, so it is also called a double-sided winding transformer. The flux on the pad's back is the same as the front side, meaning that the magnetic loss in the shielding plate is significant. The bipolar topology employs D or Q coils to couple the power; a detailed description is given in [66, 67]. The bipolar pad has less flux going through the pad's back and a higher efficiency than a circular pad.

The control of IPT systems mainly involves pulse-width modulation (PWM) of the resonant converter at the primary side. The frequency value and duty cycle are used to modulate the converter for determining power efficiency and density [51, 70-72]. Fixed and variable frequency controllers are generally used in EVWC [56]. The fixed frequency operation is simple in both software programming and hardware realization. However, a fixed frequency requires more severe operating conditions such as limited tolerance for the positioning of the coupled coils and the size of the air gap between the pads, since the power delivery and efficiency can be greatly reduced by misalignments [71, 73]. A variable frequency controller is proposed to make the IPT more adaptive and robust in response to the external variances that could lower IPT performance, although the system becomes complex and high-cost in both software and hardware with control algorithms, additional circuits, and communication modules [51].

EVWC can be categorized into stationary (garage or park-to-charge) and dynamic (in-motion or road-powered) charging [7, 16]. With stationary WC, an EV driver simply parks the vehicle over a ground primary charging station, and a corresponding charging pad attached on the vehicle underbody picks up the power and recharges the EV. WC technology has already been proposed to be utilized in public transit systems at bus stops in what is known as “opportunity charging” [16]. When the electric bus idles or waits for passengers at a stop, the bus can be refueled for as long as it remains at the station. The concept of opportunity charging can potentially reduce the battery pack size equipped on electric transit systems, leading to more sustainable public transit due to lower battery cost and lighter vehicles. In addition, opportunity charging could reduce the cost and volume of the heavy batteries carried by electric cars and trucks.

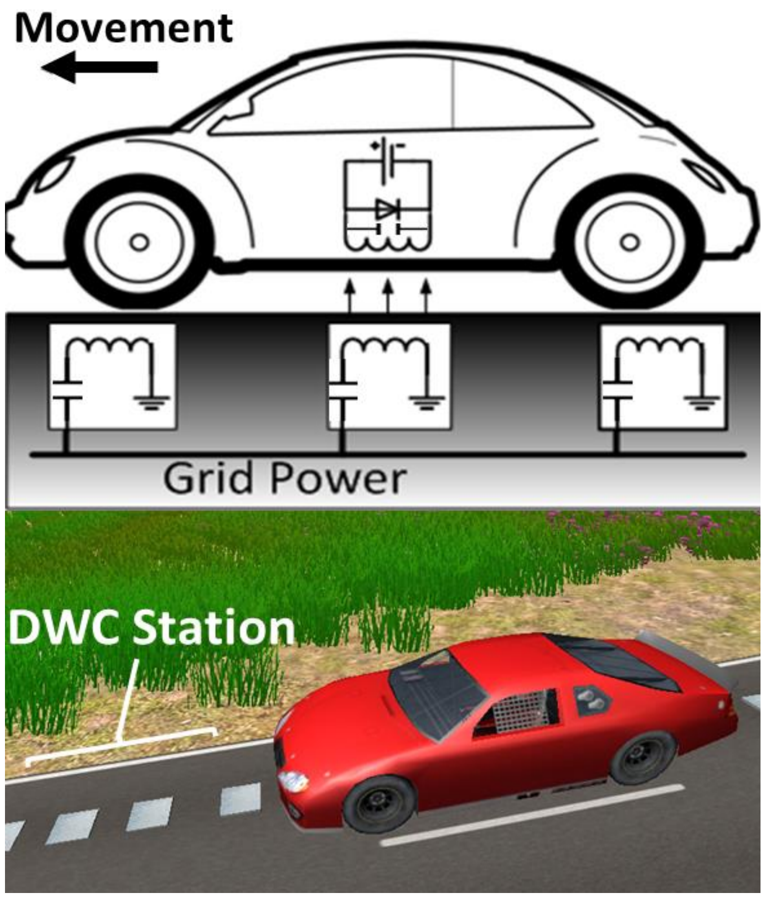

Figure 1.8. Conceptual diagram of dynamic wireless charging (DWC) of EVs

Dynamic WC involves a string of charging pads or segmented charging strips that are built underneath a length of the road or highway to charge EVs as the vehicles pass over them [7]. This concept would significantly decrease the need for energy storage devices on EVs and fundamentally solve vehicle range anxiety. Figure 1.8 illustrates a conceptual diagram for future transportation where the electric car is roadway powered while it is moving.

1.2.3 EV charging technologies

EV charging technologies can be classified as plug-in charging and wireless charging. Charging a battery conductively by directly connecting the load with grid power is the traditional plug-in charging method developed for EV usage. Considering about 80% of drivers in the U.S. drive 40 miles or less per day, there are three kinds of plug-in charging solutions available on the market:

level 1, level 2, and DC fast charging [74-76]. Table 1.1 offers a comparison among the three different charging solutions in terms of power, duration of charging event, range per hour of charging, cost, typical uses, etc. Level 1 charging requires plugging the EV into an ordinary household outlet, meaning that this charging method is low-cost and does not require any professional installations as long as the user has access to a standard 110V outlet. However, the maximum power of Level 1 is limited to 1.6kW. For a Nissan Leaf, Level 1 charging allows it to be recharged at a rate of about 4.5 miles of range per hour, or about 22 hours for a full charge [77]. DC fast charging, the fastest type of charging currently available, provides up to 40 miles of range for 10 minutes of charging or 80% of full charge in 30 minutes [76, 78]. However, it is almost impossible to install such a high power rating (50-60kW) and expensive charging equipment (up to $160,000) [78]. Level 2 is a compromise between Level 1 and DC fast charging; it requires 240V outlets and charges an EV at 6.6 kW or around 26 miles of range per hour of charging [42, 76]. Some high-power household appliances also employ the 240V grid input. All the electric cars are made to be compatible with both Level 1 and 2 charging, while DC fast charging requires special equipment on the cars.

Table 1.1. Specifications and comparison of Level 1, 2, and DC fast charging for EVs [78, 79]

	Level 1	Level 2	DC fast charging
Typical duration of charging event (hours)	6 - 10	1 - 3	<0.5
Range each hour of charging (miles)	2 - 5	10 - 20	>75
Types of utility	120V AC	208/240V AC	208/480V AC three-phase input

Power ratings (kW)	1.6	Typically 6.6 (can be up to 19.2)	50 - 60
Cost ($USD)	600 - 1,000	About 2,000	10,000 - 160,000
Typical applications	Home use; Workplace parking lot; Long term parking (8+ hours).	Home use for a faster charge; Charging in a commercial area while shopping or on business.	Long trip use; Extension of trip.
Location/installation preferences	Home garage; Long-term; parking/visitor parking; Workplace parking area.	Municipal or private parking decks in downtowns, shopping centers, or home garage.	Close to highway entrances and exits; Roadway points with high volume of transportation load.

Although EV makers have not offered wireless chargers as an option on their EVs up to now, WC technology could become a competitive alternative over plug-in because of its cordless manner, along with unique benefits such as hands-free, automatic charging, weather-proofing, and avoidance of electric shock [3, 6, 80]. WC can be configured for multiple power levels since both WC and plug-in charging can maintain an efficiency of >90% from grid to battery [3, 63]. Although plug-in charging can have a slightly higher efficiency than WC, the advantages of WC over plug-in largely outweigh this small disadvantage.

1.3 MOTIVATION AND SCOPE OF THE PROPOSED RESEARCH

As stated above, EVWC systems research involves circuit topologies, power flow control, magnetic coupler design, safety, and vehicle alignment. Although there are a number of publications and some preliminary commercialized products are available on the market, research towards more adaptive, robust, efficient and safe WC is still of great value for widespread adoption of EVs.

1.3.1 Positioning and adaptability to misalignment

One significant characteristic of WPT systems is the relative position between the primary and secondary is variable. It is unrealistic to expect EV drivers to park their vehicle over a ground station so that the two coils are precisely aligned. The inevitable misalignment of the two coupled coils can cause a mutual inductance variation, which might lower the WPT efficiency or even burn the power electronics in a severe condition. To address the misalignment issues in EVWC, two approaches are researched in this dissertation:

First, a uniform voltage gain control is proposed to maintain a stable voltage output when the coupled coils are not well aligned. The switching frequency of the IPT system is tuned in each charge based on the alignment conditions between the two coils to compensate for the negative effects of a misalignment. This frequency control method improves the maximum allowed misalignment for EVWC but cannot solve the issue fundamentally. It cannot work if the mutual inductance is too weak.

Second, a vehicle alignment detection system is proposed to assist the EV driver while parking to ensure the two coils are well aligned before recharging the vehicle. However, additional equipment for this purpose is bulky and can increase the system complexity and cost as well.

This dissertation investigates two practical alignment methods that utilize the existing IPT platform to detect coil positioning and guide parking. The first method is based on the fact that the resonant frequency of IPT changes along with different alignment conditions, so the position can be determined by measuring the resonant frequency and the phase angle between voltage and current of the primary power inverter. The second method is to use four auxiliary minor coils as sensors to measure a magnetic field that is produced by the ground station. The relation between the four outputs and coil position is derived to determine the secondary coordinate in three dimensions. Besides the horizontal alignment information, this method can also be used to figure out the air gap considering different car models and weights. This data can be used to improve the interoperability and universality of wireless EV chargers.

1.3.2 Frequency-spacing modeling

The leakage inductance is compensated by tuning capacitors for resonance to deliver huge amount of power through an air gap in a loosely coupled system, meaning that IPT systems can only deliver power at certain frequencies. Traditionally, the operating frequency is determined by two steps: the first is to determine the coupler mutual inductance by finite element analysis (FEA) or experimental measurement; the second is to calculate the optimal frequency for WPT. This dissertation simplifies this process by modeling the relation of frequency and coil position in IPT systems, which bypasses the intermediate mutual inductance process. The derived formula takes three-dimensional coil position into account while assuming the two coils are in parallel with each other. This model allows the frequency to be fixed in about 10ms, which shows higher computational efficiency in contrast to FEA simulation. A fast approach to determining the operating frequency of IPT is highly desirable in such a dynamic environment where the relative position of coils can be variable in both lateral and vertical directions.

1.3.3 Safety and health concerns

Although the wireless charging of EVs can be seen as non-radiative due to its relative low EM frequency, possible health effects on the human body and safety concerns from the high volume of power delivered between the two charging pads are investigated in this dissertation. The safe operation of a WC system is evaluated in terms of possible health effects from human exposure to EM field, thermal effect on metal, and EMI (electromagnetic interference) to other electronic devices. International guidelines regarding EM health are reviewed to evaluate our testing results and contribute to a deep understanding of safety concerns of EVWC.

1.4 BRIEF OVERVIEW OF THE DISSERTATION ORGANIZATION

Chapter 1 reviews the wireless power technologies and states the research background and objectives of the dissertation. Chapter 2 investigates a uniform voltage gain control to tune the switching frequency to allow the IPT system to have a larger misalignment tolerance. The uniform voltage gain is achieved by analyzing a circuit model in multiple misalignment/mutual inductance cases. An experimental platform is created and a tuning program is implemented on a DSP controller to demonstrate the frequency control approach. Chapter 3 derives a mathematical model to calculate the mutual inductance and resonant frequency of an IPT system. Experimental results are conducted to validate the mathematical approach.

Chapter 4 describes a vehicle alignment technology that uses the mutual inductance to identify the relative position between the primary and secondary coils while a three-dimensional coil positioning approach is researched in Chapter 5 by using four auxiliary minor coils to sense the EM field and align the two coils. The mathematical derivations between the voltage of auxiliary and secondary coordinates are included in the chapter. The experimental results show the high value of this approach to assisting EV drivers with parking their car over a ground charging station.

Chapter 6 introduces safety guidelines related to EVWC and shows a group of testing results including thermal effect, human exposure to EM field, and potential damage to electronics associated with EVWC. Design considerations and safety recommendations are presented for EVWC in this chapter.

Chapter 7 summarizes contributions of the dissertation, limitations of the work, and proposes future research topics in wireless EV charging.

CHAPTER 2

UNIFORM VOLTAGE GAIN CONTROL [1]

[1] Gao, Yabiao, Kathleen Blair Farley, and Zion Tsz Ho Tse. "A uniform voltage gain control for alignment robustness in wireless EV charging." Energies 8.8 (2015): 8355-8370.

Reprinted here with permission of the publisher.

2.1 ABSTRACT

The efficiency of wireless power transfer is sensitive to the horizontal and vertical distances between the transmitter and receiver coils due to the magnetic coupling change. To address the output voltage variation and efficiency drop caused by misalignment, a uniform voltage gain frequency control is implemented to improve the power delivery and efficiency of wireless power transfer under misalignment. The frequency is tuned according to the amplitude and phase-frequency characteristics of coupling variations in order to maintain a uniform output voltage in the receiver coil. Experimental comparison of three control methods, including fixed frequency control, resonant frequency control, and the proposed uniform gain control was conducted and demonstrated that the uniform voltage gain control is the most robust method for managing misalignment in wireless charging applications.

2.2 INTRODUCTION

The world has witnessed a rapid growth of plug-in hybrid electric vehicles (PHEVs) and pure electric vehicles (EVs) over the past decade due to the increase in greenhouse gas emissions, environmental pollutants, and fossil-fuel price fluctuations. However, PHEVs and EVs still need to address range anxiety, high battery cost, and the inconvenience of charging before their widespread acceptance [7, 44]. Wireless power transfer (WPT) has been an emerging research area for several years and could overcome the inconvenience of EV charging [44]. WPT allows power to transfer from a transmitter coil to a receiver coil over an air gap. Applications for WPT include mobile devices, household facilities, medical implants, and electric vehicles [7, 16, 44, 60, 81-85]. WPT is based on the principle of magnetic resonance couplings. The WPT system is mainly composed of a high-frequency power inverter, transmitter coil (also called “primary side”), receiver coil (also called “secondary side”), compensation capacitors, and rectification electronics. The alternating magnetic field generated by the primary side induces an alternating current in the secondary side. The rectifier converts the alternating current into direct current (DC), and then a DC-DC converter can be used to drive the desired load—for example, a battery. The compensation capacitors make up for the large inductance leakage and allow for a loose coupling, so power can transfer wirelessly across a large air gap.

WPT systems are frequency-sensitive due to their use of magnetic resonance. Any change in the resonant components, such as inductance, capacitance or load, can influence the operating frequency of the system. Since WPT systems operate in a non-contact manner, the physical spacing between the two coils can vary, resulting in a change in magnetic coupling and eventually shifting the best switching frequency for WPT [86, 87]. Often, EVs used in everyday life are not parked in the ideal position over the transmitter each time. The misalignment between the two coils influences the output voltage at the secondary side and hence changes the power delivery. Additionally, the chassis height might be different for different EVs, which can also influence the optimal switching frequency.

The body of this study focuses on a uniform voltage gain control method to address the frequency shift caused by misalignment and different air gaps while keeping the output voltage stable. A WPT system was developed to experimentally demonstrate the proposed frequency control under different coil alignments. There are four common resonant tank topologies for WPT based on different capacitor arrangements, including series-series (SS), series-parallel (SP), parallel-series (PS), and parallel-parallel (PP). A popular SP resonant tank is used as an example to demonstrate the frequency control in the experiment.

The WPT frequency controls fall into two categories: fixed frequency control and variable frequency control (also called "adaptive frequency control"). A fixed frequency control is normally operated under limited magnetic coupling variances, and a typical input voltage control is used to keep the charging voltage constant [88]. Resonant frequency control, which is a kind of variable frequency control, is designed to improve the WPT's adaptability for coupling change. Resonant frequency control allows WPT to always operate at a zero phase angle between the output voltage and current in the primary inverters. However, this causes the circulating current for resonant control to be quite high. In some studies, soft switching techniques are used to minimize the power losses of switching devices where the phase angle is forced to shift to a small value, making the WPT under-coupled [3, 39, 44, 61, 86]. There are several different ways to provide resonant frequency control, such as adding auxiliary components to adapt to the variance of magnetic couplings and directly switching the frequency of gate signals. For example, Aldhaher et al. adjusted the operating frequency by using saturable reactors [89], and the WPT system developed by Han et al. can adjust a different resonant capacitor and then change the operating frequency [90]. Although these auxiliary resonant components help to switch the frequency indirectly, they increase the cost of wireless chargers, especially in high power applications, and the additional electronic elements make the WPT system bulky. An automatic frequency tuning system is proposed by Sample et al. and Kar et al., where the WPT is tuned and operated at its resonant frequency, resulting in a zero load phase angle [86, 91]. Although the system is physically resonant, the output voltage at the secondary side is varied under different coil spacing, making it difficult to regulate power delivery to the battery. To address the influence of load variances on output voltage, a universal WPT was designed to charge different batteries [39, 92]. However, the universal system did not compensate for misalignment issues. Moreover, a different hardware configuration was used to achieve variable frequency control for WPT. Most of the proposed variable frequency controllers calculate the voltage and current of the secondary side via wireless communications, which can increase the cost and overall system complexity.

Wireless charging systems could operate at an adaptive switching frequency with uniform voltage gain in order to compensate for misalignment. The frequency control proposed in this paper is based on voltage gain and impedance analysis across the frequency domain, and the uniform voltage gain control is achieved through phase angle feedback at the primary side.

2.3 OVERVIEW OF THE WPT SYSTEM

The schematic diagram in Figure 2.1a illustrates the components of the WPT system with frequency control. The phase angle between output voltage and current of the inverter is measured before charging, and the digital signal processor (DSP) controller switches the frequency of pulse width modulation (PWM) signals to adjust the impedance of the system, thereby providing efficient wireless power transfer. The H-bridge inverter drives the transmitter coil to generate high-frequency electromagnetic fields. The voltage/current induced in the receiver is rectified to DC to power the load or charge a battery. Table 2.1 shows the parameters of the coils in the WPT system.

Figure 2.1b shows the power inverter packaged with liquid cooling. Two half-bridge, insulated gate bipolar transistor (IGBT) modules (FF100R12K4, Infineon) are employed to form the H-bridge controlled by a four-channel gate drive board. Since the IGBT can support a higher power rating with liquid cooling, the power inverter can be upgraded to a higher power level with minor changes. A resistor-capacitor-diode (RCD) snubber circuit is paralleled with each half-bridge switch to mitigate the undesirable spikes which can cause component failures and electromagnetic interference (EMI) issues. Moreover, these spikes can result in poor phase angle measurement, or even destroy the phase angle measurement circuit.

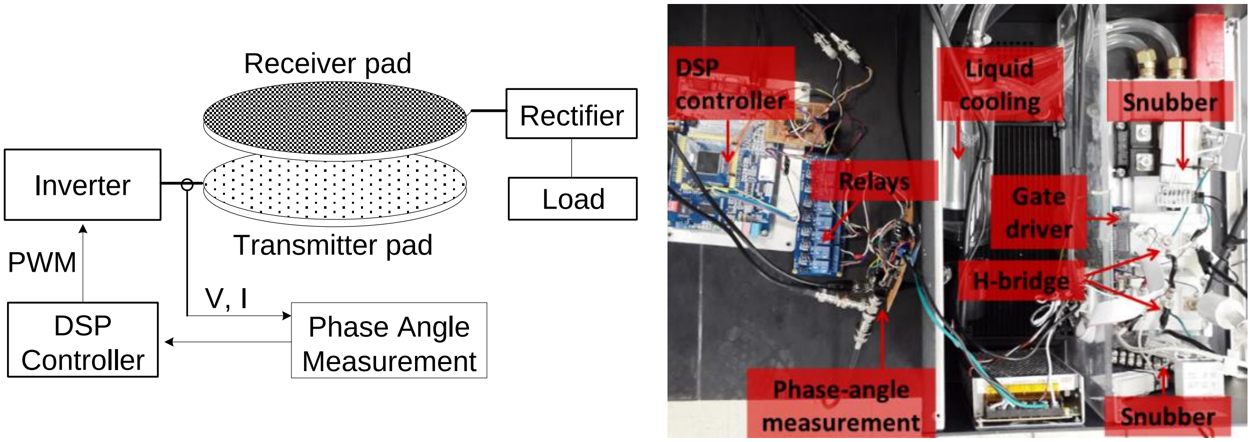

(a) (b)

Figure 2.1. (a) Overview of the WPT system; (b) Inverter and control electronics.

Table 2.1. Parameters of transmitter and receiver coils.

Specification	Primary	Secondary
Inductance (μH)	65.3	65.1
Tuning capacitor (μF)	1.0	1.0
Turns	12	12
Coil inside diameter (cm)	11	11
Coil outside diameter (cm)	56	56
Copper tube outside diameter (inch)	3/8	3/8
Copper tube inside diameter (inch)	1/4	1/4

2.4 PHASE ANGLE MEASUREMENT

The phase angle between the primary inverter's output current and voltage can be used to calculate the WPT's frequency. The operating frequency influences both the voltage gain and the phase angle. Thus, the phase angle must be measured in order to find and adjust the operating frequency to control the WPT system's power delivery.

Figure 2.2 shows the schematic design of the phase angle measurement circuit. The output voltage (V_{sense}) and current (I_{sense}) signals from the power inverter (modeled as an AC source in Figure 2.2) are transformed into two square waveforms by comparators. An exclusive-OR gate (XOR) combines the two square waveforms to one pulse waveform whose width is equal to the phase delay between V_{sense} and I_{sense}. A low-pass filter converts the pulse into a DC signal V_{phs}, which can be acquired by the analog-to-digital converter (ADC) in the DSP controller. The DC output of the filter is proportional to the phase angle between V_{sense} and I_{sense}. Since the high power in the WPT system can destroy the comparators and control circuit, four relays were used to isolate the power and control sides, as shown in Figure 2.2.

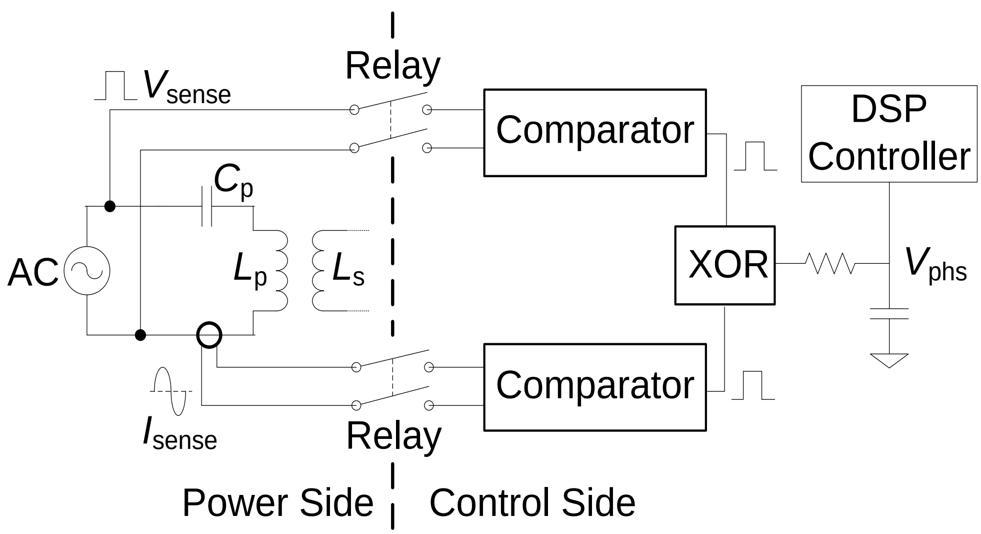

Figure 2.2. Schematic of phase angle measurement

Because the switching frequency is greater than 10 kHz, and at times even 100 kHz, it is quite difficult for a commercialized hall-effect voltage sensor to pick up the high speed. The voltage probe is directly connected to the output of the power inverter and then to the comparator. A current transformer is used to measure the circulating current in the coil. Although discrete Fourier transform (DFT) can be programmed in the DSP for phase angle measurements, using an

XOR and an RC filter greatly simplifies the embedded software development process and reduces the computational load of the DSP.

Once the phase angle has been measured, the switching frequency must be adjusted until uniform voltage gain is achieved. The DC input voltage is limited to 12 V during the frequency tuning process because lower voltage levels are much safer for the control circuit, and frequency tuning at high power levels would prolong the tuning time. Additionally, unreasonably fast variance of the frequency generates instability of output voltage and power emissions in high-power applications, which could damage the battery. Hence, frequency tuning is designed to occur at low power levels for both tuning speed and the safety of the circuit. After the switching frequency is well tuned, the WPT system operates at high power and starts charging.

2.5 ANALYSIS AND SIMULATION OF WPT

A full-bridge series-parallel WPT schematic is shown in Figure 2.3a. The four semi-conductors were driven by square waveform signals with a duty cycle close to but less than 50% to avoid make-before-break situations (momentary short circuit) in the inverter. Although the energy consumption of the rectifier can lower the system efficiency due to the inherent voltage drop, its simplicity makes it an ideal choice for industrial use where reliability and low cost are highly valued.

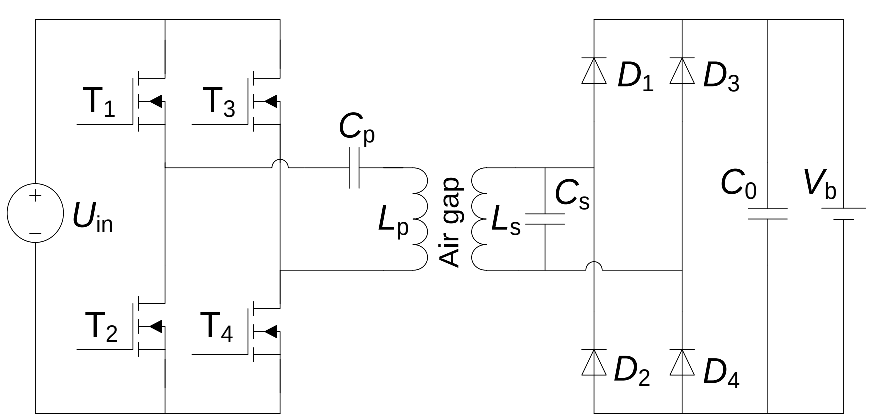

(a)

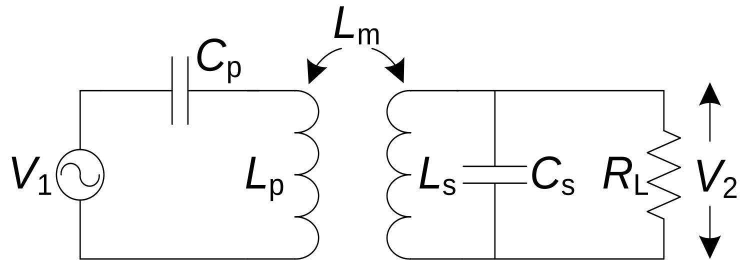

(b)

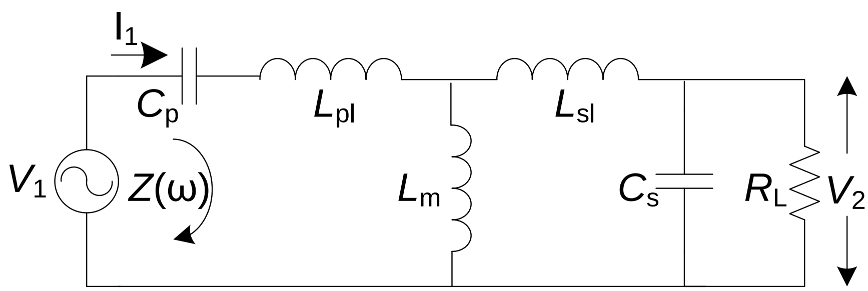

(c)

Figure 2.3. Circuit diagram of proposed WPT system: (a) SP topology for WPT; (b) Simplified SP topology; (c) Equivalent circuit of SP topology.

Figure 2.3b is a simplified series-parallel circuit diagram, and Figure 2.3c is the corresponding equivalent circuit. Equation (2.1) describes the circuit impedance (Z) in terms of the switching frequency (ω).

$$Z(\omega) = \frac{1}{j\omega C_p} + j\omega L_{pl} + j\omega L_m // \left(j\omega L_{sl} + \frac{1}{j\omega C_s} // R_L \right) \qquad (2.1)$$

where C_p is the series tuning capacitance of the primary side and C_s is the tuning capacitance of the secondary side. C_p must equal C_s to achieve resonance. L_{pl} and L_{sl} are the leakage inductances of each coil. Since both coils are the same, L_{pl} equals L_{sl}. L_m is the mutual inductance. The leakage and mutual inductance can be experimentally measured. The battery is equivalent to a resistive load, R_L, which can be calculated using the delivered power and voltage across the battery. For a desired 1.4 kW/120 V battery charging condition, R_L is 20 Ω. *j* is the imaginary unit.

The coupling coefficient k is defined as

$$k = \frac{L_m}{\sqrt{L_p L_s}} \tag{2.2}$$

$$L_p = L_{pl} + L_m \tag{2.3}$$

$$L_s = L_{sl} + L_m \tag{2.4}$$

The voltage gain G is the ratio of output voltage V_2 over input voltage V_1 as shown in Figure 1.3c and is determined by

$$G = \left| \frac{\omega^2 L_m C_p R_L}{\omega^4 L_p L_s C_p C_s R_L (1-k^2) - \omega^2 R_L (L_p C_p + L_s C_s) + R_L - j(\omega^3 L_p L_s C_p (1-k^2) - \omega L_s)} \right| \tag{2.5}$$

The mutual inductance changes with different coil alignments, which can cause a shift in the best switching frequency for WPT. Figure 2.4 is a simulation result of impedance and voltage gain against frequency performed in Simulink (MathWorks, MA, Natrick). Figure 2.4a, b show that the resonant frequency of WPT varies due to different magnetic couplings. Figure 2.4c is the voltage gain curve in the frequency domain. Although the WPT system has purely resistive impedance if operating at the resonant frequency, the voltage gain can change dramatically with different couplings, meaning that misalignment can cause the voltage output and power delivery to be unstable. The output voltage at resonance can be extremely high even under a weak coupling.

Although voltage gain varies at a specific frequency according to different magnetic couplings, uniform voltage gain can be achieved for a given coupling by changing the switching frequency. In Figure 2.4b, each curve goes through one fixed phase angle value at frequency f_0. The phase angle is fixed at f_0 no matter how the coupling varies, but the voltage gain G and impedance magnitude are the most unstable at f_0, so the WPT system cannot operate at f_0. On the left side of f_0, uniform gain theoretically exists, but the corresponding phase angle is much lower than on the right side of f_0, showing that the overall efficiency will be low if the WPT system operates on the left side of f_0. Therefore, the frequency range marked in Figure 2.4c, on the right side of f_0, is seen as the uniform gain control area. In Figure 2.4c, the frequency range for uniform gain control decreases from 24.4 kHz to 20.2 kHz when the coupling becomes weaker, and the corresponding phase angle is 18° at 24.4 kHz and 90° at 20.2 kHz. The total impedance is inductive in this frequency domain where the input voltage leads the input current, which realizes zero-voltage switching (ZVS) operation of the inverter.

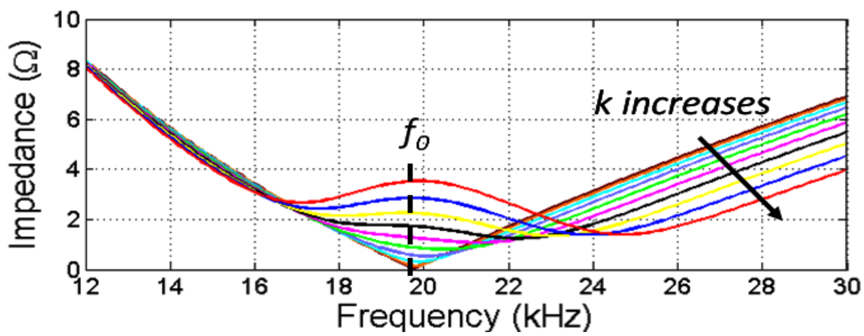

(a)

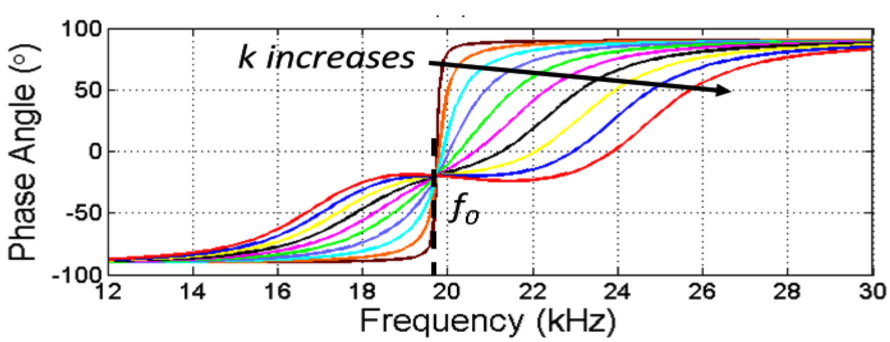

(b)

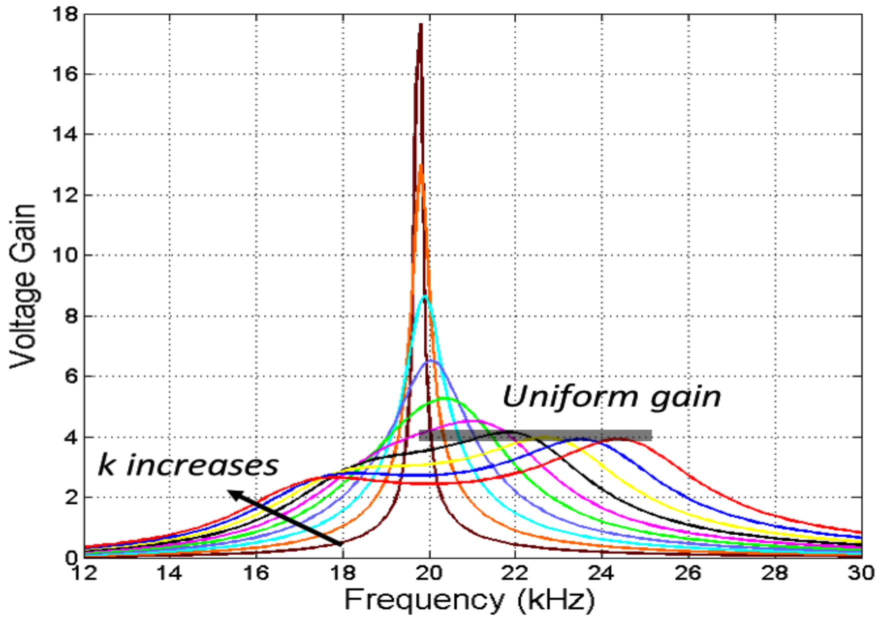

(c)

Figure 2.4. Impedance and voltage gain *G* in frequency domain. (a) Impedance magnitude; (b) Impedance phase characteristics; (c) Voltage gain in frequency domain. The simulation conditions were L_p = 65 μH, L_s = 65 μH, C_p = 1 μF, C_s = 1 μF, R = 20 Ω, and L_m = 2.5, 5, 7.5, 10, 12.5, 15, 17.5, 20, 22.5, and 25 μH.

For each curve of the phase angle in Figure 2.4b, one zero-crossing point exists, which indicates the resonant frequency point. Therefore, the switching frequency can be shifted to some value higher than the resonant frequency in order to achieve uniform voltage gain by first detecting the phase angle. Since the phase angle measurement cannot detect polarity of angles, the first step is to find the resonant frequency, and then increase the frequency until the predetermined uniform gain is obtained. From Figure 2.4 b,c the phase angle for a uniform voltage gain is around 18 – 22 as long as the magnetic coupling (*k*) is relatively strong. The phase angle corresponding to the uniform voltage gain increases when the magnetic coupling becomes worse.

2.6 CONTROL LOOP DESIGN

The main objective of this section is to explore the use of the proposed uniform gain control to generate a fixed output voltage regardless of any coil misalignment. The WPT is designed to automatically choose the optimal frequency after the EV is parked but before charging begins. A dummy resistor is required to simulate the battery status, as its equivalent resistive load can vary at different levels of charge.

The resonant frequency is the frequency that makes the load phase angle between the primary inverter's input voltage and current zero. While the resonant frequency allows the system to transfer maximum power, the output voltage at the secondary side varies significantly, thus increasing the difficulty in designing a DC-DC converter that can ensure the charger voltage is stable. The non-zero phase angle between the primary inverter's output voltage and current allows for the use of soft switches, decreasing the power losses caused by switching devices. The tuning process is as follows:

Firstly, the WPT system searches for the resonant frequency for a specific alignment condition. This resonant frequency is determined by the coil coupling, so it can be different each time a driver parks an EV. As shown in Figure 2.5, the resonant frequency is located through frequency shifting (Δfp) and phase angle comparison between current and previous angles ($\theta_{current}$ and $\theta_{previous}$). As the polarity of the phase angle cannot be detected by the measurement circuit, a direction flag *p* is utilized in the firmware to determine whether to shift the frequency to larger or smaller frequencies. The phase-angle which corresponds to the resonant frequency is zero, but the phase angle read by the DSP at the resonant frequency is not exactly zero due to the measurement error of digital devices. Therefore, the resonant frequency is set when the current phase angle ($\theta_{current}$) is lower than *t*, where *t* is a value within the range of acceptable measurement accuracy. Secondly, the WPT system determines the uniform gain frequency once the resonant frequency is known. The tuning program increases the frequency step by step (Δf) while measuring the load phase angle. The resonant frequency acquired in the first step determines the phase angle curve (Figure 2.4b) and the mutual inductance between the two coils can be calculated according to Equation (2.1). Once the mutual inductance is known, the phase angle ($\theta_{uniform}$) for the uniform gain can be obtained using Equations (2.1) and (2.5). Then the DSP program increases the switching frequency step by step (Δf) while measuring the load phase angle until the phase angle is equal to $\theta_{uniform}$. Finally, the WPT sets the switching frequency to the uniform gain frequency and raises the input DC voltage to begin charging the EV.

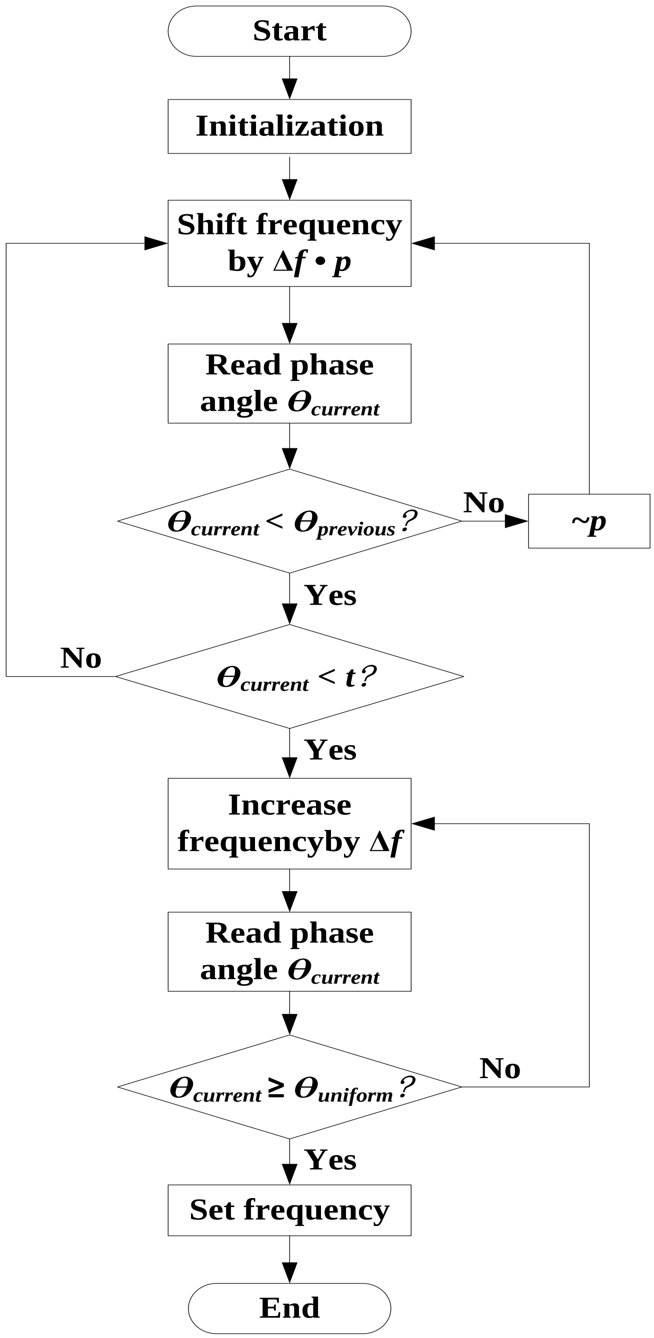

Figure 2.5. Flowchart of the uniform voltage gain control loop.

Theoretically, the calculation of the phase angle $\theta_{uniform}$ for a known coupling can be derived from Equations (2.1–5). However, a floating calculation could consume the computational resources of a 16-bit DSP dramatically and might influence the tuning speed as well. In addition, the theoretical value might have an error due to parasitic resistance and stray inductance in the electronic elements. Hence, the phase angle $\theta_{uniform}$ is calibrated for each increase (set 2 cm in our test) in misalignment and the coupling between two calibration points will linearly map the phase angle $\theta_{uniform}$.

2.7 EXPERIMENTAL VALIDATION

2.7.1 3-Axis Platform for Alignment Study

Figure 2.6 shows a three-axis motorized platform which was used to set the alignment conditions for experimental study. The three-axis platform shown in Figure 2.6 is based on a CNC machine (Model DHC, PlasmaCAM, Inc., Colorado City, CO, U.S.). It has a width of 1.75 m, a height of 1.65 m, and a depth of 1.65 m. The maximum speeds are 25 m/min in the horizontal direction and 2 m/min in the vertical direction. The movable ranges are 1.2 m × 1.2 m in the horizontal plane and 0.6 m in the vertical direction (Figure 2.6). The speed and motion trail can be programmed in a computer interface. The misalignment test was only performed in a single direction in the horizontal plane since the coil shape is circular.

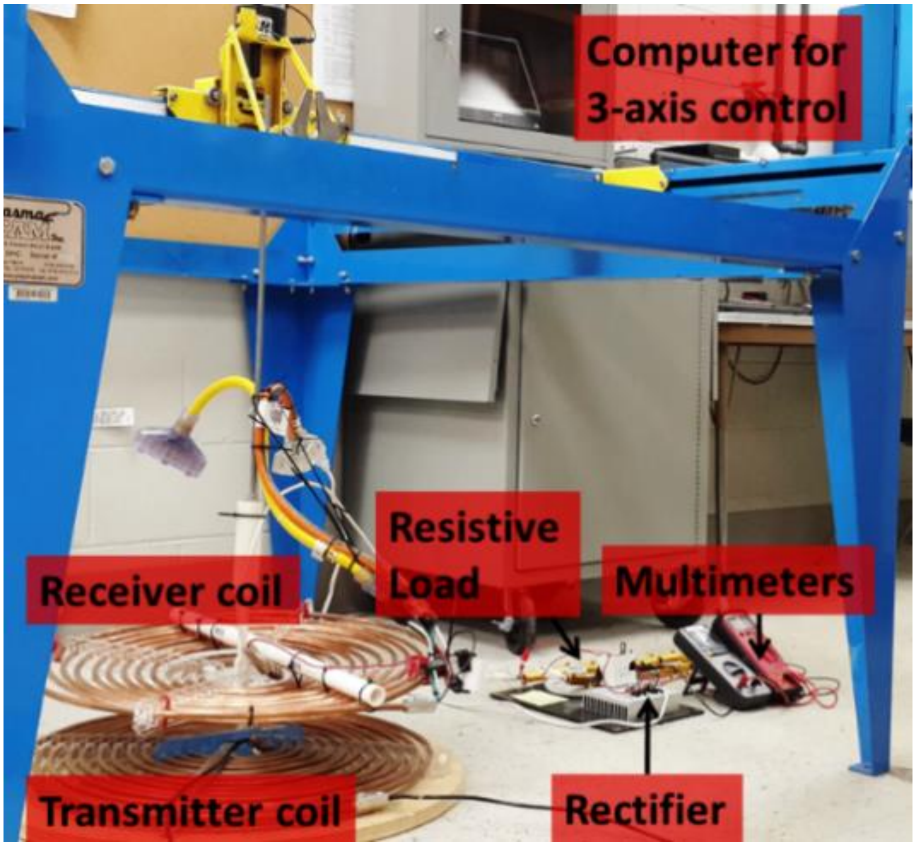

Figure 2.6. Experimental setup for misalignment study.

2.7.2. Experimental Results with Misalignment under a Constant Air Gap

While the air gap was kept at 100 mm, the efficiency and voltage gain (*G)* were measured with variance of misalignment in the horizontal plane. Figure 2.7 shows the efficiency and *G* curves under three frequency control methods, the fixed frequency, the resonant frequency, and the uniform gain control. The experiment was conducted using three input voltages: 10 V, 20 V, and 40 V, to show the influence of power losses of from switching devices on efficiency when the frequency and misalignment stay the same.

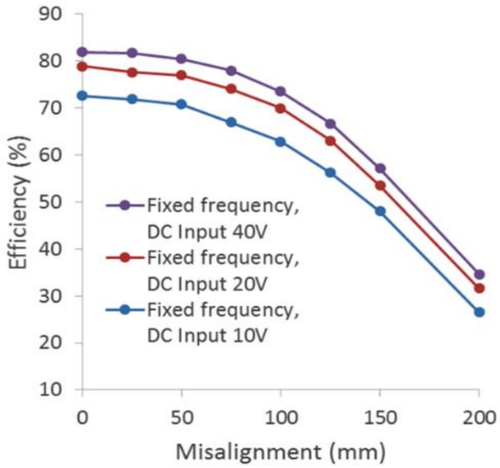
Efficiency (%)
Misalignment (mm)
Fixed frequency, DC Input 40V
Fixed frequency, DC Input 20V
Fixed frequency, DC Input 10V

(a)

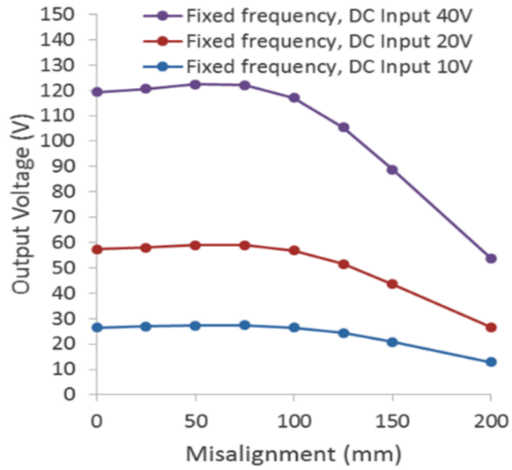
Output Voltage (V)
Misalignment (mm)
Fixed frequency, DC Input 40V
Fixed frequency, DC Input 20V
Fixed frequency, DC Input 10V

(b)

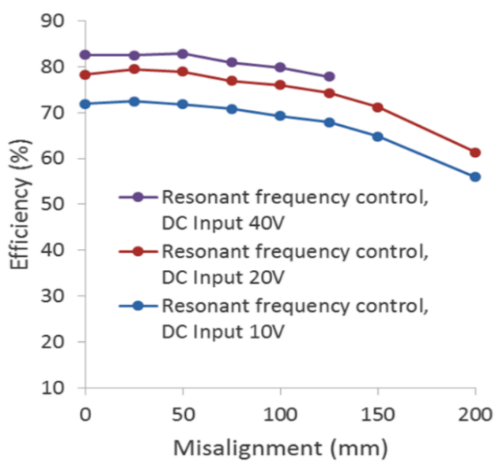
Efficiency (%)
Misalignment (mm)
Resonant frequency control, DC Input 40V
Resonant frequency control, DC Input 20V
Resonant frequency control, DC Input 10V

(c)

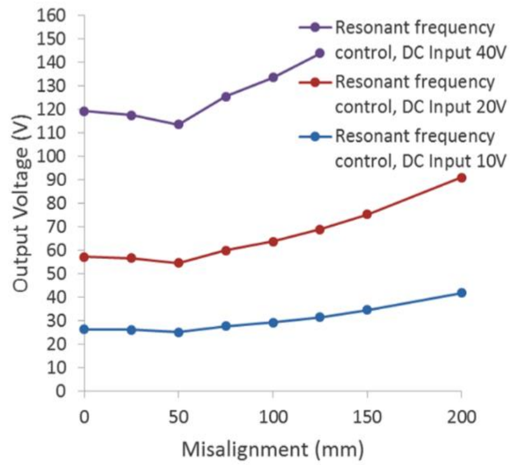
Output Voltage (V)
Misalignment (mm)
Resonant frequency control, DC Input 40V
Resonant frequency control, DC Input 20V
Resonant frequency control, DC Input 10V

(d)

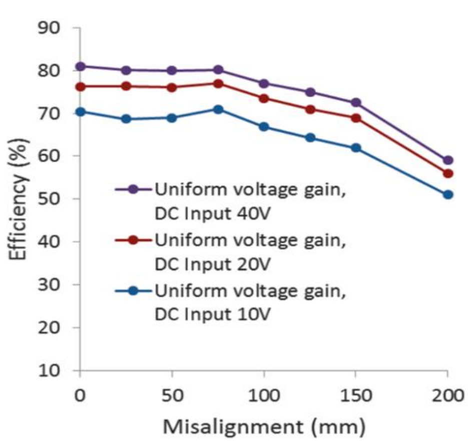
Efficiency (%)
Misalignment (mm)
Uniform voltage gain, DC Input 40V
Uniform voltage gain, DC Input 20V
Uniform voltage gain, DC Input 10V

(e)

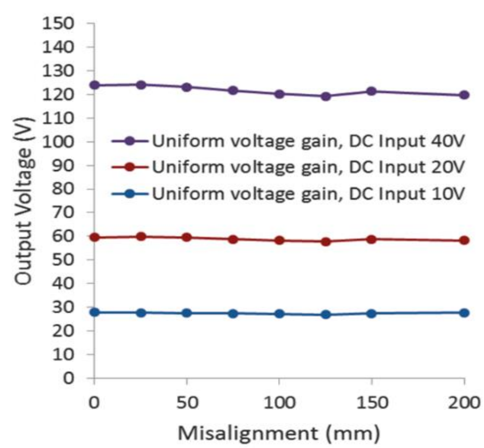
Output Voltage (V)
Misalignment (mm)
Uniform voltage gain, DC Input 40V
Uniform voltage gain, DC Input 20V
Uniform voltage gain, DC Input 10V

(f)

Figure 2.7. Experimental comparison in three control modes at a fixed air gap of 100 mm and different misaligned coil conditions. (a) Efficiency at a fixed frequency; (b) Voltage at a fixed frequency; (c) Efficiency at resonant frequencies (phase angle θ = 0); (d) Voltage at resonant frequencies (phase angle θ = 0); (e) Efficiency at uniform gain frequencies; (f) Voltage at uniform gain frequencies.

As shown in Figure 2.7a,c,e, the efficiency of resonant frequency and uniform gain control is better in misalignment than that of fixed frequency control. The efficiency at resonant frequency in different misalignment conditions is slightly higher than the uniform gain's efficiency. For example, at a DC input voltage of 40 V, the efficiency of fixed frequency control dropped from 82% to 67% when the misalignment was changed from 0 to 125 mm, while the efficiency of resonance control dropped from 82% to 79%, and the efficiency of uniform gain control dropped from 81% to 77%. It was noted that the efficiency curve of 40 V input was unavailable after the misalignment exceeded 125 mm in Figure 2.7(c). This is because the mutual inductance between two coils was too small, which led to a much smaller impedance under resonance. The DC supply could not support such a heavy load. From the efficiency curves in Figure 2.7a,c,e, the efficiency under different DC inputs is different even at the same misalignment value. This phenomenon occurs when the switching device's loss occupies a relatively larger portion of the total consumed power when operating in a low power condition. The efficiency can still increase if the DC input is greater than 40 V.

According to the voltage gain characteristics in Figure 2.7b,d,f, the output voltage at the secondary side under fixed and resonant frequencies began to vary significantly at a misalignment of more than 100 mm. However, the output voltage gain (G = V_b/V_{in}, V_{in} is the DC input voltage of the inverter) was maintained at about 3.04 across the misalignment range up to 200 mm, which coincides well with the simulation result in Figure 2.4c. The DC output voltage V_b after the rectifier and the smoothing capacitor (Figure 2.3a) is the rectifier input RMS voltage V_2 multiplied by a constant value, specifically: $V_2 = \frac{\sqrt{3}}{2}V_b$ [3]. The theoretical peak-peak voltage gain is 4.0 (Figure 2.4c); hence the theoretical DC output voltage over DC input is 3.27, which is quite close to the measured gain.

A stable output voltage for wireless charging helps to reduce the burden on the DC-DC converter to regulate the power flow. Although operating at resonance frequency has a slightly higher efficiency than the uniform gain control, it introduces a much more complex power regulation issue in comparison to the uniform gain control. Moreover, since the overall impedance under resonance frequency operation is very small for a large misalignment, the circulating current in the coils is extremely high and the power supply faces a huge challenge to drive the heavy load.

2.7.3. Experimental Results with Air Gap Variations under Zero Misalignment

When both the primary and secondary coils were in perfect alignment, the efficiency and voltage gain (G) were measured with a variance of air gaps. Similar to the misalignment experiment, Figure 1.8 shows the efficiency and *G* curves under three frequency control methods: fixed frequency, resonant frequency, and uniform gain control.

The experimental results for air gaps (Figure 2.8) followed the same trend in efficiency and voltage gain with the results shown in Figure 2.7, due to the fact that both misalignment and air-gap variation change the magnetic coupling. The relative error for output stability under the uniform voltage control was 2.0% for misalignment (Figure 2.7) and 4.7% for air gap variations (Figure 2.8). One interesting phenomenon is that the efficiency of uniform gain control (Figure 2.8e) dropped more gradually than that of the resonant control when the air gap was more than 100 mm. As the coils used for EV charging are relatively large in dimension, they are more tolerant to misalignments than air gap variations. Thus, an air gap variation causes a worse coupling compared with the same amount of misalignment in this case. The worse coupling represents a heavier overall load that needs a larger current from the inverter, which results in more conduction losses in switching devices and lowers the efficiency more quickly. Figure 2.8 a,c,e demonstrates that the efficiency varies under different DC inputs but the same frequency method and misalignment condition. Since the switching device's loss accounts for a higher percentage of the total consumed power when operating in a low power condition *versus* a high power condition, a lower DC input can make the WPT less efficient compared with a higher DC input. Figure 2.8b shows that the output voltage at an air gap of 50 mm is much lower than that of 100 mm. Since 100 mm is assumed a nominal operation gap for EV charging in our setup, the switching frequency is chosen based on the 100 mm gap for fixed frequency control. Therefore, although the wireless charging system has a stronger coupling at an air gap of 50 mm than 100 mm, the mistuned frequency causes the huge output voltage drop when the gap is 50 mm.

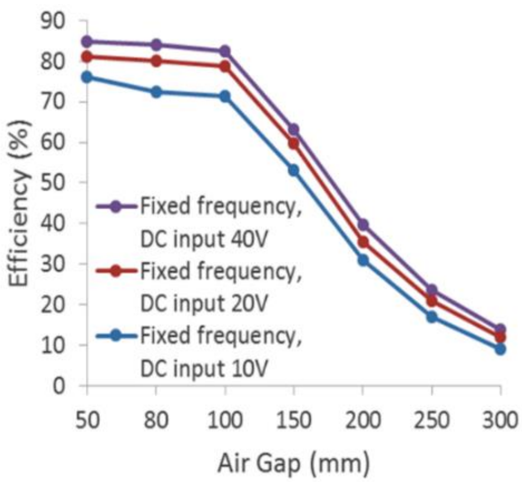

(a)

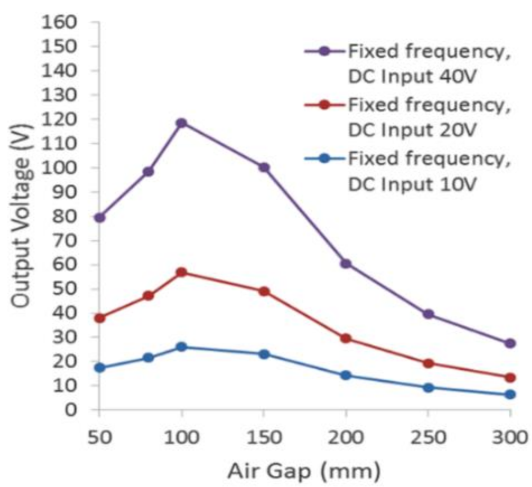

(b)

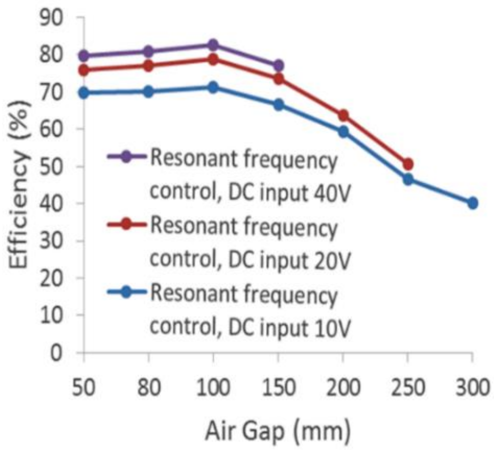

(c)

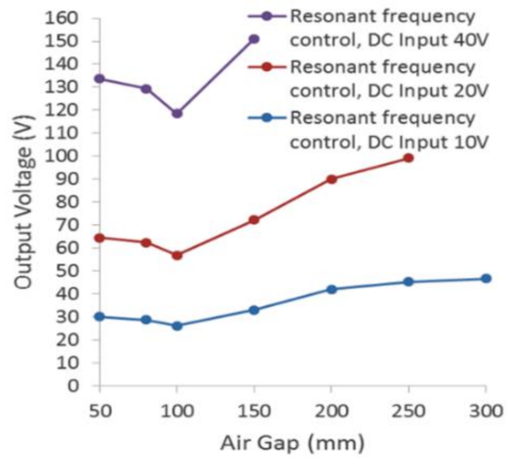

(d)

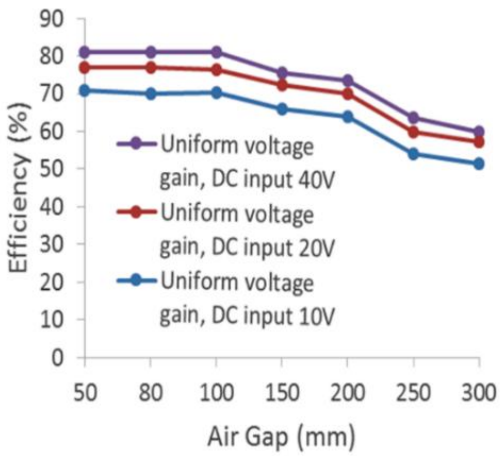

(e)

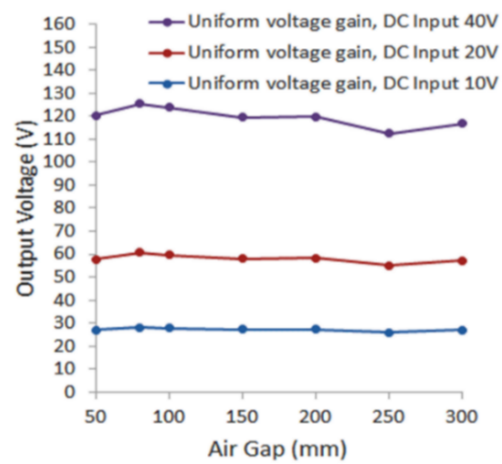

(f)

Figure 2.8. Experimental comparison in three control modes with different air gaps and no coil misalignment. (a) Efficiency at a fixed frequency; (b) Voltage at a fixed frequency; (c) Efficiency at resonant frequencies (phase angle θ = 0); (d) Voltage at resonant frequencies (phase angle θ = 0); (e) Efficiency at uniform gain frequencies; and (f) Voltage at uniform gain frequencies.

2.7.4. Accuracy of Frequency Tracking

Figure 2.9 shows the comparison between theoretical and actual operating frequencies. The theoretical switching frequencies were calculated with Matlab using Equation (2.5) and the acquired frequency was experimentally obtained by the proposed control method using a DSP controller. The difference between the theoretical and actual values ranged from 0.8 to 1.1 kHz, and all the acquired frequencies were lower than the theoretical ones. Since the inverter and rectifier were considered ideal switching devices in the circuit model and the equivalent resistance of coils was not considered, as shown in Figure 2.3(c), the actual switching frequency is different from the theoretical one. Due to the error analysis of voltage gain as stated above, such frequency tracking error should be acceptable in a practical application.

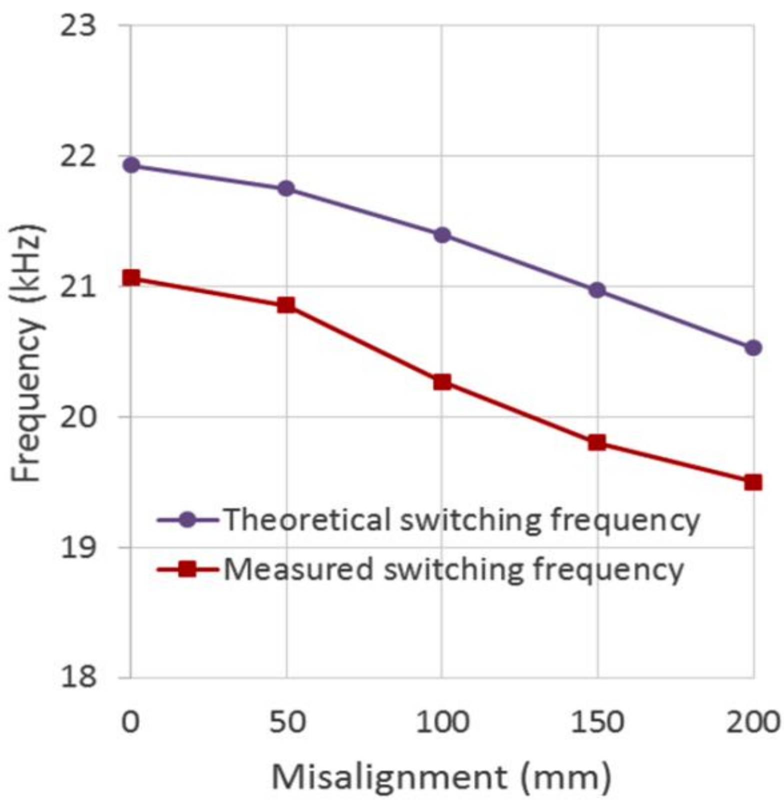

Figure 2.9. The theoretical and acquired switching frequencies for uniform voltage gain control with various couplings (misalignment at an air gap of 100 mm).

2.7.5. Frequency Control at a Large Misalignment

Figure 2.10 shows the primary side's circulating current and the gate drive signals when the misalignment is 200 mm and the air gap is set at 100 mm. These scope graphs are obtained under a DC input voltage of 40 V. Under these conditions, the circulating current of resonance operation is extremely high, which challenges the electronic devices and hinders heat dissipation, meaning resonant operation is impractical under severe misalignment. The phase angle between the two signals is around 56° for fixed frequency control (Figure 2.10a). Such a large phase angle results in a weak wireless power transfer capability. However, the current signal in Figure 2.10b lags slightly (about 29.3°) behind the switching signal which is also consistent with the inverter voltage. Thus, the soft-switching operation is used in the uniform gain control. The measured mutual inductance is 9.69 μH when the misalignment is 200 mm and the air gap is 100 mm. According to Figure 2.4b and Figure 2.9, the theoretical phase angle is 30.5°, which coincides well with the experimental value (about 29.3°).

Figure 2.10 also shows that the RMS current of fixed frequency control is 13% smaller than that of uniform gain control, while the efficiency of uniform gain control is 76.4% larger than that of fixed frequency control (Figure 2.7a,e). Therefore, the maximum allowed misalignment can be significantly extended with help of the uniform gain control. The power delivery of the uniform gain control performs much better than the fixed frequency control under severe misalignments while the resonance control cannot operate in such a weak coupling.

The current switching frequency band for light duty EV wireless chargers is 81.38 kHz–90 kHz according to the SAE-J2954 [55]. For heavy duty EV wireless chargers, the SAE currently has no such frequency recommendations due to the frequency properties of high power switching devices. As far as the authors know, the switching frequency of several commercialized wireless chargers is around 20 kHz. For instance, the Plugless wireless charging system from Evatran Group, Inc operates at 19.5 kHz [80]. Following the trend of SAE, our future demonstrations for light duty EVs will also focus on a nominal operating frequency of 85 kHz.

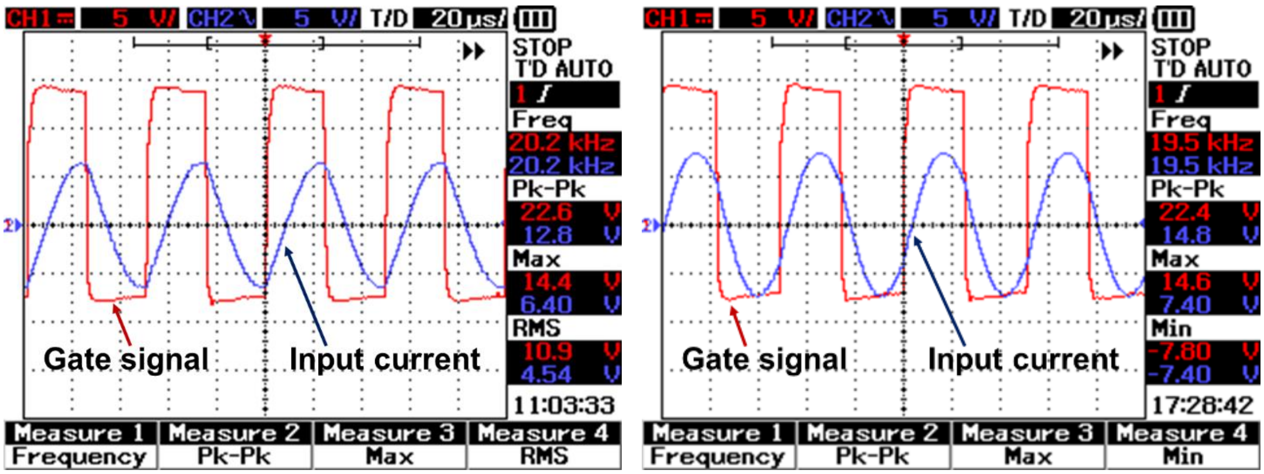

(a) (b)

Figure 2.10. Switching signals and the inverter circulating current under two extreme conditions (misalignment = 200 mm, air gap = 100 mm) (a) Fixed frequency control (20.2 kHz); Sinusoidal current waveform: Max = 32 A, RMS = 22.7 A, (b) Uniform gain operation (19.5 kHz). Sinusoidal current waveform: Max = 37 A, RMS = 26.2 A. The voltage-current ratio of the current sensor is 0.2 V/A.

2.8 CONCLUSIONS

A uniform voltage gain control for wireless charging can generate a stable and controllable voltage to address the negative effects of misalignment and air gap variations in EV applications. Simulation and experimental validation were conducted in comparison with traditional fixed frequency and resonance frequency operation. The uniform voltage gain control offers certain advantages, as shown by the theoretical analysis and experimental demonstration. Firstly, the uniform gain control allows for operation under greater misalignment and is more robust under differing vehicle chassis heights. Since the proposed control method can operate under worse magnetic couplings, it can counteract the drawback of a common circular coupler, which is that the coupling coefficient drops relatively quickly. Secondly, although the WPT system does not operate at the resonance frequency under uniform control, it does not mean the overall efficiency is low. Lower current operation and use of soft switching can decrease the power loss caused by switching devices, and hence uniform gain control has a competitive or even higher efficiency compared to resonant operation. Thirdly, the stable voltage output under uniform gain operation can decrease the design requirements of a DC-DC converter on the secondary side. Potentially, a battery could be directly charged without the existence of the DC-DC converter using the proposed gain control plus duty-cycle regulation. This could decrease the amount of electronic components involved in wireless charging.

CHAPTER 3

FREQUENCY-SPACING MODELING [2,3]

[2] Gao, Yabiao, Kathleen Blair Farley, Chen Duan, Antonio Ginart and Zion Tsz Ho Tse. "Calculating Unity-gain Frequency of Inductive Charging through Coil Dimension and Air Gap," Electronics Letters, 2016, 52(2): 145-146.

Reprinted here with permission of the publisher.

[3] Gao, Yabiao, Antonio Ginart, Kathleen Blair Farley, and Zion Tsz Ho Tse. “Frequency-gap Modeling of a Symmetrical Series-series Compensated Inductive Power Transfer System,” Submitted to IEEE Energy Conversion Congress and Exposition (ECCE), 01/24/2016.

3.1 ABSTRACT

The switching frequency of inductive charging can change along with the air gap between two coils due to mutual inductance variation. Traditionally, the mutual inductance is acquired through experimental measurement, finite element analysis, or frequency tracking control. In order to simplify this process, a frequency-gap model for series-series inductive power transfer is proposed to calculate the unity-gain frequency as long as the air gap and coil dimensions are known. Neumann's formula is applied to compute the mutual inductance of two coils. The experimental results show that the unity-gain frequency can be predicted with varying loads and air gaps (75mm to 250mm), and a demonstrated unity-gain error of <6%.

3.2 INTRODUCTION

Inductive power transfer (IPT) is used to charge electric vehicles, medical implants, and consumer electronics due to its safety and non-contact manner [7, 39]. The switching frequency at which IPT operates is important due to the principle of magnetic resonance. The unity-gain frequency of IPT is defined as a load-independent frequency which allows the secondary side's output voltage magnitude to equal the primary inverter's voltage magnitude [39]. The unity-gain operation of IPT works similarly to wire electricity transmission. However, the unity-gain frequency for IPT varies as the air gap changes because the size of the air gap influences the magnetic coupling between the primary and secondary coils.

Traditionally, the frequency of IPT is obtained by measuring/simulating the mutual inductance and calculating the frequency, or by using a frequency tracking control system through phase-angle feedback and communication with the secondary side [39, 61, 91]. These approaches are either complex or timing consuming. This paper proposes a direct way to calculate the unity-gain frequency based on the physical dimensions of the primary and secondary coils.

3.3 FREQUENCY-GAP MODELLING

The Neumann formula is used to calculate the mutual inductance between two circular wire loops [93]. Equation 3.1 is the Neumann formula for mutual inductance.

$$M = \frac{\mu_0}{4\pi} \oint_p \oint_s \frac{d\vec{p} \cdot d\vec{s}}{r} \tag{3.1}$$

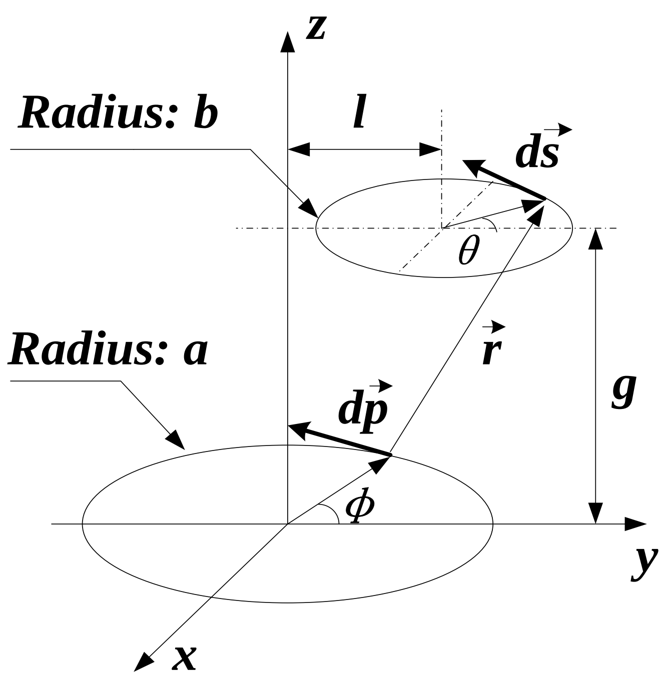

Figure 3.1. Spatial configuration for each set of wire loops.

According to Figure 3.1, we have

$$\begin{aligned} d\vec{p} &= a(-\sin\phi \vec{x} + \cos\phi \vec{y}) d\phi \\ d\vec{s} &= b(-\sin\theta \vec{x} + \cos\theta \vec{y}) d\theta \\ d\vec{p} \cdot d\vec{s} &= ab \cos(\phi - \theta) d\phi d\theta \end{aligned} \tag{3.2}$$

From Figure 3.1, the distance r is

$$r = \sqrt{a^2 + b^2 + g^2 + l^2 - 2ab\cos(\phi - \theta) - 2al\cos\phi + 2bl\cos\theta} \tag{3.3}$$

where a is the radius of the primary coil, b is the radius of the secondary coil, *l* is the lateral distance, and g is the distance between the two concentric coils (Figure 3.1). Φ is the corresponding angle of integration variable of the primary while θ is the angle of the secondary.

Combining equations (3.1)-(3.3), and using Newton's generalized binomial theorem to expand the integral expression up to the sixth order, the simplified mutual inductance between the two wire loops can be expressed as

$$M = \frac{\mu_0 \pi a^2 b^2}{16\rho^3}\left(\begin{array}{l} 1 - \frac{3l^2}{8\rho^2} + \frac{15(a^2b^2 + 8al^3 + 8b^2l^2 + 8bl^3)}{128\rho^4} - \frac{35l^4(a^2+b^2)}{256\rho^6} \\ + \frac{315(a^4b^4 + 3a^4l^4 + 3b^4l^4 + 6a^4b^2l^2 + 6a^2b^4l^2)}{16384\rho^8} \end{array}\right) \tag{3.4}$$

where $\rho = \sqrt{\frac{a^2 + b^2 + g^2 + l^2}{4}}$ and μ_o is the magnetic constant.

The formula deduction can be simpler and up to the seventh order if two coils are coaxially placed (*l* equals to zero), then it can be simplified as

$$M = \frac{\mu_0 \pi a^2 b^2}{16\rho^3}\left(1 + \frac{15a^2b^2}{128\rho^4} + \frac{315a^4b^4}{16384\rho^8} + \frac{15015a^6b^6}{4194304\rho^{12}}\right) \tag{3.5}$$

Since the coils used for IPT commonly include multiple turns of wire loops, the mutual inductance between two planar coils is a sum of all the possible combinations of single wire loops. Thus, the total mutual inductance between the two circular coils is

$$M_{total} = \sum_{i=1}^{n_p}\sum_{j=1}^{n_s} M_{ij} \tag{3.6}$$

where n_p and n_s are the number of turns of the primary and secondary coils. For unity-gain operations, both the primary and secondary coils have the same dimensions, so $n_p = n_s$. M_{ij} is the mutual inductance between the primary's number *i* loop and secondary's number *j* loop.

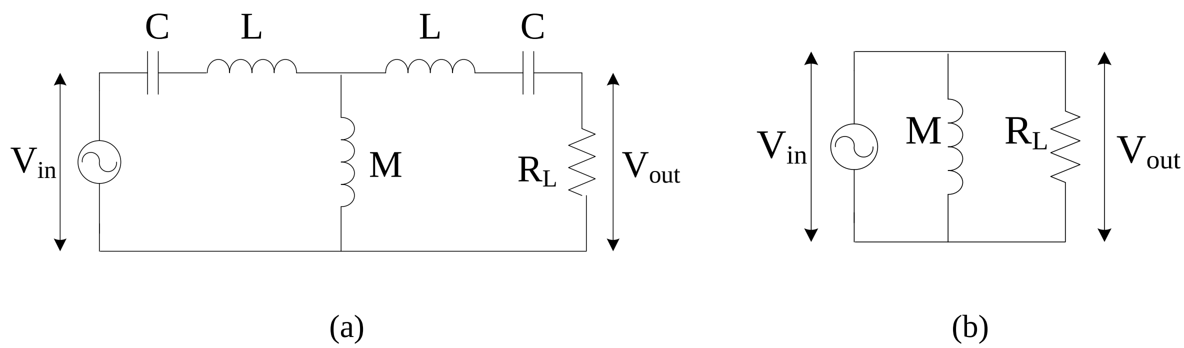

Figure 3.2. Circuit model of symmetrical SS resonant tank. (a) Equivalent circuit of SS IPT; (b) Simplified circuit at the unity-gain frequency f_u

Figure 3.2 shows the simplified circuit model of a symmetrical SS resonant converter of IPT for the unity-gain operation. Although there are two load-independent resonant frequencies that meet unity-gain operation for symmetrical SS IPT [39, 94], the unity-gain frequency expressed in equation (3.7) is preferred because it has the maximum power transmission efficiency for SS IPT [94]. The leakage inductance of the coupled coils is fully compensated at this frequency. Therefore, the circuit can be further simplified as shown in Figure 3.2b, resulting in minimal voltage across the mutual inductance and thus minimum circulating current in the coil. A minimum current in the coupler indicates that it operates at maximum power transfer efficiency.

$$f_u = \frac{1}{2\pi\sqrt{LC}} \tag{3.7}$$

3.4 EXPERIMENTAL VERIFICATION

An IPT system was built to verify the frequency-gap model. As shown in Figure 3.3, it consists of a full-bridge inverter, primary and secondary coils, compensating capacitors, and resistive loads. The compensating capacitance is 2.0 μF in both the primary and secondary sides. The coil specification is shown in Table 3.1. The resistive load was set at 12Ω, 36Ω, and 90Ω separately for each air gap. The air gap varied from 75mm to 250mm and data was recorded for each incremental step of 25mm. The DC input voltage of the inverter was set at 40V during the experiment.

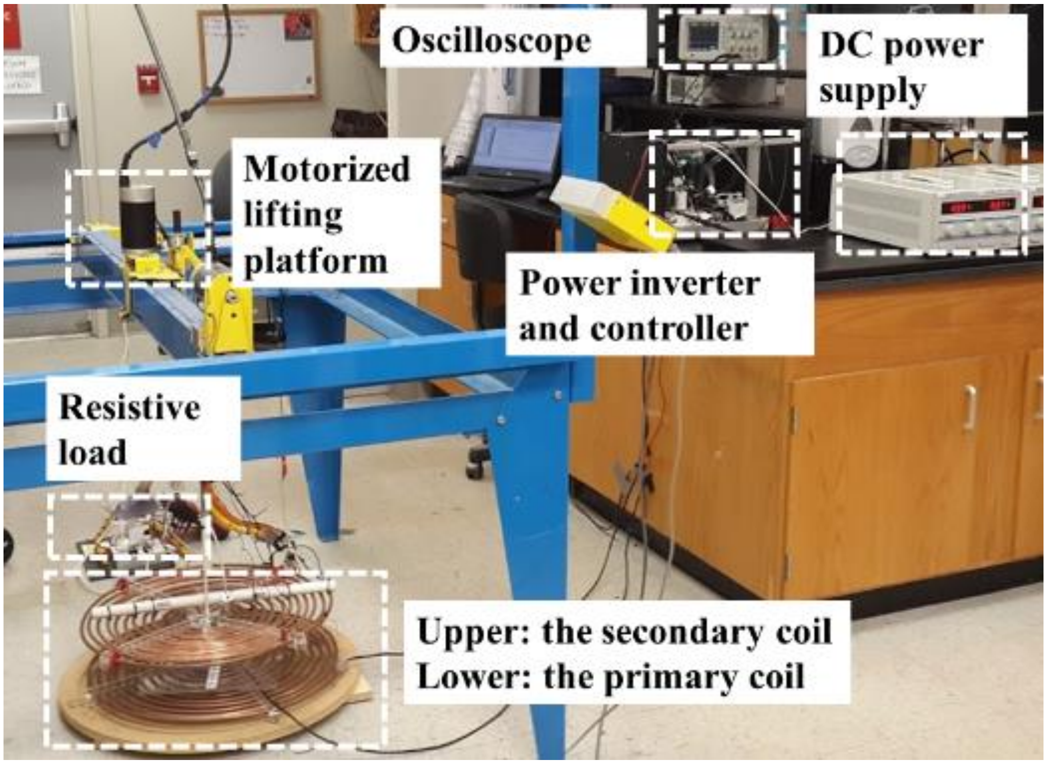

Figure 3.3. Automated positioning system and coil setup

Table 3.1. Specification of primary and secondary coils (unit: mm).

Parameters	Value	Parameters	Value
No. of turns	12	Coil track separation	10.9
Outer coil diameter	560	Coil track width	9.5

Figure 3.4a shows the unity-frequency calculated by Matlab using the frequency-gap model. Figure 3.4b compares the mutual inductance between the primary and secondary coils obtained by measurement and computation via the model. The average difference between the measured and computed values for the eight air gaps is 0.43μH (STD: 0.27μH). The maximum difference is 1.02 at the air gap of 75mm. The minimum difference is 0.14 μH at the air gap of 175mm. Figure 3.4c is the actual gain at computed unity-gain frequencies (Figure 3.4a) for three different

loads. The gain changes from 0.94 to 1.05 for all twenty-four load and air-gap configurations with an average gain of 0.98 (STD: 0.04). Figure 3.4d shows that the gain variation at each air gap is lower than 3% for all three load conditions, and the gain change is zero when the air gap is either 200mm or 250mm, indicating that the output voltage can stay quite stable for different loads at the same air gap.

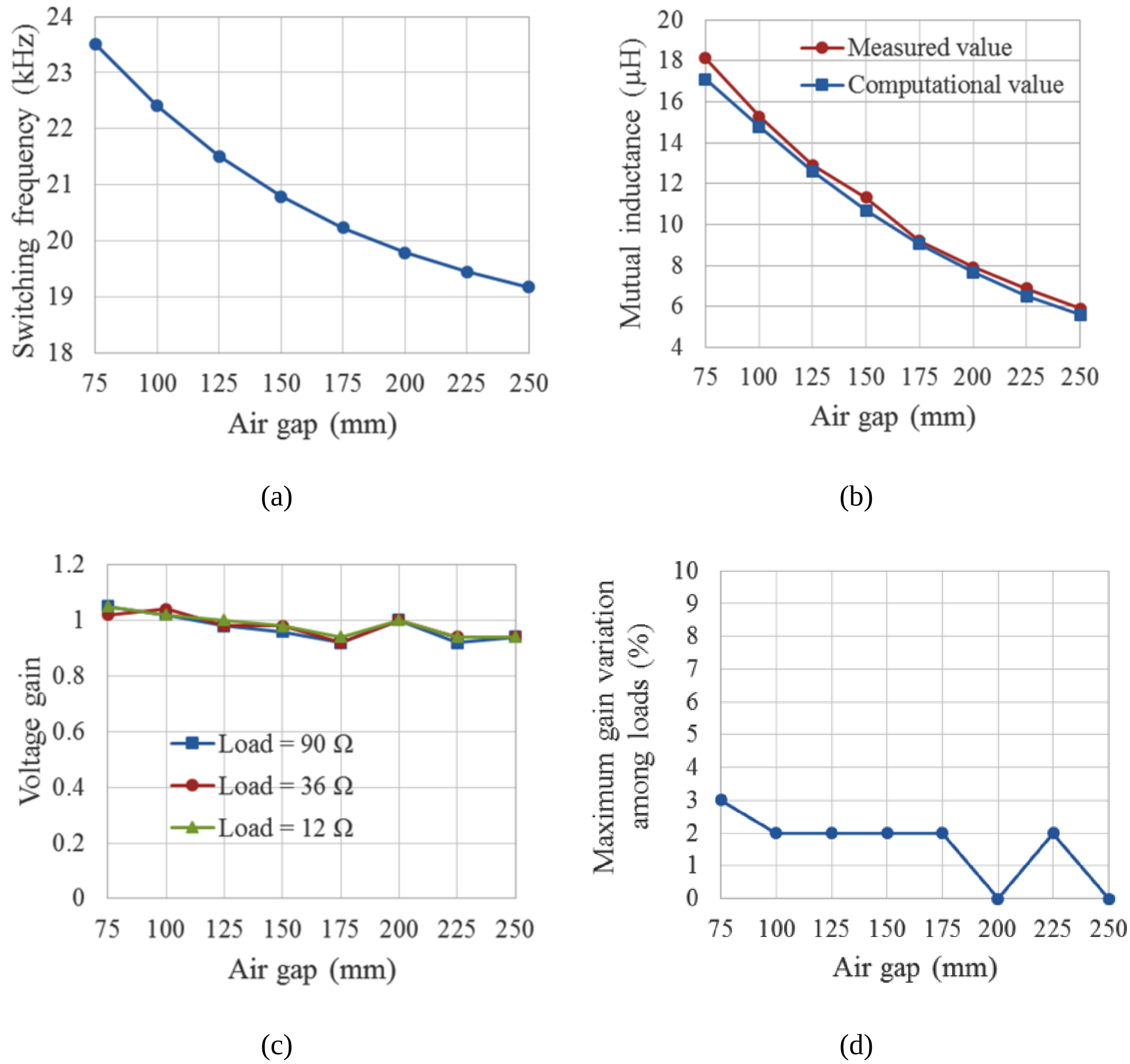

Figure 3.4. Experimental results based on frequency-gap model. (a) Switching frequency at various air gaps; (b) Comparison of measured and computed mutual inductance; (c) Measured

voltage gain at various air gaps; (d) Gain stability among three resistive loads at each air gap.

The computational time to calculate the unity-gain frequency by Matlab was recorded for eight air gap conditions from 75mm to 250mm with an increment of 25mm. The Matlab program has an average runtime of 9.79ms (STD: 0.25ms), meaning that the proposed approach has higher computation efficiency in comparison with finite element software.

3.5 CONCLUSION

The proposed frequency-spacing model allows the unity-gain frequency of a SS IPT system to be computed in about 10ms. This process requires no measurement or finite element analysis to acquire the mutual inductance in IPT; it is a direct way to calculate the unity-gain frequency. The frequency-gap model can also take into account air gap variations. The average gain value for all twenty-four configurations in the experiment is 0.98, and the gain stability at any air gap is within 3% under three different loads.

CHAPTER 4

MAGNETIC ALIGNMENT DETECTION [4]

[4] Gao, Yabiao, Aleff Antonio Oliveira, Kathleen Blair Farley, Zion Tsz Ho Tse. "Magnetic Alignment Detection Using Existing Charging Facility in Wireless EV Chargers," Journal of Sensors, vol. 2016, Article ID 5670510, 9 pages, 2016. doi:10.1155/2016/5670510

Reprinted here with permission of the publisher.

4.1 ABSTRACT

Wireless charging is a promising outlet to promote the electric vehicle (EV) industry due to its safe and non-contact manner. Wireless EV chargers require the secondary receiver coil to be well aligned with the primary station for efficient charging, which could require more of the driver's time and attention when parking a vehicle. Therefore, this paper presents a magnetic alignment system to assist the EV driver during parking. The magnetic alignment approach uses the existing coil and frequency tracking control electronics of wireless chargers to detect the distance between the two coils while using 4 small auxiliary coils for direction and fine adjustment, leading to a cost effective detection method for coil alignment in electric vehicle wireless charging (EVWC). The testing results of a prototype shows acceptable measurement correctness and the mean error for ten trials in range detection is within 0.25 cm at three different misalignment conditions (10.5, 15, and 20cm). The positioning accuracy of coil alignment is within 1.2cm for three different start positions with the auxiliary coils.

4.2 INTRODUCTION

Over the past decade, pure electric vehicles (EVs) and plug-in hybrid electric vehicles (PHEVs) have increased in popularity due to environmental awareness and fossil fuel price fluctuations [7, 16, 39, 44, 61]. Wireless charging is a competitive option to overcome the inconvenience of plug-in EV charging and the relatively low energy density stored in batteries by opportunity charging [44]. A wireless EV charger typically includes power electronics that convert the grid power to a high frequency power source: the primary coils placed/buried on ground, the secondary coil mounted underneath the chassis of the EVs, on-board electronics that rectify the secondary output to charge the EV battery, and a communication module between ground facility and the on-board electronics [3].

The efficiency of wireless charging highly relies on the alignment condition between the two charging pads [95, 96]. The wireless EV chargers can commonly tolerate a misalignment error of only 10cm, which presents a challenge to EV drivers while parking over a wireless charging station [97]. Birrell et al. investigated the effects of drivers' behavior and parking alignment on wireless chargers [97]. According to their study, the mean longitudinal misalignment is more than 70cm when the drivers parked over a wireless charging pad with no guidance from external support. The study also shows that only 5% of EVs can park well enough to achieve efficient wireless charging. Since the wireless chargers can only endure limited misalignment, advanced frequency control methods and coupler design have been investigated with the goal to improve the alignment flexibility for EV wireless charging. These advanced design indeed have better performance than a common one. However, it still cannot compensate for parking errors greater than 0.7m (which is greater than the diameter of the coils). Hence, a vehicle alignment system should be a necessary sub-system of wireless EV chargers. Additionally, the alignment system has been seen as an essential module of wireless EV chargers in the newly released SAE technical standards (SAE-J2954) [55].

To the best of the authors' knowledge, the magnetic method is the best option for alignment detection. It uses the existing coil to generate a weak magnetic field that is detected by magnetic sensors installed on the secondary side. Although RF positioning can meet the accuracy requirement of alignment control, more than one RF antennae need to be fixed on the primary side, which potentially increases its cost and leads to a complex system. Other potential detection methods include RFID positioning, GPS, optical detection, mechanical stop, and mechanical arm. The accuracy of RFID is more than 50cm which is inaccurate for alignment. The cost becomes increasingly high if the pressure sensors are buried underground. Machine vision seems promising in vehicle alignment. However, it cannot work if the charging stations are covered with snow in winter. The GPS signals are unavailable sometimes, and the positioning accuracy is limited to 5m [98]. The mechanical stop is large in size, and cannot support automated alignment control, while using a mechanical arm will increase the cost, and make the system more complex.

There is currently still limited literature available regarding the design of an alignment system for wireless EV chargers. Ni et al. presented a conceptual radio alignment system for EV wireless charging [99]. The system applied eight radio nodes with four on the ground and the other four mounted underneath the secondary pad to sense the relative position between the primary and secondary coils. The radio nodes used by the system is based on an indoor ranging technique called wireless ad hoc system for positioning (WASP), which operates in 5.8-GHz ISM band with a bandwidth of 125 MHz, and achieves a distance measurement error of about 0.2 m. Chen et al. introduced an alignment system using sixteen reference RFID tags and two readers placed on ground, and one tracking tag attached to the vehicle [100]. Although the radio alignment method is an alternative option for EV wireless chargers, it can increase the system complexity and thus result in a high-cost wireless charging system. The price of each commercial radio reader can be as high as several thousand dollars, which surpasses the cost of the basic charging electronics. For example, the current price of a commercialized 3.3 kW plugless wireless EV charger is as low as $1260 for Chevy Volt [101]. Therefore, the radio alignment system might encounter cost issues in an open market where the configuration that meets requirements with minimal cost survives. Moreover, the additional operating frequency band of the radio positioning system could possibly cause electromagnetic interference issues.

This paper introduces a magnetic sensing system for alignment in wireless EV chargers. The system utilizes the existing charging facility to generate a magnetic field and sense the relative distance between the two coil centers. The system also requires four minor coils to be installed on the secondary pad for direction detection using triangulation. The four small coils are also able to adjust the alignment when the two major coils are close enough, ensuring the primary and secondary pads well aligned.

4.3 OVERVIEW OF MAGNETIC ALIGNMENT FOR WIRELESS EV CHARGING

Figure 4.1(a) illustrates the components of the wireless charging system used for alignment detection. Since the phase angle between output voltage and current of the inverter changes along with the operating frequency and coil spatial distribution, the distance between the primary and secondary coils can be measured by the phase angle feedback and the WPT system's frequency characteristics on misalignment. The digital signal processor (DSP) controller switches the frequency of pulse width modulation (PWM) signals and acquires phase-angle signals and charging information from the vehicle side via wireless communication. Two half-bridge insulated gate bipolar transistor (IGBT) modules (FF100R12K4, Infineon) are employed to form the H-bridge that drives the transmitter coil to generate high-frequency electromagnetic fields. The voltage/current induced in the receiver is rectified to DC to power the load or charge a battery. A National Instrument (NI) Data Acquisition (DAQ) card (NI CompactRio-9075) with wireless communication modules is used to transmit the data from the primary to the secondary side wirelessly. A user interface is developed in LabVIEW to display the alignment information for the driver while parking.

Figure 4.1(b) shows the mechanical schematic of the secondary coil. The four minor coils can detect its distance from the primary center when the two coils begin to overlap. Since the actual magnetic field strength and distribution is always different from the computational value, the minor coils' output distance is outputted by matching the immediate value with an experimentally acquired data space. This scenario is used when the two big coils are close enough with each other that the big-coil's detection limit might not be effective. The use of four coils allows the system to determine whether the driver needs to move left, right, forward, or backward. The zero misalignment occurs when the relative value of the four nodes is 0. The four small coils are mounted symmetrically.

Figure 4.1 is the existing hardware for wireless charging except for the four minor coils and an ultrasonic sensor (MaxSonar-EZ2, MaxBtixInc, Brainerd, MN, USA) for height measurement. Therefore, the alignment system shares most of the electronic components with the charging facility, leading to a low-cost detection. After completion of alignment operation, the DSP controller will tune its optimal switching frequency based on the phase-angle feedback as well as the battery's state of charge, and then start charging.

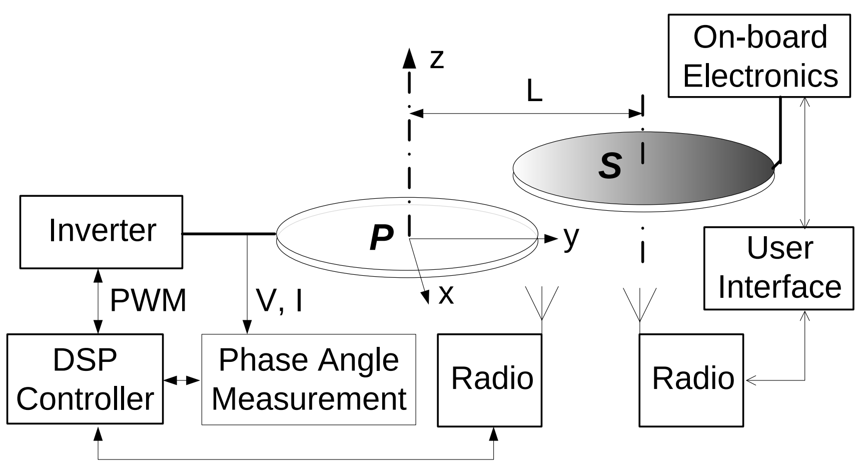

(a)

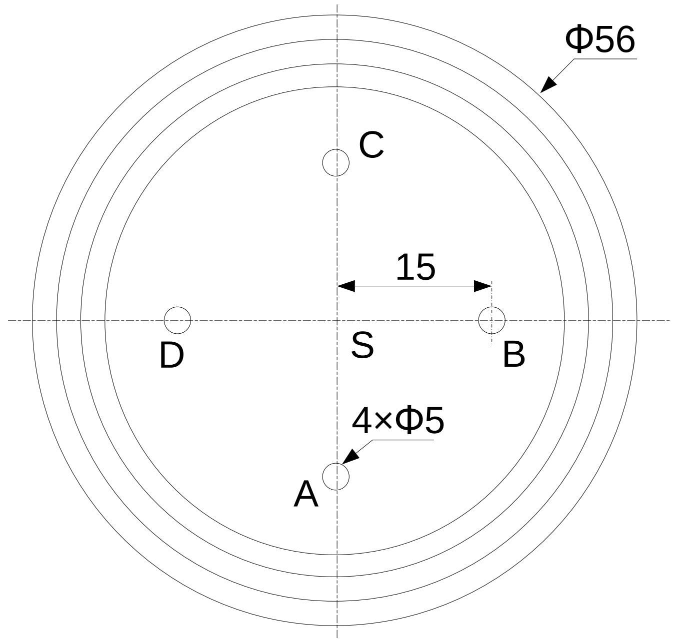

(b)

Figure 4.1. (a) Block diagram of the proposed magnetic alignment system using existing wireless charging equipment; (b) Secondary coil with four small auxiliary coils (A-D) for direction and fine adjustment (unit: cm). P is the primary center while S is the secondary center.

Figure 4.2 is a block diagram of the phase-angle measurement module. The four relays are used to isolate the power electronics from the control electronics due to the high power in wireless charging. The comparators are used to transform the output voltage (V_s) and current (I_s) signals from the inverter into two square waveforms. The phase delay between V_s and I_s is measured by an exclusive-OR gate (XOR) that combines the two square waveforms to one pulse waveform. A low-pass filter converts the pulse into a DC signal V_{phs}, then the DSP reads the voltage signal and obtains the phase angle information. The DC output of the filter is proportional to the phase angle between V_s and I_s. The DC input voltage is operated at a relatively low voltage (limited to 24V) during the vehicle alignment process, as lower voltage levels are much safer for the control electronics.

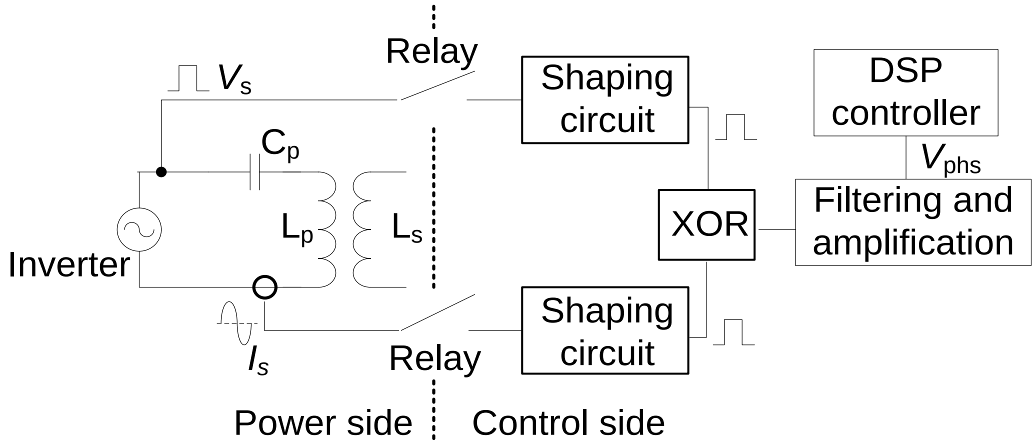

Figure 4.2. Phase-angle measurement between the inverter's output voltage and current.

In the phase angle measurement circuit, the voltage probe is directly connected to the output of the power inverter by a resistance divider. This is because the switching frequency is more than 10 kHz, and thus such high frequency makes a typical commercialized hall-effect voltage sensor unable to catch the fast response time. The AC current is measured by a current transformer. Although discrete Fourier transform (DFT) can be programmed in DSP for phase angle measurements, using an XOR and an RC filter greatly simplifies the embedded software development process and reduces the computational load of the DSP.

4.4 RANGE DETECTION USING CHARGING COILS

Figure 4.3 shows the resonant tank using series parallel topology for wireless power transmission (WPT). The primary and secondary coil both have 12 turns. The inductance of primary coil L_p is 65.3 µH and the secondary coil inductance L_s is 65.1 µH. The tuning capacitance for both sides (C_p and C_s) is 1 µF. According to the equivalent circuit shown in Figure 4.3(b), the circuit impedance Z(ω) is

$$Z(\omega) = \frac{1}{j\omega C_p} + j\omega(L_p - L_m) + j\omega L_m \, // \left(j\omega(L_s - L_m) + \frac{1}{j\omega C_s} \, // \, R_L \right) \tag{4.1}$$

where j is the imaginary unit, ω is the angular frequency, L_m is the mutual inductance between the two coils, and R_L is the equivalent resistance of the battery, which can be calculated using the delivered power and voltage across the battery. For a desired 1.4 kW/120 V battery charging condition, R_L is 20 Ω.

The coupling coefficient k is defined as

$$k = \frac{L_m}{\sqrt{L_p L_s}} \tag{4.2}$$

According to the Neumann formula, the mutual inductance is a function of coil dimension and spatial arrangement. Since the coil dimension has been determined, the coupling coefficient is a function of misalignment and air gaps. Therefore, the coil misalignment can be measured through analyzing frequency characteristics of WPT.

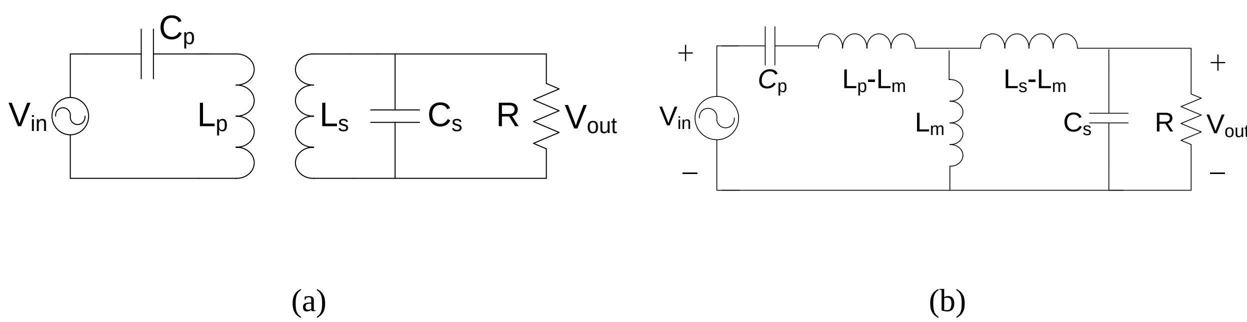

Figure 4.3. (a) Simplified circuit model of the WPT; (b) Equivalent circuit

Figure 4.4 is the simulated impedance and phase characteristics in the frequency domain with multiple coupling coefficient values. For each curve of the phase angle in Figure 4.4(b), one zero-crossing point exists, which indicates the resonant frequency. The resonant frequency varies with different coupling coefficients. Thus, the lateral distance between two coils can be obtained through adjusting the frequency until the phase-angle becomes zero. The resonant frequency indicates the lateral distance.

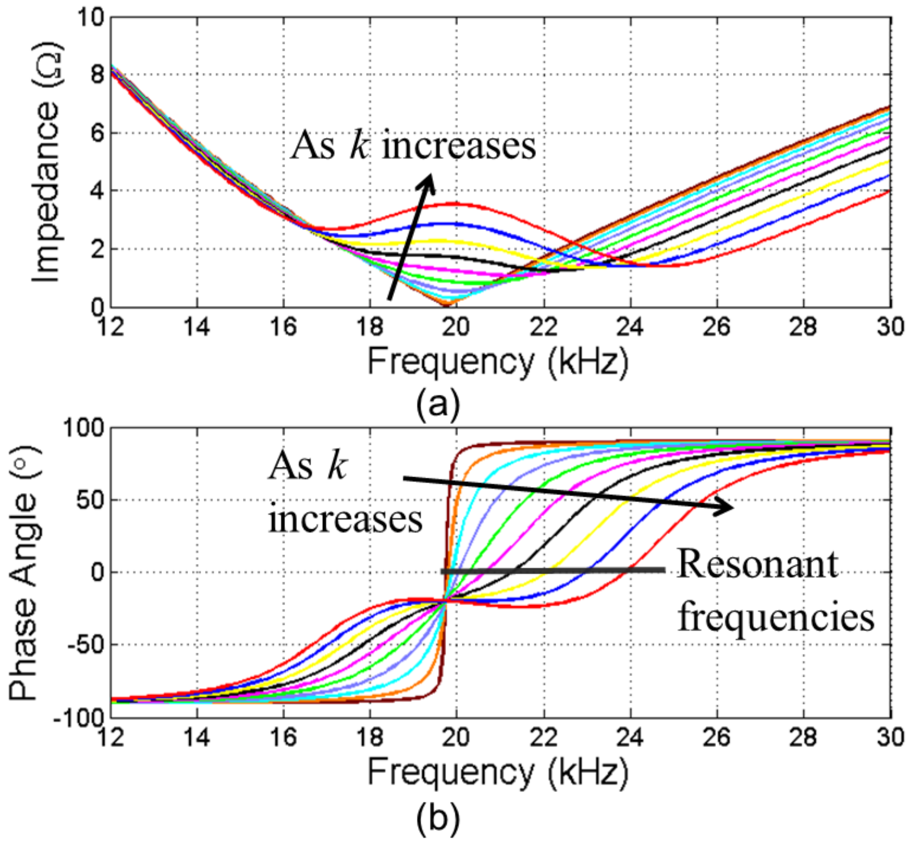

Figure 4.4. (a) Impedance magnitude across frequency domain; (b) Phase-angle across frequency domain. The parameters of the wireless charging system were L_p=65 μH, L_s = 65 μH, C_p = 1 μF, C_s = 1 μF, R = 20 Ω, and the mutual inductance L_m was assumed as 2.5, 5, 7.5, 10, 12.5, 15, 17.5, 20, 22.5, and 25 μH in the simulation.

In order for an accurate measurement, a calibration is necessary to build a data space that allows the resonant frequency to match with it. The built-in data space is composed of 25 sets of misalignments and resonant frequencies for each height. Since the vehicle chassis might be slightly varied due to tire pressure or the weight it carries, the height should be taken into account when building the data space, making it a multi-dimensional array. The calibration is conducted for each step of 1cm so the total calibrated ranging is up to 25 cm for each height. Following Figure 4.4(b), the misalignment value can be assumed to change linearly with the measured resonant frequency f between two calibration points as close as possible. Hence, the misalignment L can be obtained by

$$L = L_i + \frac{f - f_i}{f_{i+1} - f_i}, \ i \in [0, D) \tag{4.3}$$

where i is the index number of the calibrated lateral distance L_i between two coil centers, f_i and f_{i+1} are the resonant frequency when the lateral distance is L_i and L_{i+1} , and D is the calibrated range and is 25 in our experiment.

Figure 4.5(a) shows the flowchart used for lateral detection. As shown in Figure 4.5(a), the resonant frequency is located through adjusting the frequency, reading the phase angle feedback, and comparing between current and previous angles ($\theta_{current}$ and $\theta_{previous}$). The resonant frequency is obtained when the current phase angle ($\theta_{current}$) is lower than t, which is close to zero. After that, the microcontroller will match the resonant frequency with the built-in data space and calculate the lateral distance by equation (4.3).

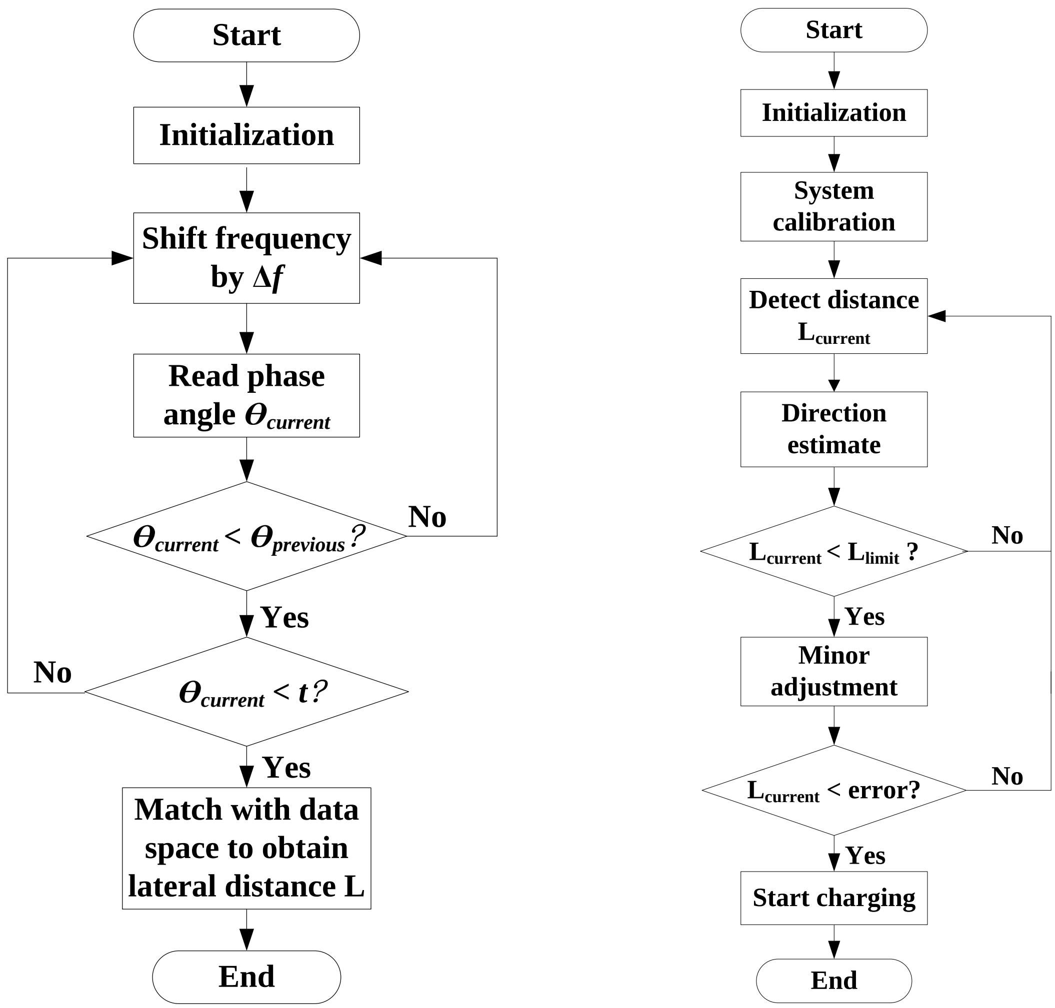

(a) (b)

Figure 4.5. (a) Flowchart for lateral distance detection; (b) Flowchart of operation planning of the magnetic alignment system.

4.5 AUXILIARY COILS FOR MINOR ADJUSTMENT

The four minor coils act as an auxiliary devices for minor adjustment to ensure the vehicle is parked perfectly. The auxiliary coil inductance is measured by a LCR meter, and the resonant capacitor is calculated by

$$C = \frac{1}{4\pi^2 f^2 L} \tag{4.4}$$

where L is the inductance of the auxiliary coil and f is the resonant frequency of the small coil. The switching frequency is assumed 20 kHz which is the proposed switching frequency of the wireless EV charger. Figure 4.6(a) shows the auxiliary coil was made in printed circuit board (PCB). Table 4.1 shows the auxiliary coil's specification.

Table 4.1. Parameters of the auxiliary coil

Specification	Auxiliary coil
Inductance (μH)	17.1
Resonant capacitor (μF)	3.7
Number of turns	10
Diameter of coil (mm)	51.5
Coil track width (mm)	1.0
Coil track separation (mm)	1.0

Figure 4.6(b) shows the circuit diagram for the four auxiliary coils. It includes an inverting amplifier, a rectifier consisting of four Schottky diodes, and a film capacitor for filtering the output voltage variations. Since the operating frequency of the wireless charging system can range from 15 kHz to 25 kHz, the electric components need to be able to operate in the frequency band. In Figure 4.5, the capacitor C_0 together with the feedback resistor adds a null end to the Bode plot of the circuit, lowering the bandwidth of the amplifier and filtering high frequency noises. The rectifier and the filtering capacitor convert the alternating current (AC) signals of the amplifier to direct current (DC) signals which are then acquired by the NI DAQ module. Because the data card faces difficulty in acquiring the high frequency signal, it is necessary to convert the signal to DC first then the data card for further processing in LabVIEW.

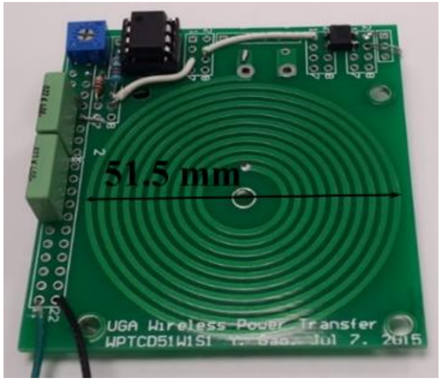

(a)

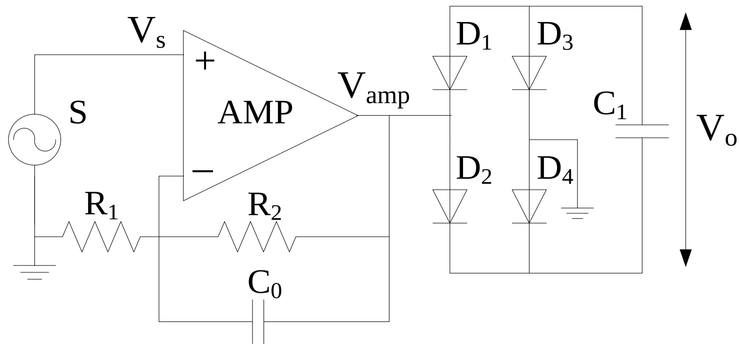

(b)

Figure 4.6. (a) A picture of auxiliary nodes; (b) Circuit diagram for auxiliary coils.

4.6 OPERATING PLAN OF THE ALIGNMENT SYSTEM

The operation plan of the alignment detection is shown in Figure 4.5(b). When the vehicle is parked, the alignment system is automatically activated from sleep mode. Firstly, the charging facility reads the vehicle height, then calibrates and chooses the appropriate built-in data array for matching purposes. Secondly, it measures and displays the immediate lateral distance $L_{current}$ and the four auxiliary coils' outputs for direction estimation. Thirdly, it compares the current lateral distance with the previous one to decide whether it is the right time to alert the driver to start minor adjustments. Finally, the charging process is initiated after both the charging pads are well aligned and the driver shifts into park and locks the transmission.

4.7 RESULTS AND DISCUSSION

4.7.1 Experimental setup

Figure 4.7(a) shows the experimental platform used to validate the magnetic sensing for alignment purposes. The 3-axis platform shown in Figure 4.7(a) is modified from a CNC machine (Model DHC, PlasmaCAM, Inc., Colorado City, CO, USA). The platform has a width of 1.75m, a height of 1.65m, and a depth of 1.65m with a maximum speed of 25m/min in the horizontal direction and 2m/min in the vertical direction. The movable ranges are 1.2m × 1.2m in the horizontal plane and 0.6m in the vertical direction. Figure 4.7(b) is the power inverter of the wireless charging and was used to drive the coil and generate a magnetic field for alignment. The user operated the control panel to adjust the coil alignment based on the computer interface's navigational information. The distance between the two coils was recorded after the user completed the test. The users did not have access to visually obtain the two coils' spatial distribution to ensure the functionality of the alignment system.

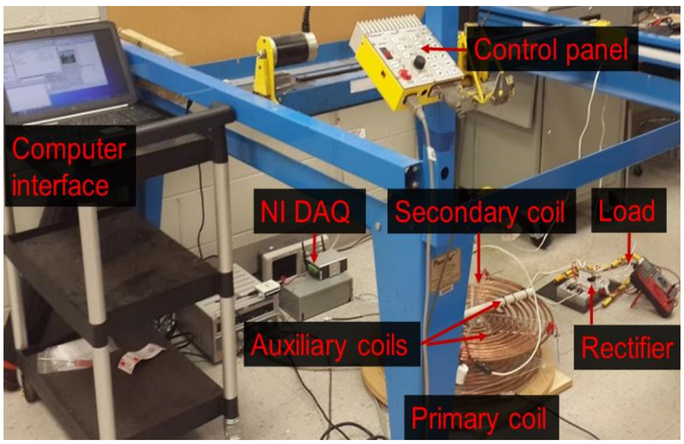

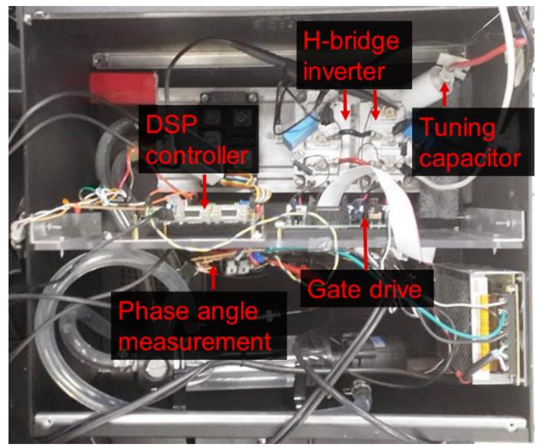

(a) (b)

Figure 4.7. (a) 3-axis platform; (b) Power inverter and frequency control electronics.

4.7.2 Experimental results with Lateral distance detection

Figure 4.8 shows the experimental comparison between measured values by the charging electronics and the true values. Figure 4.8(a) is the experimental result when the coil air gap is 12cm and Figure 4.8(b) is the result when the gap is 11.5cm. The mean error is 0.2cm in Figure 4.8(a) while it is 0.34cm in Figure 4.8(b). As the system was calibrated at an air gap of 12cm, the system shows more accurate measurement at 12cm than 11.5cm. The measurement error is relatively higher when the two coils are very close together (<2 cm). This is because that magnetic coupling is similar when the two coils are almost strictly aligned. In this case, the resonant frequency of the WPT system varies little, making the system have relatively low sensitivity when the charging coils are in close to perfect alignment. Since the wireless charging system can endure some misalignment, the alignment can still meet the requirements as long as the navigation error is lower than 10cm for a common wireless EV charger.

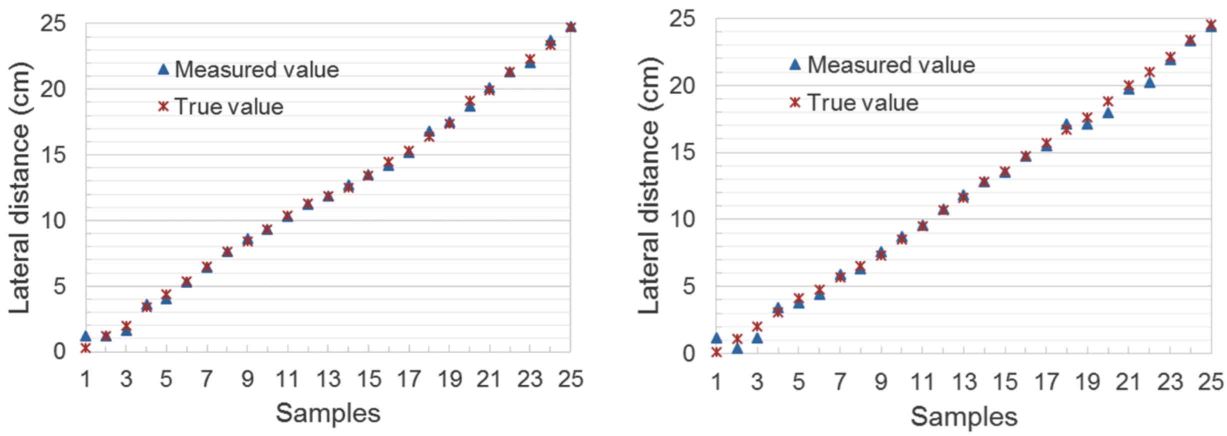

(a) (b)

Figure 4.8. Experimental comparison between measured and true values across the whole measurement range. (a) height = 12cm; (b) height =11.5cm.

Figure 4.9(a) shows the measurement accuracy of the alignment system when the lateral distance between two coils is 5cm, 10.5cm, and 15cm. The measurement was repeated 10 times for each lateral distance. The mean error is 0.2cm (STD=0) at the misalignment of 5cm, 0.25(STD=0.05) at 10.5 cm, and 0.12cm (STD=0.03) at 15cm. These data shows that the system has a high measurement repeatability.

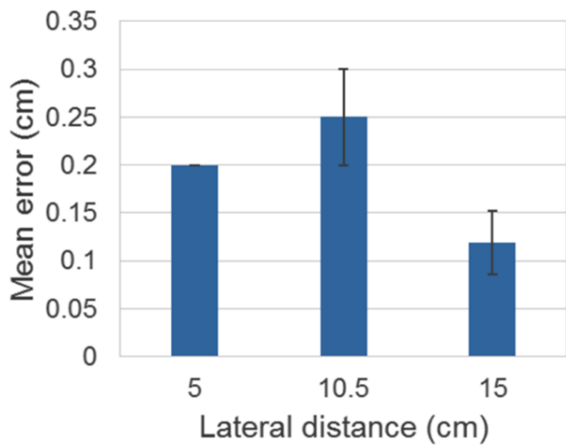

(a)

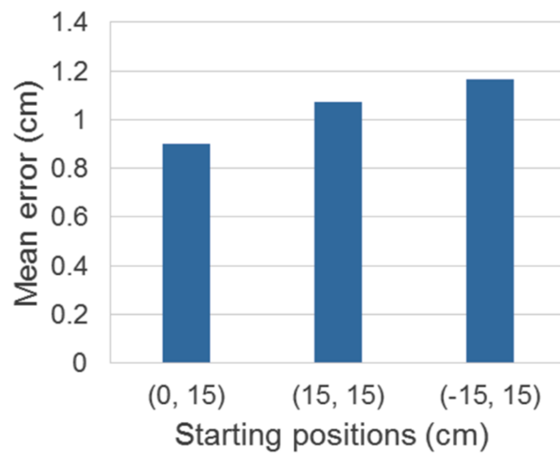

(b)

Figure 4.9. (a) Measurement accuracy at three lateral distances under a chassis height of 11.5 cm; (b) Measurement accuracy between two well aligned coils under a chassis height of 11.5 cm. The measurement was repeated 3 times for each starting position.

4.7.3 Minor adjustment with auxiliary coils

Figure 4.9(b) shows the positioning accuracy between the two well aligned charging coils with assistance from the four auxiliary coils. The experiment was repeated three times for each starting position. The mean error is 0.9cm when the starting point's coordinate is (0, 15), 1.1cm for (15, 15) and 1.2 cm for (-15, 15). Since the (0, 15) starting point is located on the Y axis, the error is slightly smaller than the other two conditions whose starting positions are in the first and second quadrants respectively. All three mean errors are lower than 1.2cm, which is within the acceptable range of misalignment in wireless EV charging.

4.8 CONCLUSION

A magnetic alignment system using existing charging electronics demonstrates that it can be a practical approach to address the misalignment issues in wireless EV charging. The distance between the two coils is transmitted to the user immediately for navigation purposes. The four auxiliary coils provide direction information and help the driver adjust the vehicle to ensure good alignment. The positioning error of the magnetic alignment system is within 1.2cm and allows for highly efficient wireless charging. The whole system is based on the existing wireless charging facility except for the four small auxiliary coils, thus, the overall cost of the system should be much smaller than an additional alignment system such as RF positioning.

CHAPTER 5

THREE DIMENSIONAL COIL POSITIONING [5]

[5] Gao, Yabiao, Chen Duan, Aleff Antonio Oliveira, Antonio Ginart, Kathleen Blair Farley, Zion Tsz Ho Tse. "Three-dimensional coil positioning based on magnetic sensing for wireless EV charging," Submitted to IEEE Transactions on Industrial Electronics, 04/06/2016.

5.1 ABSTRACT

Wireless power transfer (WPT) via magnetic resonance coupling is considered a promising outlet for electric vehicle (EV) charging due to the non-contact manner. Unlike a traditional transformer, with WPT the relative spacing between the primary and secondary coils is highly variable, which can affect the wireless power delivery and lower the efficiency. A magnetic positioning approach that shares the wireless charging structure is proposed to solve the misalignment issue associated with wireless EV charging. The proposed alignment sensing system employs multiple auxiliary minor coils on the secondary side to position the charging pad. The positioning principle and equivalent circuit were analyzed. The experimental results demonstrate that >92% of 108 samples have positioning error of <2cm, and 98% of the samples have positioning error of <3cm.

5.2 INTRODUCTION

Unlike railway/subway transit systems where grid energy is conductively transmitted to vehicle sides by pantograph sliding plates, road network complexity and EV flexibility cannot easily allow grid energy to power the EV in a contact manner. Thus, energy dense batteries are installed on EVs in order to achieve a decent travelling range on a single charge. The problem is that the energy density (kW/kg) of current EV batteries is about 0.8% that of gasoline [6]. This means either the total weight or cost of EVs would be too large to support a traveling range equal to traditional engine vehicles, which could make the adoption of EVs almost impossible on mass scale. To solve the battery issue, wireless EV charging through inductive power transfer (IPT) is presented and proved as a convenient charging method to refuel the EV by a concept named “opportunity charging” [7, 16]. Besides convenience, wireless charging could bring a few other benefits over plug-in charging, including increased safety, battery volume reduction, and weather proofing [6, 7, 16].

As described by SAE-J2954, a practical wireless charging system for EVs consists of power converter at the primary side, magnetic coupler (primary and secondary coils), rectifier and DC-DC converters on vehicle side, voltage/current sensors and charge control, alignment module, foreign object detection, and communications [55]. The current research concerns about wireless EV charging mainly include magnetic coupler design, circuit topologies, high frequency power conversion, and charge control strategies and algorithms [3, 7, 38, 42, 44, 48, 50, 61, 95, 102-106].

Although advanced power electronics and control approaches were presented to improve wireless charging's tolerance to misalignment, severe misalignment could still occur when a driver is parking his or her vehicle [71, 97]. The relative position between the primary and secondary coils can be highly variable depending on the driver's parking, which can cause efficiency drop or even lack of function if the misalignment is too large. Generally the wireless charging system can endure a maximum misalignment of 10cm while keeping a decent efficiency [97]. However, a previous study on drivers' parking behavior has shown that the mean longitudinal misalignment is more than 70cm when drivers do not receive any external parking navigation support [97]. The study also indicates that only 5% of drivers can park their vehicles within the accepted misalignment without any additional navigation tools. Overall, a vehicle alignment system which provides coil positioning information to guide the driver's parking for efficient charging is highly desirable.

The vehicle alignment technology for wireless EV charging is mainly focused on magnetic and radio positioning approaches [99, 107]. A radio positioning based alignment system uses multiple nodes underneath both the ground and vehicle and it operates at a higher frequency band than the wireless charging gate switching signals. For example, the system in reference [99] operates within 5.8GHz ISM band with a bandwidth of 125 MHz. The radio alignment tool is an independent system to the charging facility that adds an additional operating frequency and complex detection hardware, which could result in frequency interferences, system complexity, and high-cost problems. Magnetic alignment, however, can share most of the hardware and software platforms with the charging infrastructure and uses the primary coil to produce a magnetic field with the same frequency band of IPT switching frequency. The only additional hardware needed is the field detector.

This paper introduces a three-dimensional coil positioning technique employing the existing primary station together with four minor coils mounted on the receiver pad. The four minor coils work as magnetic sensors to pick up the magnetic field strength generated by the primary coil. The aim of this work is to determine the alignment by using the existing charging hardware while considering the air gap variations due to different car models or changes in weight carried by the vehicles. The measurement principle is, first, mapping the four sensors' output voltages in the navigation area, then, matching the measured data with previously mapped data space. Our previous study measures the misalignment through detecting the mutual inductance and resonance frequency changes with different misalignment cases [107]. Compared with the previous one that uses an additional ultrasonic sensor to measure the air gap, the current one removes the vertical measurement module by deriving the output voltage and mutual inductance over three dimensional coordinates.

5.3 WIRELESS CHARGING SYSTEM FOR EVS

Figure 5.1 illustrates the components of a typical wireless charging system used for EVs. The grid power is first rectified to DC, then a resonant inverter converts the DC power to high frequency AC current to drive the primary coil and produce a magnetic field. According to Faraday's law of electromagnetic induction, another AC current with the same frequency as the magnetic field is induced in the secondary coil. Additional power conversion is required to convert the high frequency circulating current into DC to charge a battery pack. The on-board electronics consist of rectifier, DC-DC converters, battery management system (BMS), as well as sensing modules. As the AC load is not purely resistive, a phase shift between the grid voltage and current will occur, which will lower the power delivery. Thus, a power factor correction (PFC) at the grid power input is used to decrease the apparent power and total current drawn from the grid. The driver interface displays all of the system’s electrical and mechanical parameters such as charging monitor, alignment information, and existence of metal and living things. These monitoring data can be transmitted to the primary controller via radios to enable, disable, and control the power delivery.

In a commercial wireless EV charger, Dedicated Short Range Communications (DSRC) is used as the wireless communication mechanism between the ground stations and the vehicle side due to its fast response characteristics, and will be applied widely in cars as required by the U.S. department of transportation and the SAE communications committee [108]. The EV can communicate with a wireless charging station as long as it enters the zone where the DSRC signal is available.

For wirelessly charging EVs, two parameters can influence the charging greatly: one is the existence of foreign objects over the primary station, the other is relative position between the primary and the secondary coils. Metal debris between the two charging pads could reach high temperatures and lower the WPT efficiency. Moreover, living things should not be subjected to the strong magnetic fields. Thus, a foreign object detection subsystem has been a necessary part of the system.

As stated above, an alignment system serving as a driving/parking guide can solve the misalignment issues by allowing the driver to easily park the vehicle perfectly. Considering system total cost and complexity, it would be desirable to have a subsystem that could position the coils by utilizing the existing wireless charging hardware. The proposed alignment system achieves this goal; it uses the charging hardware along with only four auxiliary coils attached on the secondary coil to measure the magnetic field and deduce the coil coordinates.

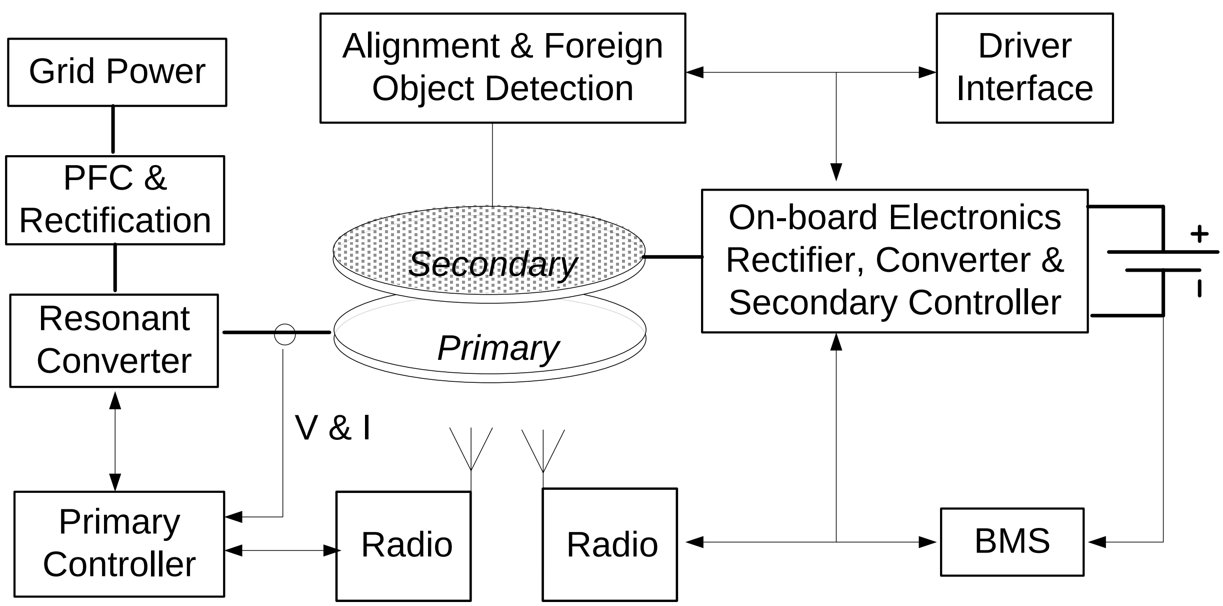

Figure 5.1. System structure for wireless EV charging

5.4 CONFIGURATION OF THE PROPOSED COIL POSITIONING SYSTEM

The coil positioning sensor consists of a high frequency power source, primary coil, controller, compensation capacitors, and multiple auxiliary coils attached on the secondary. As shown in Figure 5.2a, most of the positioning structures utilize the wireless charging hardware, including the high frequency source, processor, and the existing coil. Since the secondary coil position (x, y, z) has three unknowns in a three-dimensional coordinate system, at least three auxiliary coils are needed to identify the position. Assuming the primary and the auxiliary coil planes are parallel with each other in EV charging, the tilt and azimuthal orientation of the target are neglected. Four auxiliary coils are employed for identifying three variables and they are fixed on forward, backward, left and right directions of the secondary pad (Figure 5.2b). Although the position coordinate of the secondary can be obtained by three auxiliary coil inputs, the configuration of four auxiliary coils allows for a more accurate positioning by calculating the average value of four sets of position data and can increase the detection range around the primary for parking.

For the auxiliary coil design, a compensation capacitor is in parallel with the wire loops to create resonance and increase output significantly. The coil is fabricated on a PCB board by winding in a flat spiral loop.

The voltage at the auxiliary coil, which is consistent with the received power, is dependent on the coupling coefficient between the coupled coils. The coefficient is directly proportional to the mutual inductance between the coupled coils. For measurement purposes, voltage is generally used to represent sensor signals and seen as a medium for signal transmission and processing. Therefore, output voltages of the auxiliary coils are chosen as representatives of the positioning sensing.

In practical application, the vehicle position is deduced by acquiring and analyzing the four auxiliary coils' outputs. The operation of wireless EV charging can be split into two steps: the first is coil alignment to ensure efficient charging; the second is power delivery to start charging. The primary coil is designed to generate a weak magnetic field out of consideration for the safety of both living things and the charging hardware, which might be destroyed under large misalignment conditions if operated in high power. Switches are used to enable or disable the compensation capacitors and load to avoid the mutual interference from the other coils during the positioning. The switch on the secondary coil is disabled before starting charging. The switch on an active auxiliary coil is turned on for the secondary coil to read data while all others are off to keep other sensors inactive. The controller will transition to another minor coil as long as the previous voltage output is stored in its RAM. The current position will be updated on the display whenever the controller has a new data set of the four outputs.

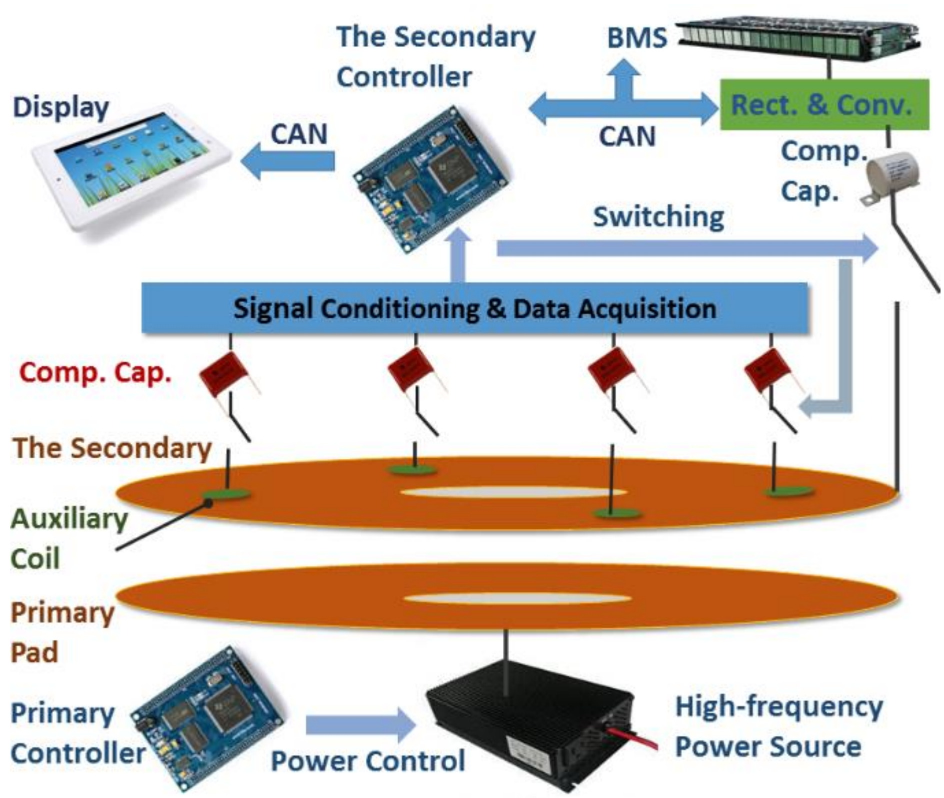

(a)

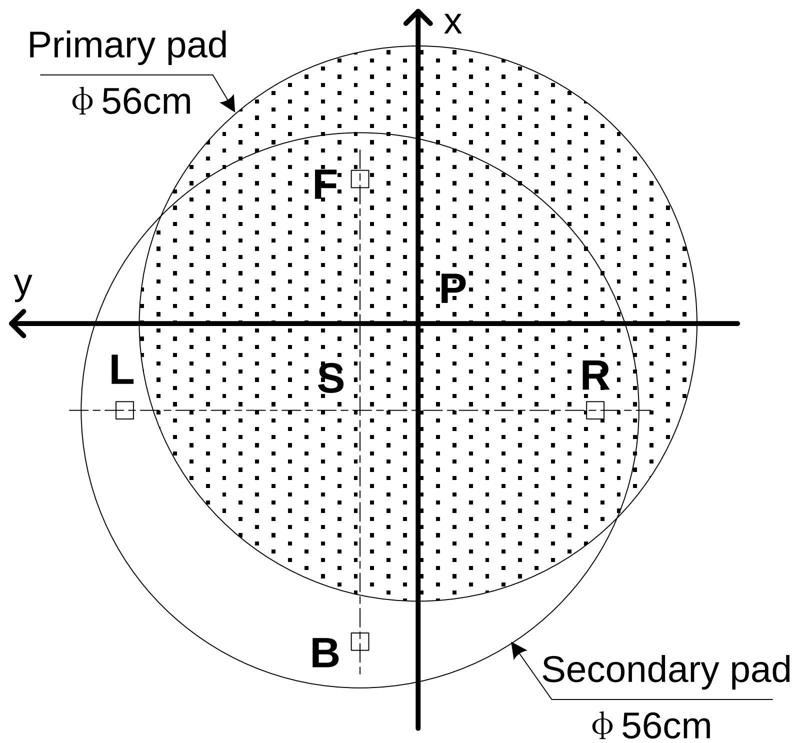

(b)

Figure 5.2. (a) Configuration of the three-dimensional coil positioning; (b) Vertical view of the position sensor using four auxiliary coils. P: primary center; S: secondary center; F: forward sensor #1; L: left sensor #2; R: right sensor #3; B: backward sensor #4.

5.5 PLACEMENT OF AUXILIARY COIL NODES

Theoretically, the position of the secondary coil can be calculated wherever the auxiliary coils are placed on the secondary. However, the field distribution needs to be considered for the auxiliary placement because the detection resolution can be variable for different coil placement. The location of the minor coils attached on the secondary should ensure that they have the maximum field measurement resolution when the primary and secondary coils are coaxial, which allows for the highest positioning accuracy. Figure 5.3a shows the 3-D model of the coil spatial structure. The field distribution is modeled and simulated by finite element method (FEM) to determine the maximum rate of field change for the auxiliary coil placement. The simulations show that the mutual inductance between the auxiliary and the primary is around 0.08μH, meaning that it can be disregarded for simplification and its effects on power transfer can be neglected. Table 5.1 displays the coil parameters and specifications used in the simulation. The circulating current is set at 0.3A in the primary coil and the air gap is set at 10cm in the simulation. Figure 5.3b shows the magnetic flux distribution produced by the primary side. The field slope is maximized when the distance from the primary center is 18-19cm which is seen as the best auxiliary location on the secondary. The area where the field has the maximum slope illustrates the auxiliary coils can detect the field at the highest resolution through the mutual coupling with the primary. The highest detection resolution at this area can decrease the positioning error for perfect alignment.

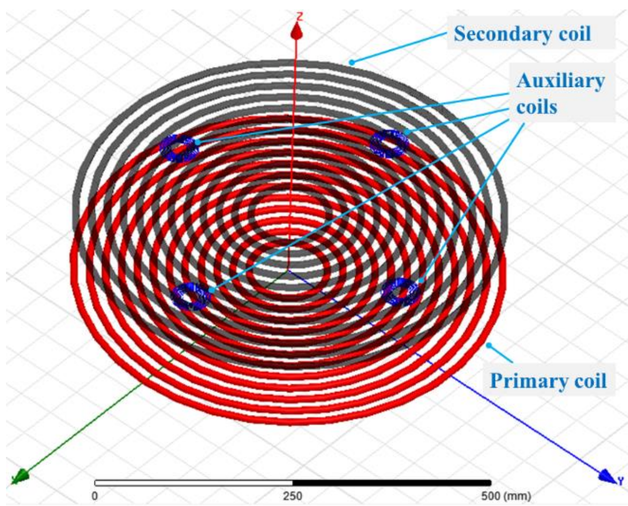

(a)

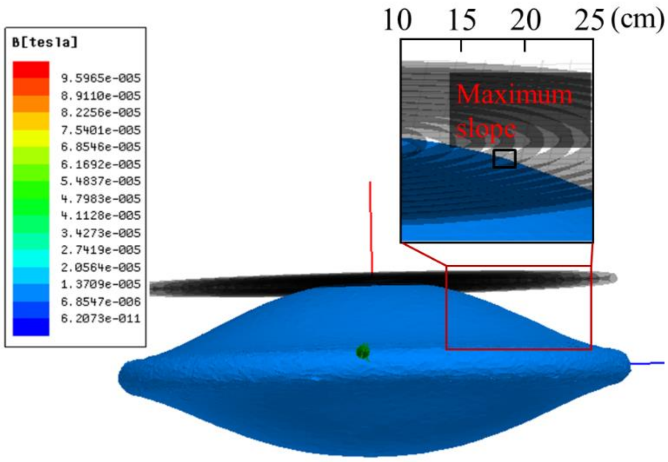

(b)

Figure 5.3. (a) Spatial distribution of the coil positioning system; (b) Magnetic flux distribution for determination of coil placement.

5.6 CONFIGURATION OF SIGNAL CONDITIONING CIRCUITRY

Figure 5.4a shows the configuration of signal sensing and conditioning. V_s is the power source to drive the coil. The load R_L is the input impedance of an operational amplifier, which is infinite. The operating angular frequency ω of the primary inverter is calculated by keeping the two coupled coils resonating simultaneously. The equation is

$$\omega = \frac{1}{\sqrt{L_p C_p}} = \frac{1}{\sqrt{L_a C_a}} \tag{5.1}$$

where C_p is the compensating capacitance at the primary side while C_a is the compensating capacitance at the auxiliary sides; L_p and L_a are self-inductance of the primary and auxiliary coils respectively.

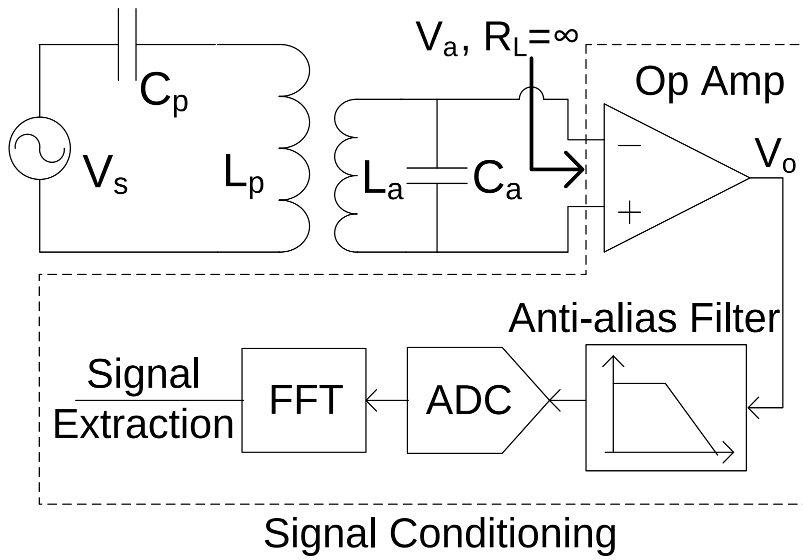

(a)

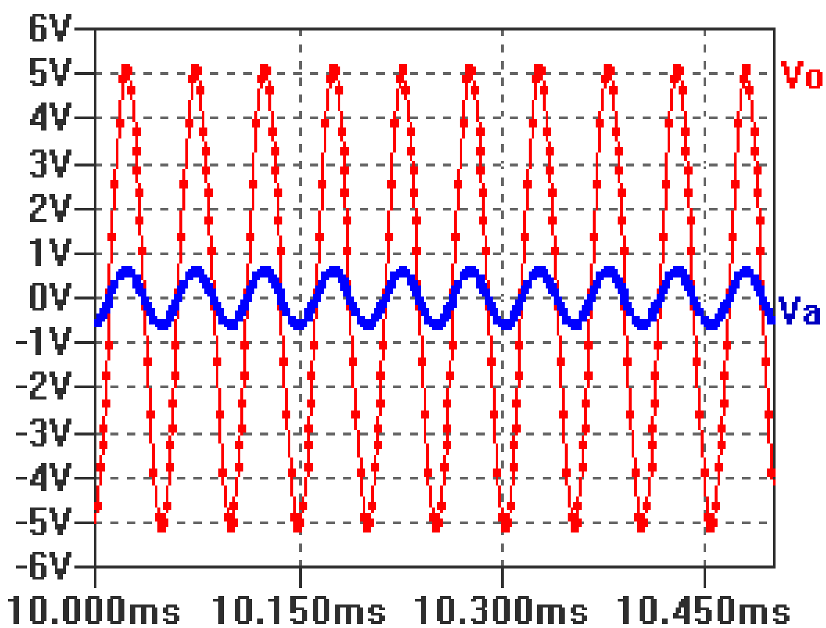

(b)

Figure 5.4. (a) Sensing circuit diagram; (b) LTspice simulation result about signal amplitude of an auxiliary coil. Simulation condition: V_s = 5.6V, Frequency = 19.8kHz, Mutual inductance is 0.05μH (assuming the coil gap is 10cm, the auxiliary coil is right over the ground coil), and the amplification factor is set at 8.4.

The primary inverter is programmed to input a low current to generate a weak magnetic field for the sensor coils to pick up the signal. A non-inverting op-amp is used to increase the amplitude of the signal, then the secondary controller converts the amplifier's analog output into digital signals for a fast Fourier transform (FFT), to extract the signal amplitude in the frequency domain. Table 5.1 shows the coil specifications including electrical characteristics and physical dimensions.

Table 5.1. Specifications of the primary and secondary coils and auxiliary sensor coils

Specification	Primary	Secondary	Auxiliary
Inductance (μH)	65.3	65.1	17.1
Resonant capacitance (μF)	1.0	1.0	3.7
Number of turns	12	12	10
Inside Diameter of coil (mm)	110	110	13
Outside Diameter of coil (mm)	560	560	51.5
Coil track width (mm)	9.5	9.5	1.0
Coil track separation (mm)	10.9	10.9	1.0

Figure 5.4b showcases LTspice simulation results about the sensor signal before and after the amplification. Since the auxiliary coils are ten times smaller in diameter than the primary coil and the mutual inductance is quite small when the two coils are relatively far away from each other, the output voltage of the auxiliary coils can be quite weak, thus, an amplifier is applied to increase their output level and detection range.

5.7 ANALYSIS OF EQUIVALENT CIRCUIT AND POSITIONING

The position of the secondary coil is estimated by measuring the auxiliary coil's voltage output. The auxiliary voltage output is determined by the mutual inductance or coupling coefficient between two coils. Here the mutual inductance is directly proportional to the coupling coefficient (Equation (5.2)). Neumann formula defines the mutual inductance between two coupled coils by their relative position, which in this case is variable, as well as physical dimension, which in this case is fixed. Moreover, the center coordinate of the secondary can be transformed to the auxiliary coordinates which correspond to the measured voltages. Thus, the section consists of modeling the output voltage, converting voltage to mutual inductance, deriving the mutual inductance from position, coordinate vector transformation from the secondary to the auxiliaries, and calibration and positioning estimation.

The use of switches across the coils and tuning capacitors allows the primary coil to resonate with only one of the four auxiliary coils at a time. Since the signal conditioning is isolated to the resonance part and is a linear amplification on the resonance output, the equivalent circuit is simply modeled as Figure 5.4a where L_m is the mutual inductance between the two coupled coils. The coupling coefficient is defined by

$$k = L_m \Big/ \sqrt{L_p L_a} \tag{5.2}$$

The input impedance of the equivalent circuit in Figure 5.4a:

$$Z(\omega) = (j\omega C_p)^{-1} + j\omega L_p + j\omega L_m \,//\left[j\omega L_a + (j\omega C_a)^{-1} \right] \tag{5.3}$$

The voltage gain is

$$G = \left| \frac{V_a}{V_s} \right| = \left| \frac{(j\omega C_a)^{-1}}{Z(\omega)} \right| \tag{5.4}$$

Substituting (5.2) and (5.3) into (5.4), it is

$$G = \left| \frac{\omega^2 C_p L_m}{\omega^4 L_p L_a C_p C_a (1-k^2) - \omega^2 (L_p C_p + L_a C_a) + 1} \right| \tag{5.5}$$

As discussed above, V_a is linearly amplified by the conditioning circuitry, the output of signal throughout the whole sensing circuit V_o is

$$|V_o| = \left| \frac{K_{amp} V_s \omega^2 C_p L_m}{\omega^4 L_p L_a C_p C_a (1-k^2) - \omega^2 (L_p C_p + L_a C_a) + 1} \right| \tag{5.6}$$

In which K_{amp} is the amplification factor of its signal conditioning circuitry.

The output V_o is read by the secondary controller and extracted in terms of amplitude and frequency.

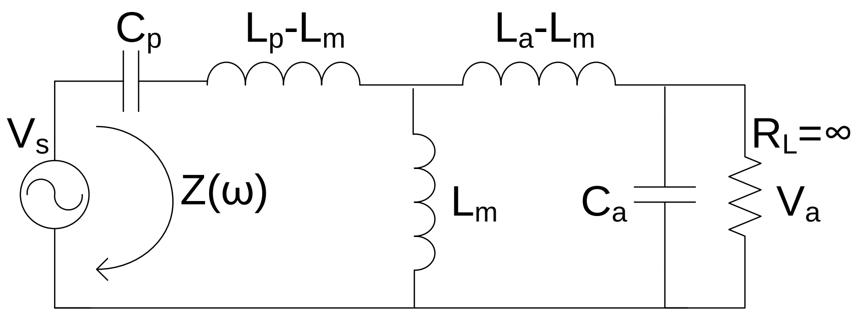

(a)

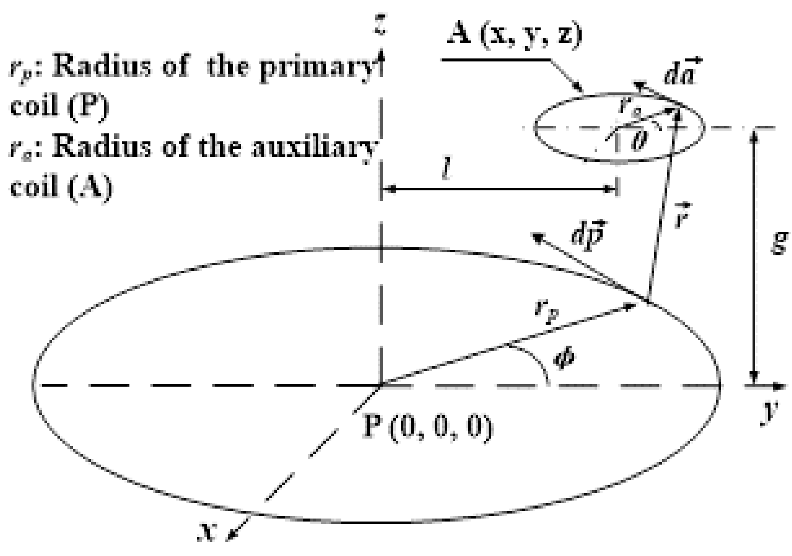

(b)

Figure 5.5. (a) Equivalent circuit of the auxiliary coil sensing; (b) The primary and an auxiliary coil in a three-axis coordinate system.

Figure 5.5b shows the spatial configuration of each set of wire loops in a 3D coordinate system for mutual inductance calculation. Neumann formula is used to express the mutual inductance between two wire loops:

$$M = \frac{\mu_0}{4\pi} \oint_p \oint_a \frac{d\vec{p} \cdot d\vec{a}}{r} \tag{5.7}$$

where μ_0 is the space permeability, $d\vec{p}$ and $d\vec{a}$ are the small line parameter for integration, and r is the distance between $d\vec{p}$ and $d\vec{a}$,

In Figure 5.5b, φ is the corresponding angle of integration variable of the primary while θ is the angle of the secondary, the coordinate of primary coil center is (0, 0, 0), and the sensor coil center is (x, y, z). Thus

$$r = \sqrt{{r_p}^2 + {r_a}^2 + g^2 + l^2 - 2r_p r_a \cos(\phi - \theta) - 2r_p l \cos\phi + 2r_a l \cos\theta} \tag{5.8}$$

$$d\vec{p} \cdot d\vec{a} = r_p r_a \cos(\phi - \theta) d\phi d\theta \tag{5.9}$$

$$l = \sqrt{x^2 + y^2} \text{ , and } g = z \tag{5.10}$$

Combining (5.7), (5.8) and (5.9) into (5.10):

$$M = \frac{\mu_0}{4\pi} \int_0^{2\pi} \int_0^{2\pi} \frac{r_p r_a \cos(\phi - \theta) d\phi d\theta}{\sqrt{{r_p}^2 + {r_a}^2 + x^2 + y^2 + z^2 - 2r_p r_a \cos(\phi - \theta) - 2\sqrt{x^2 + y^2}\left(r_p \cos\phi - r_a \cos\theta\right)}} \tag{5.11}$$

Equation (5.11) shows the mutual inductance between two wire loops. As both of the two coupled planar coils have multiple turns of wire loops, the mutual inductance between them is the sum of all possible combinations of single wire loops. Hence, the total mutual inductance is

$$L_m = \sum_{i=1}^{n_p} \sum_{j=1}^{n_a} M_{ij} \tag{5.12}$$

where M_{ij} is the mutual inductance between wire loop i of the primary and j of the auxiliary coil. Equations (5.11) and (5.12) indicate that the mutual inductance L_m is a function of the sensor position $A_n(x_n, y_n, z_n)$ in which n is the number of sensor nodes, thus, the relation can be described as $L_m = h(x_n, y_n, z_n)$. Given that all the electrical characteristics in equation (5.6) are fixed in the sensing circuit except the mutual inductance depending on the relative position between the coupled coils, V_o is a function of position, assumed as

$$V_O = f(L_m) = f[h(x_n, y_n, z_n)] = F(x_n, y_n, z_n) \tag{5.13}$$

In this paper, 4 sensor nodes are supposed, so n=4. Assuming the secondary coordinate $S(x_s, y_s, z_s)$, according to Figure 5.2b, the relation between $A_n(x_n, y_n, z_n)$ and $S(x_s, y_s, z_s)$ can be expressed by the following matrix operation:

$$\begin{bmatrix} x_1 & y_1 & z_1 \\ x_2 & y_2 & z_2 \\ x_3 & y_3 & z_3 \\ x_4 & y_4 & z_4 \end{bmatrix} = \begin{bmatrix} 1 & d & 0 \\ 1 & 0 & d \\ 1 & 0 & -d \\ 1 & -d & 0 \end{bmatrix} \bullet \begin{bmatrix} x_s & y_s & z_s \\ 1 & 0 & 0 \\ 0 & 1 & 0 \end{bmatrix} \tag{5.14}$$

in which d is the distance from the center of secondary pad to the auxiliary nodes and z_s equals the gap g.

Substituting (5.14) into (5.13):

$$\begin{cases} V_{o1} = F\left((x_s + d), y_s, z_s\right); \\ V_{o2} = F\left(x_s, (y_s + d), z_s\right); \\ V_{o3} = F\left(x_s, (y_s - d), z_s\right); \\ V_{o4} = F\left((x_s - d), y_s, z_s\right). \end{cases} \tag{5.15}$$

According to equations (5.11-5.15), although the output voltage corresponds to the secondary position, which can form 4 equations for three unknowns, the position coordinate (x_s, y_s, z_s) cannot be mathematically expressed due to the calculating of dual integrals. However, a database matching technique is established to derive the coordinate of the secondary and solve this issue.

As discussed in the above equations (5.13)-(5.15), there is a one to one correspondence between the voltage vector $\vec{V}(V_{o1}, V_{o2}, V_{o3}, V_{o4})$, which is acquired by the secondary controller, and the secondary coordinates (x_s, y_s, z_s), in three-dimensional space. Hence, the three variables can be derived by matching the measured voltage $\overrightarrow{V_m}$ with the built-in voltage array $\vec{V}$ until $\left\|\vec{V} - \overrightarrow{V_m}\right\|$ is minimized. The matching process is realized by a for-loop (known as an exhaustive search) to determine the desired position one by one throughout the lookup table. The positioning flowchart is shown in Figure 5.6.

Although the database can be numerically obtained through equations (5.13)-(5.15), experimentally measuring the voltage outputs at positions within an alignment region can increase accuracy by avoiding the possible negative influence of metal objects such as vehicle chassis. A large metal chassis can re-shape the field distribution dynamically while aligning the coils. Another advantage is that the systematic error resulting from sensor placements and sensing circuits can be diminished because it bypasses the process or electrical elements.

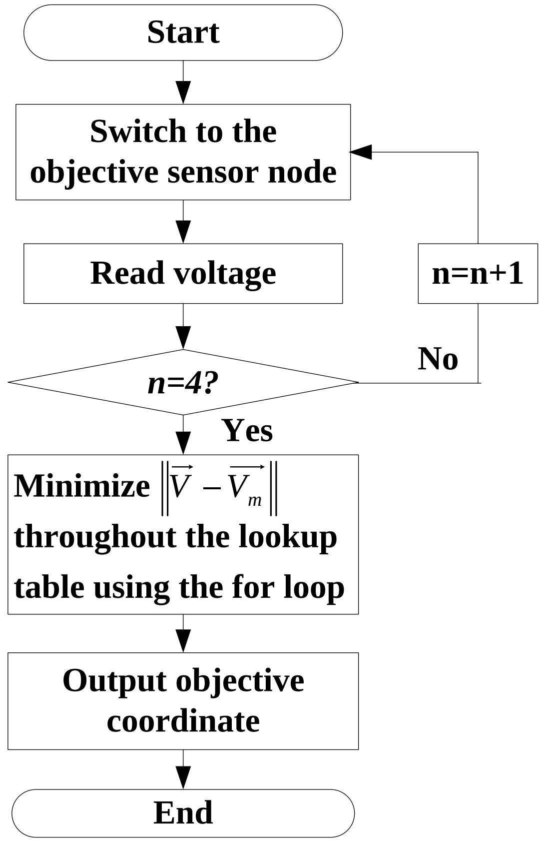

Figure 5.6. Flowchart of the 3D positioning

5.8 TESTING PLATFORM

Figure 5.7 shows the experimental platform where a three-axis motorized platform modified from a CNC machine (DHC, PlasmaCAM, Inc., Colorado City, CO, USA) built to test the alignment estimation approach. The secondary pad with auxiliaries is mounted on the platform while the primary is placed on ground. The traveling path of the coil can be programmed on the machine computer or manually operated by the control panel in Figure 5.7. The test platform can move horizontally in a 1.2m× 1.2m plane and vertically in a 0.6m range. The maximum allowed speed is 25m/min for the horizontal and 2m/min for the vertical direction. The dimensions of the platform are: 1.75m width, 1.65m height, and 1.65m depth.

The inverter in Figure 5.7 is used to drive the primary to produce a magnetic field for the auxiliaries to pick up. The inverter DC input is set at 5V to operate under low power during alignment process and generate a weak magnetic field of <15μT throughout the charging zone for EM safety consideration of living things. An NI CompactRIO-9074 is applied to acquire the sensing signals. The positioning search algorithm is run in MATLAB by using LabVIEW Mathscript. A LabVIEW program was developed to analyze, extract, display, and record the signals and position. During experiments, the position and related voltages will be stored into an excel file whenever the LabVIEW receives inputs and operation orders from users. 108 position samples from air gaps of 9cm to 14cm were measured in the experiment. The samples were distributed on range of 0-70cm and both 0 and 10cm misalignment in the horizontal plane.

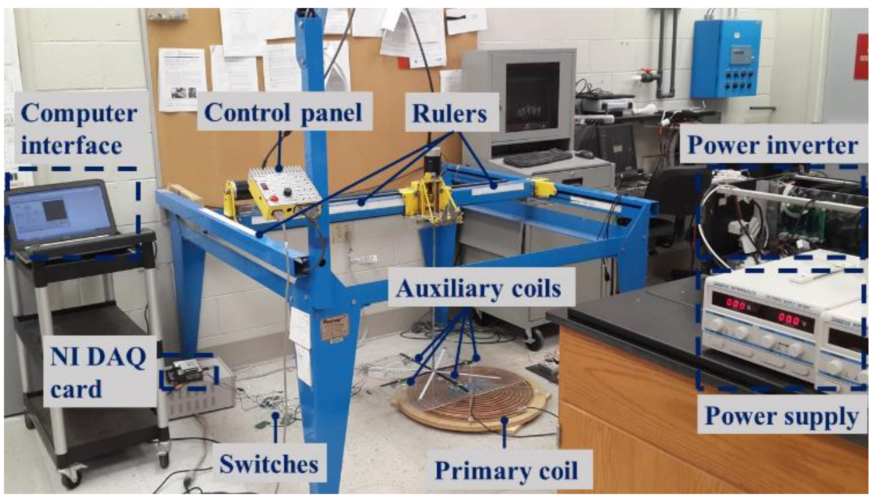

Figure 5.7. Experimental platform for coil positioning.

5.9 RESULTS AND DISCUSSION

5.9.1 Sensor testing

The high accuracy and repeatability of sensing elements play major roles in the overall successful measurement. Figure 5.8 is the sensor output in both time and frequency domains from NI LabVIEW under a 10cm air gap when the sensor coil was coaxial with the primary axis. The signal spectrum shows that the output consists of a single frequency that is 19.8 kHz, showing that possible noise in other frequencies are filtered and the sensor output is low in noise.

The signal amplitude is close to the simulation result which is around 5.2V as shown in Figure 3b.

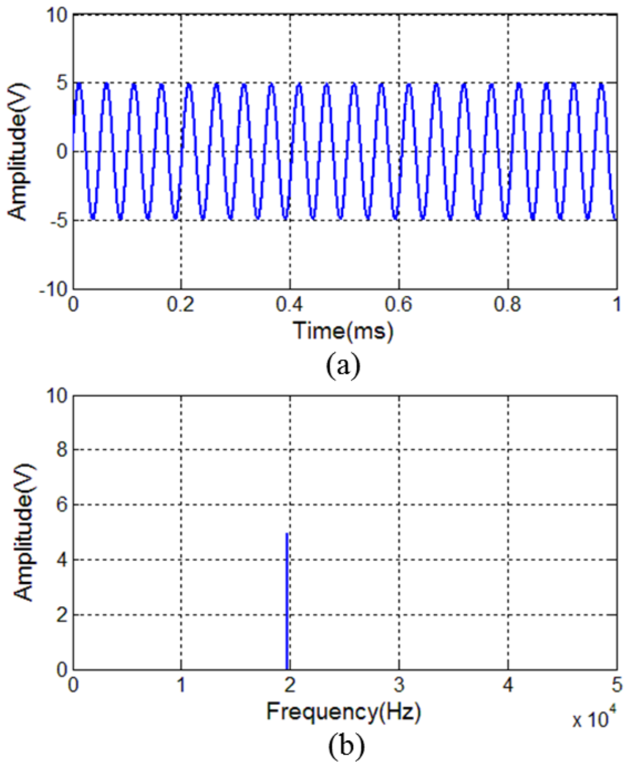

Figure 5.8. Sensor output in (a) time domain and (b) frequency domain.

The sensor nodes were also tested throughout the whole measurement range of 99cm, with a 1cm increment. Figure 5.9 shows the output voltage curves for 3 trials, which are highly coincided. The maximum relative repeatability error is <4.1% for all the 100 positions, indicating the sensor has high repeatability. The relative repeatability error is defined as the difference between the maximum and minimal voltages divided by the mean value of the three trials under the same conditions. Repeatable sensor output is essential in a measurement system.

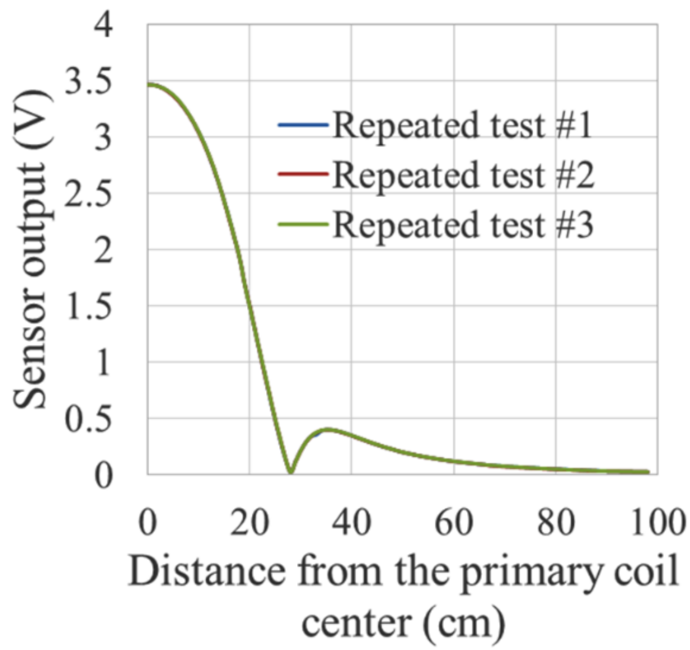

Figure 5.9. Sensor output repeatability under air gap of 10cm.

According to Figure 5.9, the derivative of the curves reaches the maximum value 0.235V/cm when the distance from the primary coil center is 19cm. The maximum slope allows the auxiliary coils to have the highest detection resolution when the distance from the primary center is 19cm. In this paper, the placement of the auxiliary follows the maximum slope theory to let the system have highest sensitivity when the two coils are close to perfect alignment. The same conclusion can be drawn from Figure 5.10.

Figure 5.10 shows the testing curves under air gaps of 9-14cm. According to Figure 5.10, the sensor output voltage becomes larger around the coil center along with a decrease of the air gap. The sensor output drops to zero when the distance from the center is around 28cm which is right over the primary coil edge. Since the field direction is reversed inside and outside the coil edge, the overall magnetic flux going through the surface of sensor can be zero around the edge and thus the output voltage can be zero.

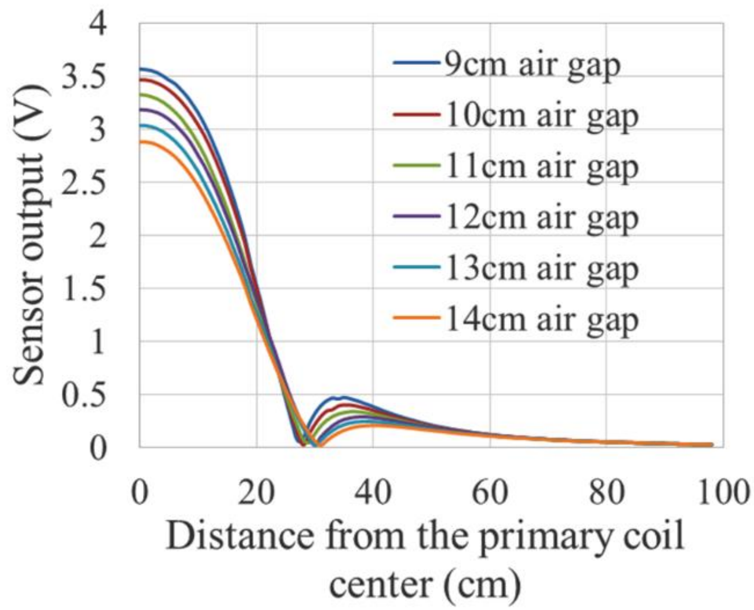

Figure 5.10. Sensor output at multiple air gaps ranging from 9-14cm.

5.9.2 Magnetic alignment evaluation

Figure 5.11 shows the comparison of actual and measured coordinates under different gaps. 108 position samples were tested to validate the accuracy of the alignment system. These samples are taken from multiple air gap and alignment conditions. The error in Figure 5.11 ranges from 0.2cm to 4.3cm throughout the 108 samples. The curves in Figure 5.10 are almost overlapped when the sensor distance is >50cm where all four nodes have close responses, which will influence the detection range. Hence the maximum detection range is set at 70cm in Figure 5.11.

The measurement error is less than 1cm across Figure 5.11 (a) to (f) when x is approaching to 0, indicating the system has higher alignment accuracy when both coils are well aligned. This is because the magnetic fields are stronger, which generates a higher sensor output when they are close to the center of the primary coil. A larger sensor output can increase the resolution over distance, leading to a more accurate alignment evaluation at the zero misalignment condition. Figure 5.11 also indicates that the proposed positioning method can meet the alignment detection requirement for efficient wireless charging, considering the maximum allowed misalignment is 10cm as stated above.

According to Figure 5.12, 62% of the 108 samples have a measurement error of less than 1cm, 30.5% have an error of between 1cm and 2cm, 5.6% are from 2cm to 3cm, and 1.9% are from 3cm to 4cm, showing that over 98% of the sample errors are not more than 3cm for a misalignment range up to 70cm and gap variation from 9cm to 14cm.

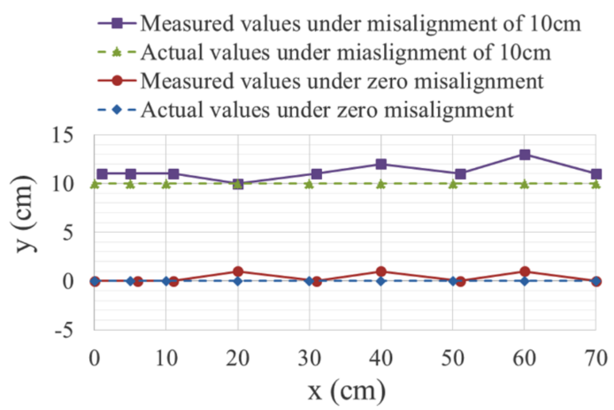

(a)

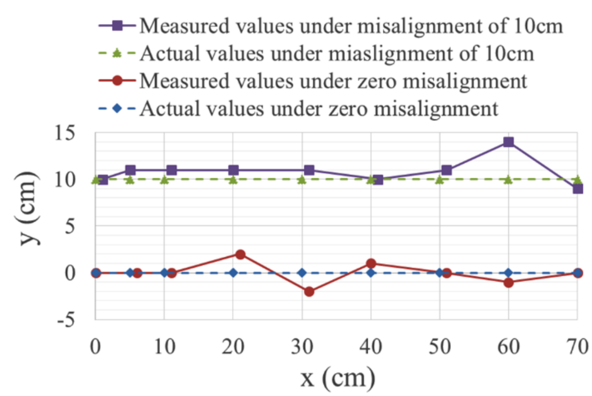

(b)

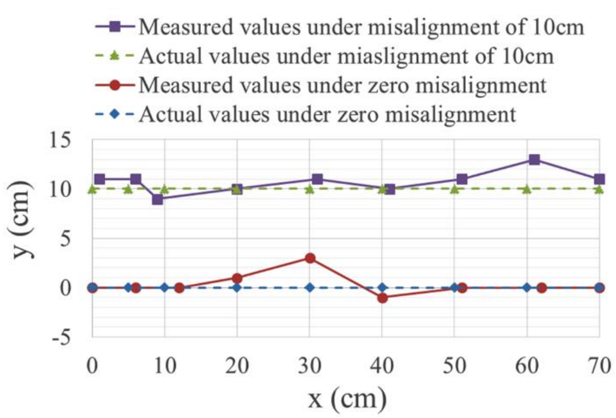

(c)

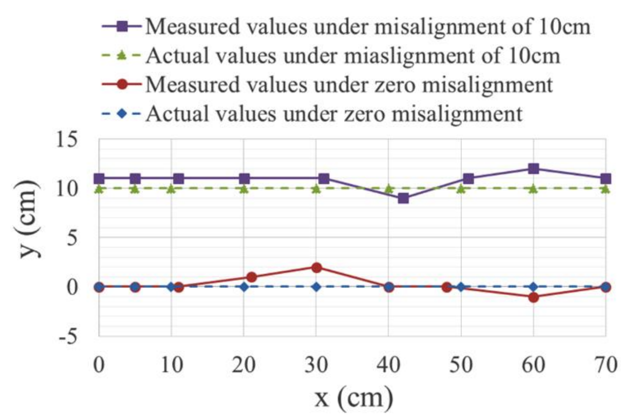

(d)

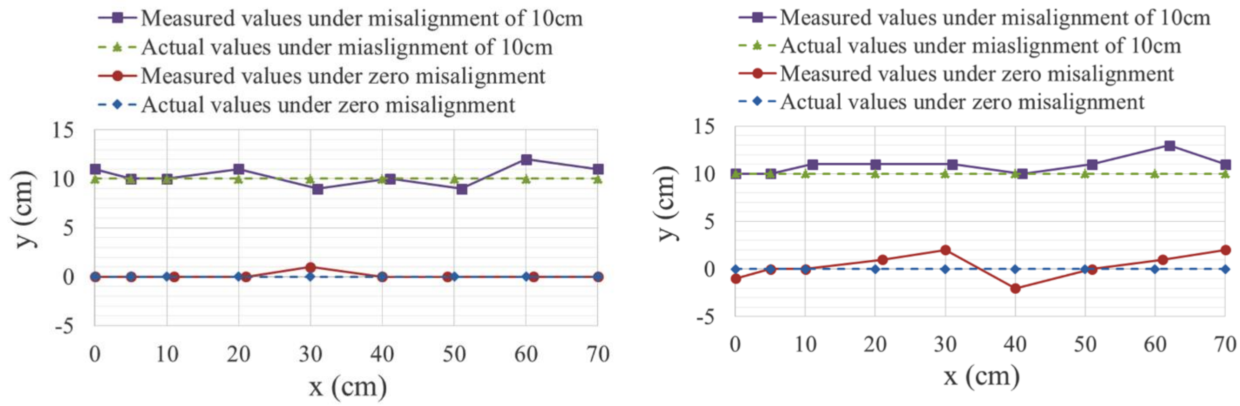

(e) (f)

Figure 5.11. Comparison of measured and actual coordinates for 54 sample positions under two different misalignment values and three air gaps. (a) air gap = 9 cm; (b) air gap = 10 cm; (c) air gap = 11cm; (d) air gap =12cm; (e) air gap = 13cm; (f) air gap =14cm.

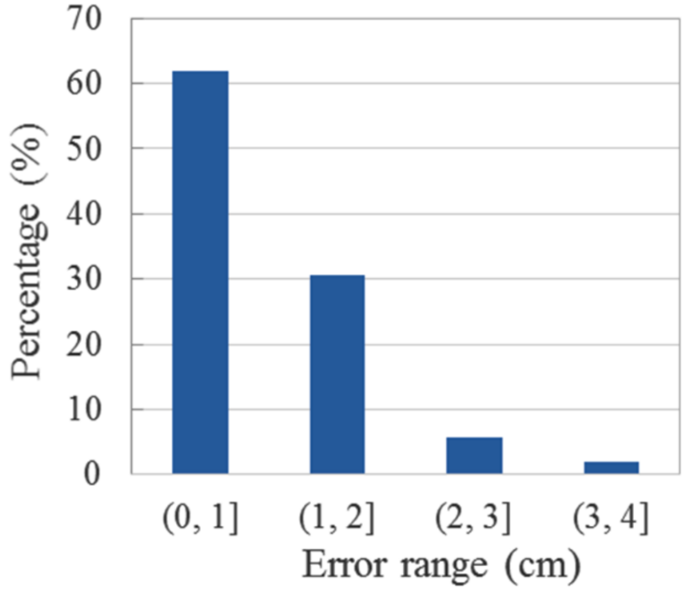

Figure 5.12. Probability of error distribution

5.9.3 AIR GAP MEASUREMENT

Figure 5.13 shows the comparison results between measured and actual air gaps under zero and 10cm misalignment conditions. The measured air gap is the average gap of 9 samples along x axis. As shown in Figure 13a, the measured air gap is 9.6 (SD=0.87), 10.5 (SD=0.88)

11.4(SD=0.88), 12.5(SD=0.72), 13.4(SD=0.52), 14(SD=0) when the misalignment is zero and the actual air gap is 9, 10, 11, 12, 13, and 14cm separately. When the misalignment was set at 10cm to repeat the measurement, the measured air gap is 9.1(SD=0.33), 10.1(SD=0.33), 11(SD=0.70), 11.9(SD=0.60), 13.2(SD=0.44), and 13.9(SD=0.33) (Figure 13b). All the measurement errors of the above configurations are within 0.6cm. As the data was acquired with an incremental step of 1cm during the calibration, the maximum measurement error of 0.6cm is reasonable.

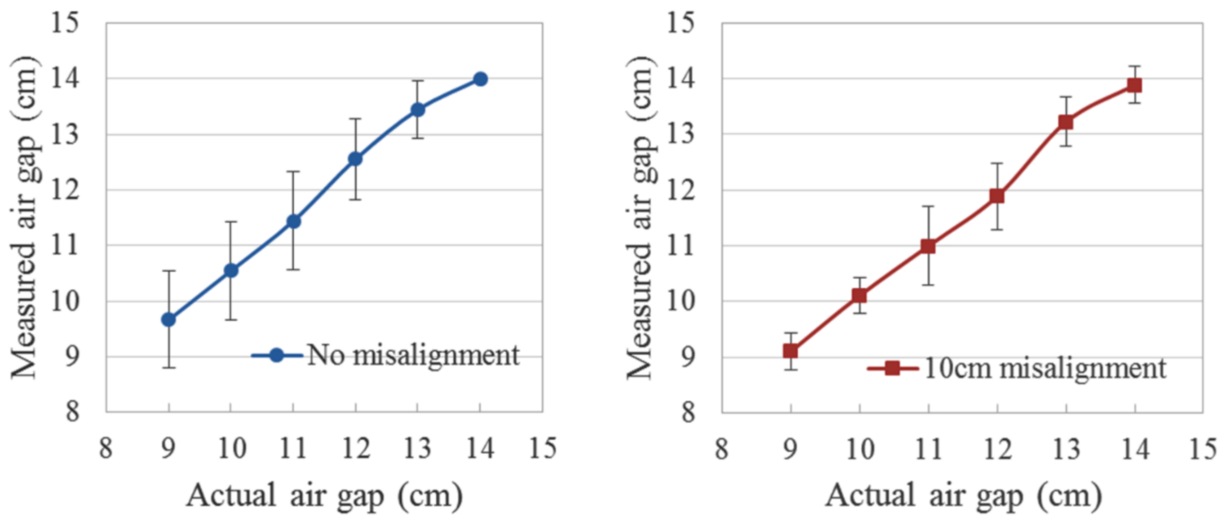

Figure 5.13. Comparison between measured and true air gaps (a) no misalignment; (b) misalignment = 10cm

5.10 CONCLUSION

This paper introduces a 3D coil positioning technique for wireless EV charging by using multiple auxiliary coils as field sensors along with existing charging hardware. The circuit model is simulated by LTspice to determine the electronic parameters of resonant elements and the non-inverting amplifier. The relation between mutual inductance and coil coordinates is derived based on Neumann's equations to allow the voltage output to be related to position. The field sensor was tested before the positioning experiment and shows high output repeatability and reliability. The alignment system has a detection range of up to 70cm. 92.5% of the tested samples have an error of less than 2cm and 98% have an error of less than 3cm. The air gap estimation also shows high accuracy, with maximum error of 0.6cm and mean error of 0.25cm. The proposed 3D positioning system is a highly valuable approach to aligning coils for efficient wireless EV charging.

CHAPTER 6

SAFETY CONCERNS [6]

[6] Gao, Yabiao, Kathleen Blair Farley, Antonio Ginart and Zion Tsz Ho Tse. "Safety and Efficiency of Electric Vehicle Wireless Charging," Accepted by Proceedings of the IMechE, Part D: Journal of Automobile Engineering.

6.1 ABSTRACT

Wireless power transfer (WPT) is a promising method to address concerns over Electric Vehicle (EV) charging. Since wireless charging stations operate without large cables or above-ground stations, they can be conveniently installed in public locations without the risk of vandalism or weather-inflicted damage, improving the life span of the EV charging station. In order for wireless charging stations to become widespread, possible health considerations regarding exposure to strong electromagnetic fields present during WPT must be investigated. This body of work examines (1) potential human safety hazards, (2) electronic device interference, and (3) thermal heating effects of wireless charging systems. A 3.3kW WPT prototype was built in order to examine these effects. Changes in WPT efficiency due to coil misalignment were also investigated using an automated 3-axis platform. Design considerations for EV wireless charging systems and safety recommendations are presented.

6.2 INTRODUCTION

Although the basic concept of wireless power transmission was introduced by Faraday and Tesla in the 19th century, the engineering research drew little attention due to the limitations of solid-state power electronic devices at that time [7, 66]. WPT technology has been an emerging research topic for a few years, and potential applications for WPT have been found in many fields including mobile devices, intelligent household facilities, medical devices, and transportation electrification [29, 35, 60, 63, 81, 109]. Figure 6.1 is a schematic diagram of a WPT system. A high-frequency power converter drives the transmitter coil (also called the "primary side") to generate an alternating magnetic field. This alternating magnetic field induces an alternating current in the receiver coil (also called the "secondary side"). The receiver electronics converts the alternating current into usable power to drive the desired load.

Capacitors are used to tune and match frequencies and impedances of the transmitter and receiver coils for optimal magnetic resonance coupling, allowing power to transfer wirelessly while maintaining a large air gap [110, 111].

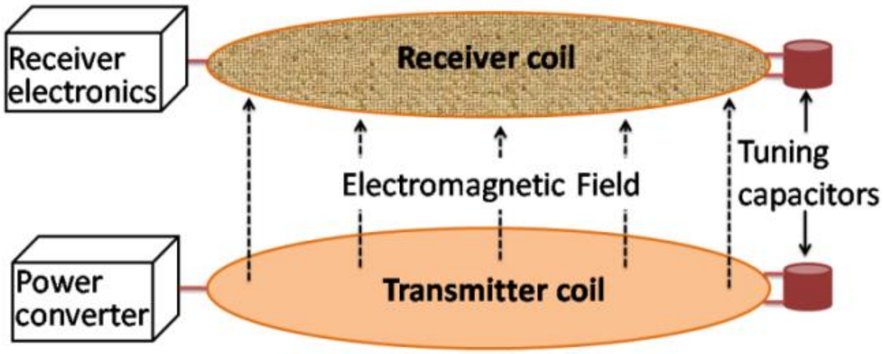

Figure 6.1. Schematic diagram of a wireless power transfer system

Driven by environmental awareness and the price of fossil fuel, electric vehicle (EV) use is growing, and EVs are becoming increasingly available for consumers and businesses alike [16, 112, 113]. In 2011, the U.S. government set the goal that one million EVs will roam U.S. streets by the year 2015 [114]. However, the major obstacle for wide-spread use of EVs is the battery, which cannot support a long travelling range in comparison to gasoline vehicles [56, 115]. In addition, conventional plug-in charging stations require street equipment that is vulnerable to vandalism and weather damage [56, 71]. Wireless charging (WC) has the potential to solve the battery life problem for future EVs by increasing opportunities to charge EVs. WC could also enhance the user experience, as it is contactless charging [7, 115]. Currently, a number of research institutes and universities are developing EVWC technologies, including ORNL, University of Michigan at Dearborn, KAIST, Delft University of Technology, University of Auckland, New York University, Virginia Tech, Georgia Tech, and others [7, 35, 38, 40, 41, 43, 47, 51, 70, 102, 116]. Wireless chargers for EVs are being commercialized, and several companies are working in this area, including Qualcomm Halo, Witricity, Evatran, WAVE, IPT technology, and more.

Because strong alternating magnetic fields are generated between the transmitter and receiver, as well as in the charging system's surrounding area, human exposure to EM field have become important concern that should be seriously considered before WC’s public acceptance [83, 117]. To the authors' knowledge, very few publications discuss WC safety [117, 118]. It is necessary to investigate the potential influence of WC on the human body, electronic devices and the environment. The measuring techniques of magnetic fields for human safety is proposed by the Australian Radiation Protection and Nuclear Safety Agency (ARPANSA), which is based on ICNIRP standards. The ARPANSA measurement techniques suggest that maximum human magnetic field exposure must not exceed 27.3μT, and the average magnetic field strength of four human body parts (head, chest, groin, and knees) must be lower than 6.25μT [119, 120]. In this paper, a 3.3kW EVWC prototype was developed to investigate the safety issues associated with EVWC systems and quantify eddy currents, thermal effects and Electromagnetic Interference (EMI) on surrounding objects with a variety of conductive surface areas and topologies. The authors also give safety recommendations for the use of EVWC systems.

While WC is a promising technology for EV applications, coil misalignment is a common phenomenon when parking a vehicle over the WC equipment, which can lower the power transfer efficiency [42, 71]. An automated 3-axis platform was built to investigate the effects of misalignment on efficiency and power transfer capabilities under diverse configurations of misalignment and air gap.

6.3 METHODS AND MATERIALS

6.3.1 WPT Principles

A full-bridge SP wireless charger schematic is shown in Figure 6.2(a). The four semi-conductors were driven by square waveform signals with a duty cycle close to but less than 50% to avoid make-before-break situations (momentary short circuit) in the inverter. A rectifier was used at the secondary side in parallel with a filter capacitor to regulate the output voltage. Although the energy consumption of the rectifier can lower the system efficiency due to the voltage drop, its simplicity and no requirement for control electronics make it an ideal choice for an industrial use where reliability and low-cost are highly valued.

Figure 6.2(b) is a simplified SP circuit diagram, and Figure 6.2(c) is the corresponding equivalent circuit. $Q_2 = R_L/(\omega L_2)$ is the loaded quality factor for the receiver coil with a load of R_L. Although a higher Q-factor increases the power transferred from the receiver, it can cause the system to be too sensitive to be well-tuned [121]. $Z(\omega)$ in equation (6.1) is the circuit impedance.

$$Z(\omega) = \frac{1}{j\omega C_p} + j\omega L_{pl} + j\omega L_m // \left(j\omega L_{sl} + \frac{1}{j\omega C_s} // R_L \right) \tag{6.1}$$

Where ω is the switching frequency, C_{p} is the series tuning capacitance of the primary, and C_{s} is the tuning capacitance of the secondary. C_{p} must equal C_{s} to achieve resonance. L_{p1} and L_{s1} are the leakage inductance of each coil. Since both coils are the same, L_{p1} equals L_{s1}. L_{m} is the mutual inductance. The leakage and mutual inductance can be experimentally measured. The battery is equivalent to a resistive load, R_{L}, which can be calculated using the delivered power and voltage across the battery[61]. S in equation (6.2) is complex power.

$$S = P + jQ = V_1 \left(\frac{V_1}{Z(\omega)} \right)^* \tag{6.2}$$

here, P is the active power and Q is the reactive power. V_1 is the input high-frequency voltage in the primary. Resonance occurs when the reactive power is zero, which corresponds to the maximum efficiency. Combining equations (6.1) and (6.2), the resonant frequency can be calculated. When misalignment or gapping happens, causing a shift in mutual and leakage inductance, the switching frequency is adjusted to regulate the output power as well as maintain maximum efficiency.

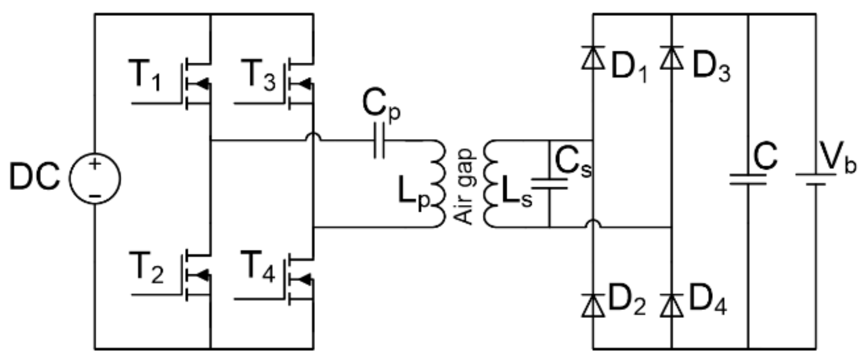

(a)

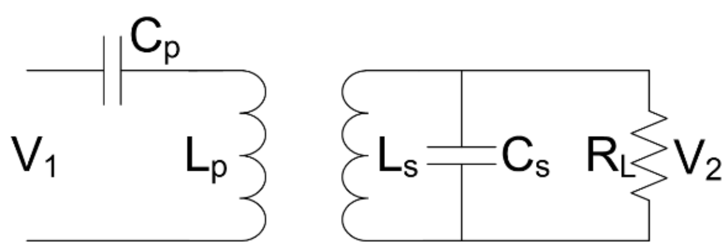

(b)

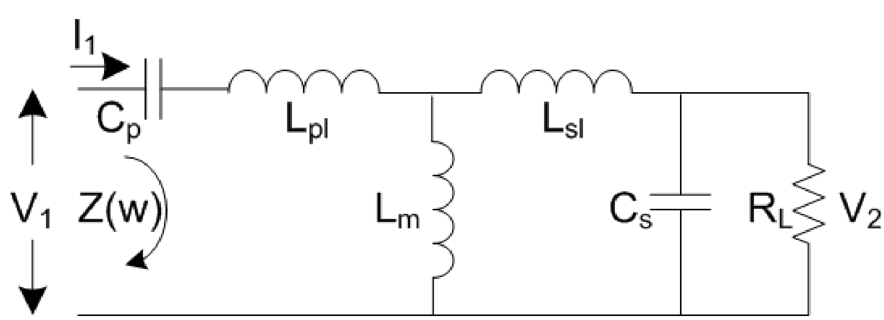

(c)

Figure 6.2. Circuit diagram of proposed WPT system: (a) SP topology; (b) simplified SP topology; (c) Equivalent circuit of SP topology

6.3.2 Coil Structures for EVWC

In order to contain the magnetic field flux within its cylindrical area, a ferrite structure is necessary to shape the magnetic field and constrain the leakage flux outside of the pad. With this structure, the magnetic field drops rapidly outside the pad [122].

Three types of coil structures and shapes are presented in the literature, including circular, flux-pipe, and bipolar topologies. The circular coil structure is commonly used with an efficiency as high as 90% [63]. Although the circular topology needs a bigger coil diameter than the other two methods to achieve the same power transfer capabilities, its characteristics of simplicity and low cost make it a preferred option for our experimental setup. For the flux-pipe topology, the coil is wound along an H-shaped ferrite bar. This coil structure has a double-sided magnetic flux path, so it is also called a double-sided winding transformer. The flux on the pad's back is the same as the front side, meaning that the magnetic loss in the shielding plate is significant [66]. The bipolar topology employs D or Q coils to couple the power; a detailed description is given in [67]. The bipolar pad has less flux going through the pad's back and a higher efficiency than a circular pad [66].

6.3.3 Hardware Setup

A 3.3kW EVWC prototype was designed and implemented in a Nissan Leaf for studying the magnetic field strength inside and around the car. The prototype consists of a power converter to supply high-frequency alternating currents, a transmitter pad placed on the ground and a receiver pad on the EV (Figure 6.1).

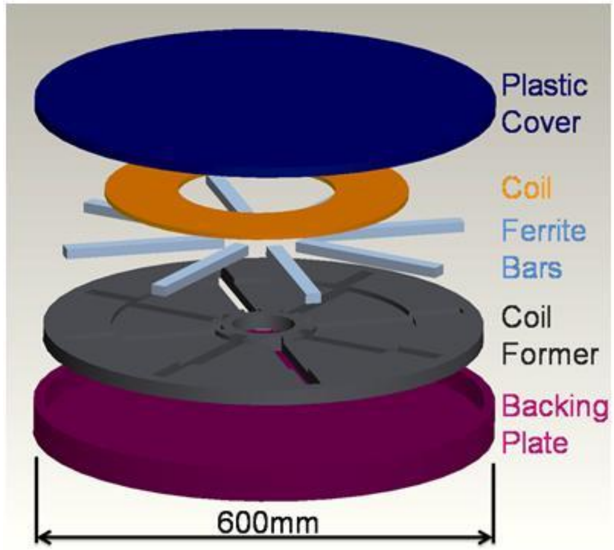
Plastic Cover
Coil
Ferrite Bars
Coil Former
Backing Plate
600mm

(a)

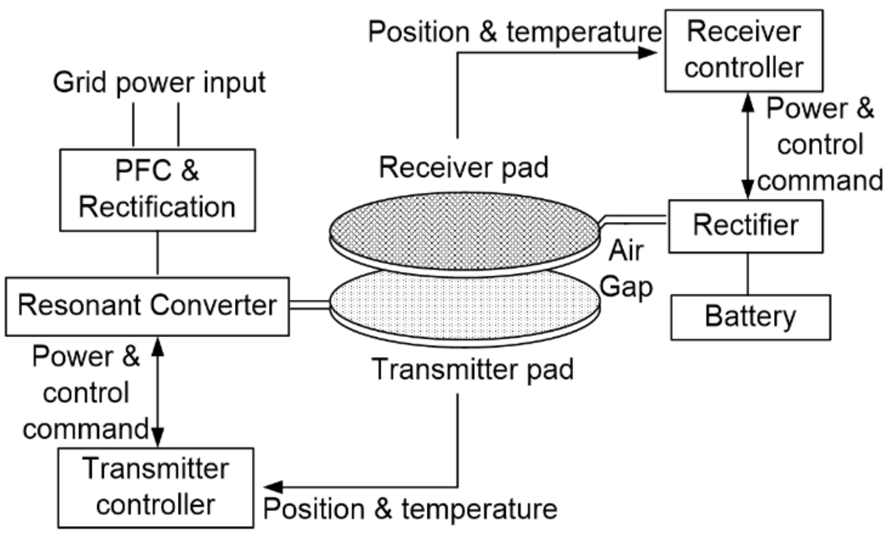
Position & temperature
Receiver controller
Grid power input
Power & control command
PFC & Rectification
Receiver pad
Rectifier
Air Gap
Resonant Converter
Battery
Transmitter pad
Power & control command
Transmitter controller
Position & temperature

(b)

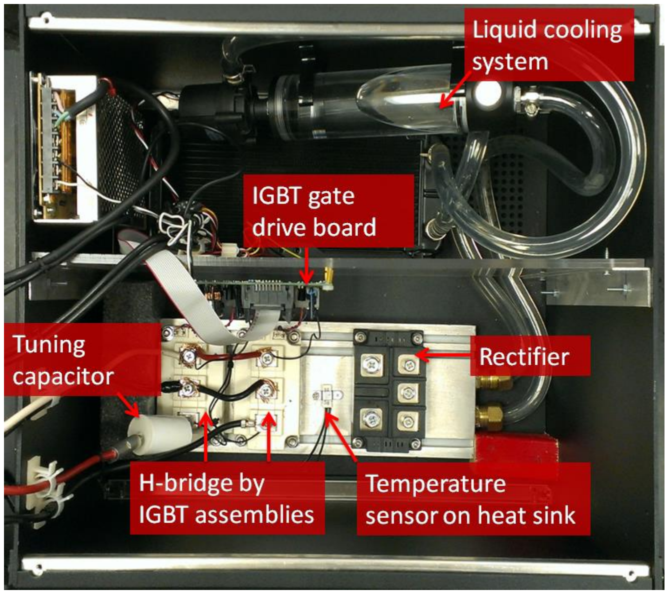

(c)

Figure 6.3. (a) Diagram of coil mechanical design; (b) EVWC system overview; (c) Photo of the power inverter setup.

The transmitter and receiver pads (Figure 6.3(a)) were constructed of a backing plate, a coil former, ferrite bars, a coil, and a plastic cover. The coil was made of copper tube windings, 60cm in coil diameter, with matched tuning capacitors to form a capacitive-inductive circuit resonating at 18-20 kHz, depending on the load and the power the system delivers. A hollow core copper tubing with an outside diameter of 3/8" was chosen to maximize heat dissipation, and minimize resistance due to the skin effect. A soft ferrite-bar structure (Ferroxcube 3C94) was mounted in the coil former under each coil to shape the magnetic flux flow and improve the power transfer efficiency. A plastic insulation case was mounted over each coil.

The schematic diagram in Figure 6.3(b) illustrates the components of the EVWC system. Grid power is first rectified to convert from AC to DC, and then regulated by a Power Factor Controller (PFC) to allow the power to be delivered at maximum efficiency. The current goes through a resonant converter, which drives the transmitter coil to generate high-frequency electromagnetic fields.

Figure 6.3(c) shows the H-bridge packaged with liquid cooling. Two half-bridge Insulated Gate Bipolar Transistor (IGBT) modules (FF100R12K4, Infineon) are employed to form the H-bridge controlled by a four-channel gate drive board. Since the IGBT can support a higher power rating than 3.3kW with liquid cooling, the power inverter can be upgraded to a higher power level with minor changes. A high-frequency voltage is induced at the receiver side and a rectifier is used to output DC voltage. The Pulse Width Modulation (PWM) signals, voltage and current on both sides, as well as the temperature of the heat sink, are processed by the transmitter and receiver controllers (CompactRIO, NI, Austin, TX). A LabView program was developed to monitor and process the control signals, efficiency and temperature. Figure 6.4 shows the EVWC system installed on a Nissan Leaf to test the system's safety.

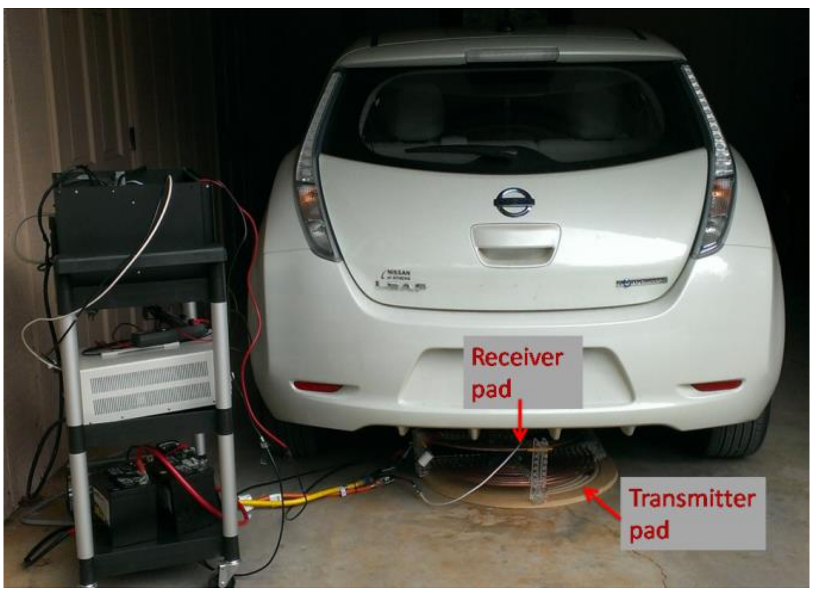

Figure 6.4. WC system implemented on a Nissan Leaf

6.3.4 Gapping and Misalignment Effects on Efficiency

Figure 6.5 shows a 3-axis motorized platform that tests wireless power transmission changes due to the changing air gap between the coils as well as horizontal misalignment. Relative air gap ratio *m* and misalignment ratio *t* are defined to normalize our testing results. The air gap ratio *m* equals gap *g* divided by coil diameter *d*, while *t* is lateral offset *l* divided by *d* (Figure 6.5(a)). The receiver coil is fixed on the platform and its motion path is programmable to meet testing requirements. In Figure 6.5, a vector network analyzer (VNA) was applied to analyze the power transfer efficiency, coupling coefficient and resonant frequency. The transmission (S_{21}) and reflection wave ratios (S_{11}) in the frequency-space domain were mapped according to the spatial allocation of the coils. The power transmission efficiency η_{21} and reflection ratio η_{11} were calculated from equations (6.3) and (6.4). The coupling coefficient *k* was deduced using equation (6.5), where f_e and f_m ($f_e > f_m$) are the two resonant frequencies of the coil setup, which are subject to the air gap and misalignment of the coils. For detailed theoretical analysis, refer to Imura et al. [111].

$$\eta_{21} = S_{21}^2 \tag{6.3}$$

$$\eta_{11} = S_{11}^2 \tag{6.4}$$

$$k = \frac{f_e^2 - f_m^2}{f_e^2 + f_m^2} \tag{6.5}$$

Figure 6.5(b) shows the 3-axis platform modified from a CNC machine (Model DHC, PlasmaCAM, Inc., Colorado City, Co, U.S.) which measures 1.75m wide, 1.65m deep, and 2.30m high. Its maximum speeds are 25m/min in the horizontal direction, and 2m/min in the vertical direction. The moveable range is 1.2m×1.2m in the horizontal plane and 0.6m in the vertical direction (Figure 6.5(b)).

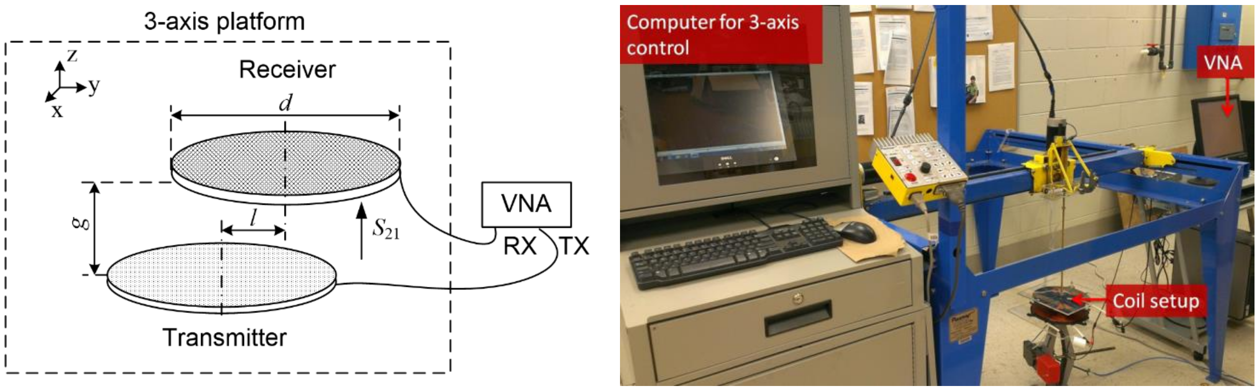

(a) (b)

Figure 6.5. (a) Testing principle; (b) Experimental setup for misalignment study

The transmission and reflection ratios on the VNA were recorded to analyze the efficiency and magnetic coupling coefficient in the air gap and misalignment experiments. Since the coil shape is circular, the misalignment test needed only to be performed in a single direction in the horizontal plane. For the misalignment tests, the air gap ratio was set at 0, 0.25, 0.5, and 0.75, and the measurement results were recorded for misalignment ratios ranging from -1.5 to 1.5.

6.4 SAFETY CONCERNS FOR EVWC

As WC systems operate at an increasingly high power level which may be up to 100kW for heavy duty EV applications, the produced electromagnetic (EM) fields between or around the charging pads should be measured to ensure a safe zone for humans. The induced voltage may also potentially damage electronic devices. In addition, heating effects on metal should be taken into consideration.

6.4.1. Human Exposure to Electromagnetic Fields

Human exposure to EM fields is the biggest safety concern for EVWC systems, since the generated EM fields could produce direct effects on the human body. Thus, the levels of EM fields inside and around the WC were measured.

Two kinds of guidelines were formulated for Human Exposure to Electromagnetic field: one was from the International Commission on Non-ionizing Radiation Protection (ICNIRP), and the other was IEEE C95.1, issued by the International Committee on Electromagnetic Safety (ICES) under the Institute of Electrical and Electronic Engineers (IEEE) [117]. The basic restrictions on EM exposure between 10 kHz to 100 kHz from ICNIRP are much more conservative than those in IEEE C95.1 [123, 124]. The ICNIRP reference level for general public exposure to time-varying EM fields is 6.25 μT, which is much lower than the IEEE level of more than 100 μT [117, 123, 124]. Nowadays, inductive EV charging standards including SAE-J2954, UL2750 and ISO/IEC PT61980 employ the ICNIRP guidelines to define limits on human exposure to EM fields [55, 63, 125]. SAE-J2954, issued by the Society of Automotive Engineers (SAE), is an operating and safety standard for wireless charging of electric and plug-in hybrid vehicles. UL2750 is another wireless EV charging safety standard outlined by Underwriters Laboratories (UL). PT61980 is a technical specification defining requirements of safety, communication and EM fields for wireless EV charging, which is from a joint working group of International organization for Standardization (ISO) and International Electrotechnical Commission (IEC). In addition, the ICNIRP guidelines have been adopted by many European and Oceanic countries [63]. Although standards have been proposed regarding human exposure on EM fields. The scope of this study is limited within the EM health study in EV wireless charging using ICNIRP guidelines.

SAE-J2954 sets general requirements for the industry to design wireless EV chargers. It includes safety, communication, positioning, and power transfer. For safety, it requires functions of object (debris and organic) detection, and EM exposure consideration. However, it does not include any particular testing results or safety regulations for EV users.

ICNIRP issued guidelines on human's exposures to EM fields in 1998 and 2010 separately. The ICNIRP 1998 covers the frequency range up to 300 GHz while the ICNIRP 2010 ranges from 1 Hz to 100 kHz [123, 124]. The ICNIRP 1998 guidelines use current intensity J to set standards; however, the internal electrical field E is used in ICNIRP 2010 [123, 124]. The relationship between the current density J and the internal electrical field E is defined by Ohm's Law: $J=\sigma E$, in which σ is the electrical conductivity of the body tissue. The magnetic field reference level in ICNIRP 1998 is more conservative than that in ICNIRP 2010, especially for frequencies ranging from 10 kHz to 100 kHz, which includes the switching frequencies commonly used by EV wireless chargers. However, there is no significant difference in the electrical field reference level between ICNIRP 1998 and 2010 [123, 124].

ICNIRP does not describe specific measurement techniques to determine EM limits on the human body. However, measurement techniques have been proposed by the Australian Radiation Protection and Nuclear Safety Agency (ARPANSA), which use the ICNIRP guidelines to define human exposure standards [126].

The test for human exposure to EM fields was conducted on a Nissan Leaf EV (body materials: galvanized steel/aluminum) fitted with the WPT prototype, and the field strengths inside the car were measured to evaluate the safety for passengers inside during WC. Figure 6.6(a) shows that the field strengths at the head, chest, groin, and knees were measured using a gauss meter (Model # UHS2, Alphalab. Inc., Utah, U.S.), according to the ICNIRP standards [1, 124]. Meanwhile, the field strengths were also mapped outside the vehicle. The system power was set at 2kW. The WPT experiment was performed on an open asphalt road between 2 brick walls 3m apart from each other. The tested EV was parked 1.5m from one of the walls, as shown in Figure 6.6(b). In real world applications, a small kid might crawl underneath the car while a parent turns their back to carry in a load of groceries or perform other tasks, so the field between the primary and secondary coils during charging as well as the associated influence to human were also studied. Although the ICNIRP has not set safety standards for pet exposure to EM, we assume the same standards for pets as for humans since the physiology is similar. Moreover, the fields inside the vehicle were also measured at the seat, head cushion, and floor carpet surface.

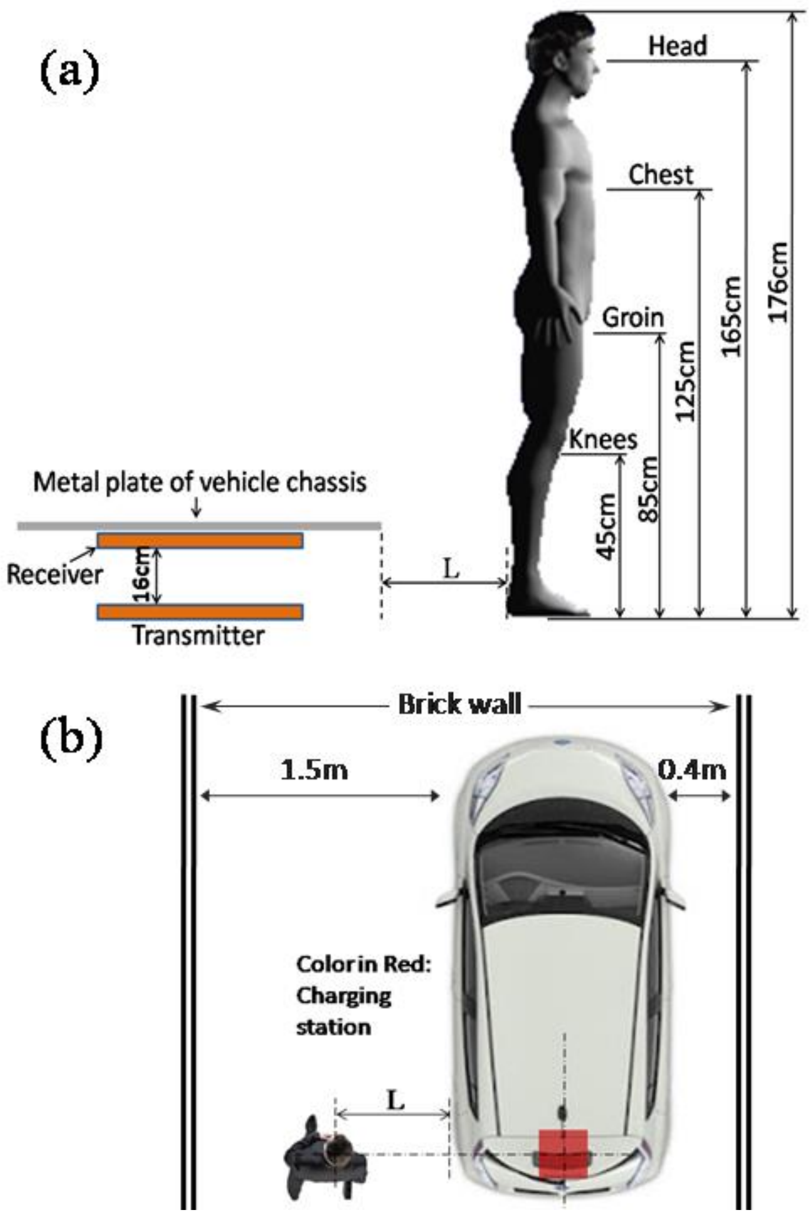

Figure 6.6. (a) EM field measurement on a standard adult human body [1]; (b) Top view of the test environment

6.4.2 Potential Damage to Electronics

Figure 6.7. Two testing objects for measuring WC-induced voltage: (a) Test piece #1 – iPhone 5 mockup (123.8mm×58.6mm, rounded with aluminum foil over the edge); (b) Test piece #2 – iPad3 mockup (241.2mm×185.7mm, rounded with aluminum foil over the edge).

Figure 6.7 shows two aluminum foil mockups used for measuring the WC-induced voltage. Two test pieces were used to simulate the induced voltage level inside electronic devices of similar sizes under a strong EM field. Each test piece was placed at the center of the coil, and then moved incrementally away until its center was aligned with the coil edge. Test pieces #1 and #2 were placed on the transmitter in parallel with a 1MΩ resistor to measure WC-induced voltages with an oscilloscope. The power level was set at 1.2kW. All the test pieces were galvanically isolated from the transmitter pad.

6.4.3 Thermal Effects

Eddy currents are generated in conductors when exposed to changing magnetic flux. This phenomenon can produce heat, such as in induction cooking. Similarly, metal debris is likely to be thrown on the WPT charging pad during charging, causing potential hazards such as fire. In our experiment, a 330mL aluminum soda can was placed a half-radius away from the pad center to study the heating effect under power levels varying from 1.1kW to 3.1kW in a worst case scenario.

6.5 RESULTS AND DISCUSSION

6.5.1 Efficiency

6.5.1.1. Air Gaps

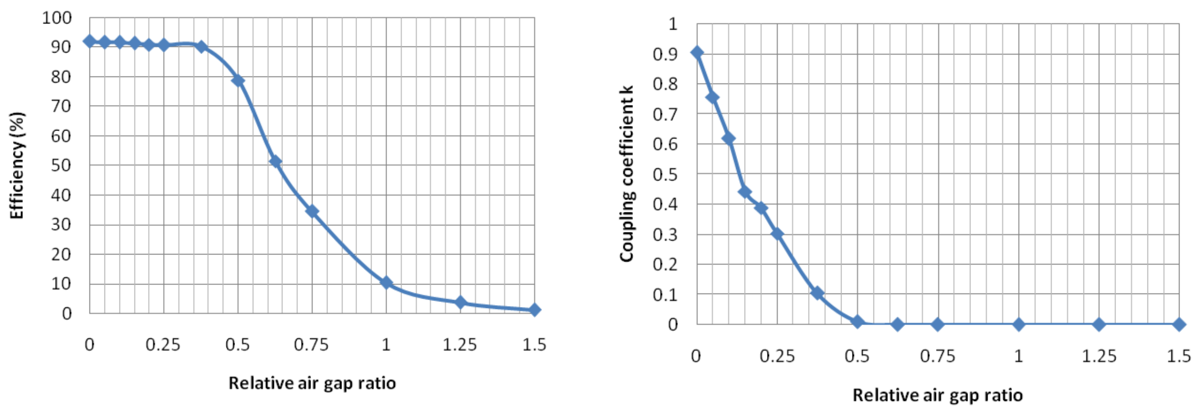

(a) (b)

Figure 6.8. (a) Relationship between power transfer efficiency and normalized air gaps; (b) Coupling coefficient vs. normalized air gaps

Figure 6.8(a) shows the maximum efficiency values at different normalized air gaps. Figure 6.8(b) is the relationship between coil coupling and air gaps, where the coupling becomes weaker with the increase in gap ratio, affecting the system impedance, as well as the resonance and efficiency. Although the power transfer efficiency can be improved by adding an impedance network to the system, in this experiment the impedance of the transmitter and receiver coils was not actively adjusted to simplify the experimental design, as the main focus of this paper is the safety of the wireless charger. As the air gap increases, the maximum efficiency stays at 90% while the coupling factor is only 0.11. Then the efficiency drops to 79% at a coupling factor of 0.01, meaning that the magnetic resonance coupling can still maintain a high value even when the coupling is as low as 0.01. This feature of magnetic resonance coupling allows wireless power transfer over a long distance at a reasonable efficiency.

Figure 6.9 shows the power transmission and reflection ratios η_{21} and η_{11} versus changes in frequency under air gap ratios of m=0, 0.25, 0.5 and 0.75. Two resonant frequencies exist for the cases of m= 0-0.5 where the air gap distances are small and the associated coupling factors are great. The first, lower resonant frequency presents a higher efficiency than the second one. As the air gap increases, the two resonant frequencies move closer and eventually merge into one, followed by a dramatic decrease in the corresponding efficiency.

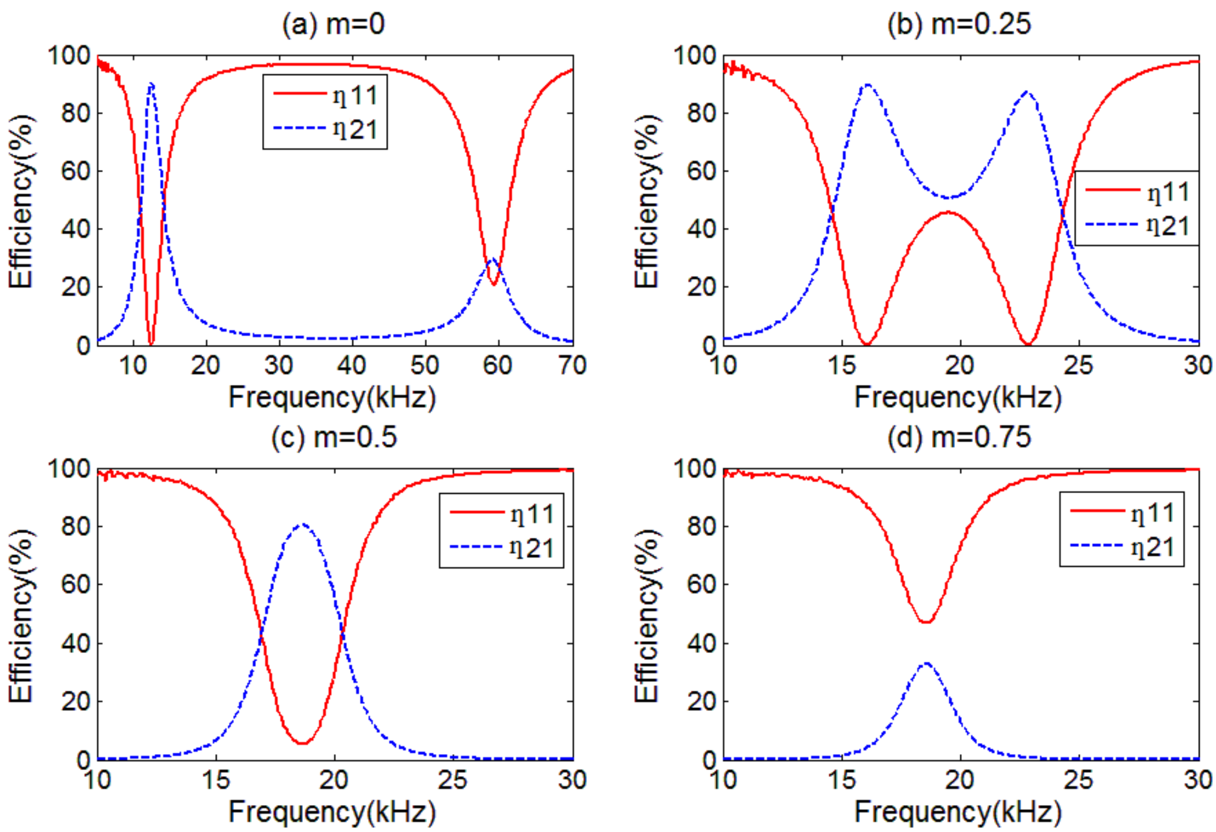

Figure 6.9. Relationship between efficiency and frequency at varying air gap ratios of m = 0, 0.25, 0.5, and 0.75, where m is defined as the distance between the primary and secondary coils divided by the coil diameter.

6.5.1.2 Misalignment

Figure 6.10(a) shows the efficiency vs. misalignment ratio curve at four different air gap ratios. When the air gap ratio is set at 0 and 0.25, the efficiency remains at 90% as long as the misalignment ratio is within 0.5, which shows that the magnetic resonance coupling allows a relatively large misalignment. When the air gap is zero (m=0), the efficiency curve has a peak value of 64% at the normal misalignment ratio of 0.75. This low efficiency might be due to the coil structure (the coil center was not covered with copper tubing and ferrite materials), which allowed more than one magnetic coupling peak to exist. As the misalignment ratio changes from -0.5 to 0.5, the efficiency curve becomes flat due to the relatively strong couplings maintained when the two coils stay close to each other. Figure 6.10(b) shows the magnetic coupling coefficient at different air gap ratios. The efficiency maintains a high value even if the coupling factor is small, which is similar to the efficiency-gap ratio curve. When the air gap increases, the efficiency drops dramatically, just as it does with increased misalignment. Essentially, the circuit impedance is adjusted by the spatial distribution of the two coils.

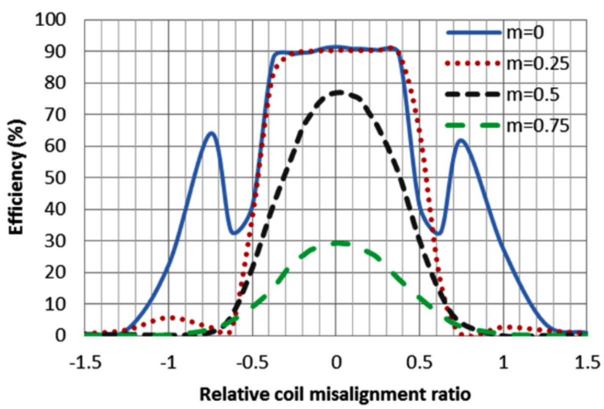

(a)

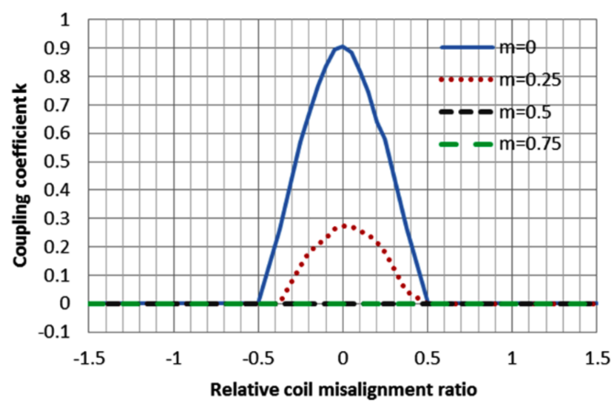

(b)

Figure 6.10. (a) Relationship between efficiency and misalignment ratio under relative air gap ratios of m = 0, 0.25, 0.5, and 0.75; (b) Experimental results for coupling characteristics vs. misalignment ratio at relative air gap ratios of 0, 0.25, 0.5, and 0.75.

6.5.2 Human Body Exposure to Magnetic Field

Figure 6.11(a) shows the magnetic field strength at several parts of the human body, studying human exposure to the magnetic field according to the ICNIRP standards (maximum magnetic field allowed: 27.3μT; average field strength for knees, groin, chest, and head allowed: 6.25 μT). Figure 6.11(a) shows that the average magnetic field strength at the distance of 75cm was 5.83 μT, and the maximum field at this distance was 10.8 μT, meaning that the safe distance for magnetic field exposure is greater than 75cm away from the vehicle edge. In addition, the maximum field was not at the edge of the vehicle (Figure 6.11(a)). This might be due to the fact that the vehicle's metal chassis acted as EM shielding, which blocks the magnetic field induced by the EVWC system. The magnetic field between the two charging pads was also measured, with a maximum value of 1.656 mT, which largely exceeds the safety guideline imposed by the ICNIRP standard. Hence, people and pets should not be allowed between the charging pads, and the EVWC system should detect objects between the charging pads, shut down the charger and send out an alert. As the vehicle's metal chassis blocks magnetic field transmission, the field strength inside the vehicle was not more than 2 μT, no matter where it was measured. Thus, it is safe for humans inside the vehicle during charging.

The specific absorption rate (SAR) is defined as the rate at which the radio frequency energy is absorbed by the human body exposed to an electromagnetic field; for its calculation , refer to [127]. In our experiment, the SAR is 0.75 kW/kg corresponding to the maximum magnetic field (1.656 mT) between the charging pads. According to the Federal Communications Commission (FCC) standard, the SAR exceeds the safety limit of 1.6 W/kg when the human body is exposed to such a strong magnetic field [117]. The SAR is 4.5 W/kg for a magnetic field of 10 μT at the safe distance of 75cm. The measurement results of SAR and magnetic fields in our experiment can be lower than the safety limits by increasing the surface area of the shielding plate.

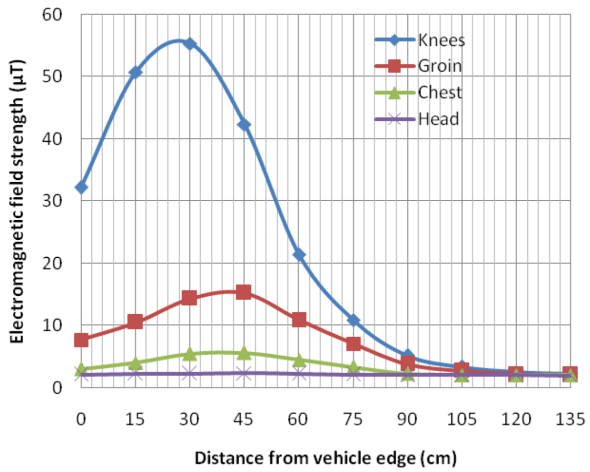

(a)

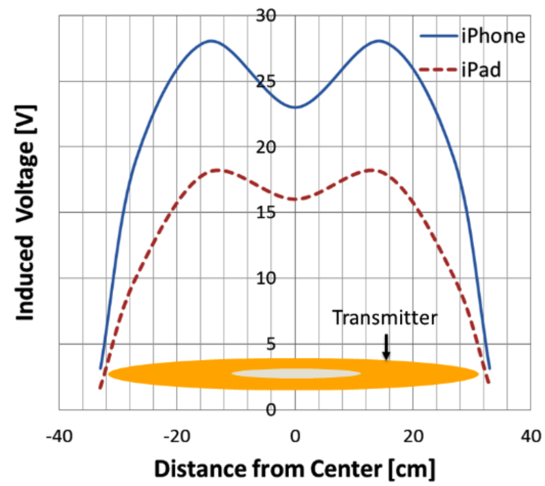

(b)

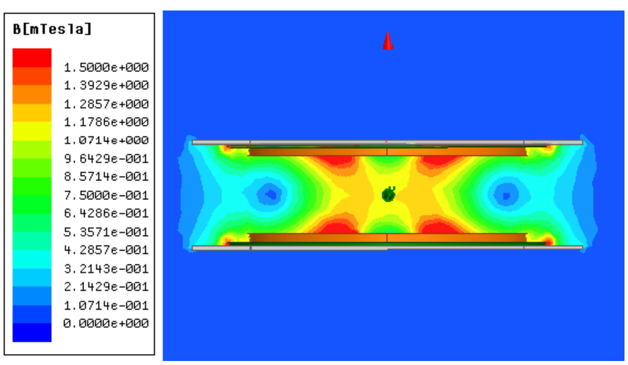

(c)

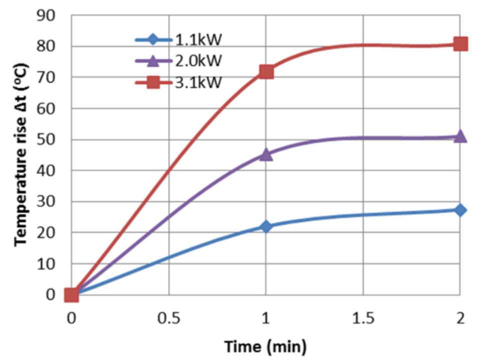

(d)

Figure 6.11. (a) Measured magnetic field distribution according to Figure 6.6; (b) EM interference for test pieces #1 and #2 at different distances from the coil center; (c) Magnetic flux distribution by FEM; (d) Temperature rise curve for a soda can put between the charging pads.

6.5.3 EMI with Electronic Devices inside the Human Body

Figure 6.11(b) depicts the relationship between the induced voltage and the corresponding distance of the electronic device test pieces from the center of the transmitting coil. The voltages rise to peaks at 16V and 23V for both test pieces at 15cm, where the maximum EM interference was. These WC-induced voltages could damage electronics and also affect the functionality of medical implants in the human body near the WC system. Decreases in induced voltage were observed when the displacement increased, while reaching 1.75V and 3.16V at the coil circumference. The induced voltage was slightly smaller than the peak value at the coil center; the voltage drop at the center results from the coil geometry from which the coil winding starts. Figure 6.11(c) shows the FEM magnetic flux distribution, which shows that the magnetic flux trend follows the actual measurements in Figure 6.11(b). As the system power was set at 1.2kW in the experiment, the EMI voltages could be much higher for a larger charging power, which could dramatically increase the risk to electronics.

6.5.4 Thermal Effects in a Worst Case Scenario

Figure 6.11(d) shows that the temperature of a soda can rose dramatically within 2 minutes with the temperature rise by 27℃ under 1.1kW, 51℃ under 2kW, and 81℃ under 3.1kW respectively. The original temperature of the soda can is 23℃ and the testing environment is a garage. The temperature rose much faster in the first minute than the second minute, reaching a steady temperature as time went on. Such high temperatures could cause an explosion for an unopened soda can, or skin burns for people who touch or pick up the soda can. The metal material of an aluminum soda can also lower the system efficiency by partially blocking the magnetic fields. Thus, metal plates or conductors should not be allowed between the charging and receiving pads. A metal detection system should be in place in WC charging. Possible methods include magnetic sensing, vision detection, capacitive sensing, etc [128, 129]. Moreover, as the energy is dissipated through the heating effects, the WPT efficiency is lowered. Thus, metal debris in wireless charging should be detected and removed in order to maintain safety and high efficiency.

6.6 CONCLUSION

EM considerations and some safety issues and misalignment effects on efficiency were studied for the EVWC system. A 3.3 kW EVWC prototype was developed for testing purposes. The safety issues were investigated with two sizes of electronic appliance mockups at various WC power levels. Debris was placed near and inside the EVWC system to investigate heating effects. A motorized 3-axis platform was applied to study the effects on efficiency caused by misalignment. Tests were conducted to determine the safe distance for humans/pets near a charging EV. Our experimental results demonstrate that significant adverse effects could occur in the forms of heating and EM interference when the test pieces were introduced, with potential damage to the human body, animals and electronic devices near the EVWC system. Several design and operational recommendations are given based on our experiments: (1) a distance of at least 75cm should be kept between humans and the EVWC system during charging (this distance is obtained at a power level of 2kW, and should be adjusted based on the power level); (2) patients with medical implants should consult their doctor/surgeon/device specialist before using wireless charging; (3) Electronic devices should not be placed between the charging coils to avoid possible damage. Finally, the results also indicate that although magnetic resonance allows a high efficiency for WPT, coil misalignment could have a significant influence on the power transfer efficiency. In order to eliminate misalignment, an automated vehicle alignment system should be in place to navigate parking accurately. As the SAE J2954 chooses a nominal frequency of 85 kHz for light duty EV wireless chargers after taking into account factors such as the cost of high frequency/power switching devices and interference issues, the switching frequency in our future WPT designs will also follow this trend.

CHAPTER 7

CONCLUSIONS AND FUTURE RESEARCH

7.1 RESEARCH SUMMARY AND CONCLUSIONS

This dissertation investigates frequency control, modeling, alignment detection and health considerations and safety concerns associated with EV wireless charging. The methodology presented in this dissertation can offer novel or alternative approaches to allow for efficient, adaptive, and safe wireless charging.

The first part of the dissertation (Chapter 2) is about modeling and control of IPT electronics for maximum efficiency operations. Chapter 2 researched a uniform voltage gain control for wireless charging that can generate a stable and controllable voltage to address the negative effects of misalignment and air gap variations in EV applications. The uniform voltage gain control offers certain advantages, as shown by the theoretical analysis and experimental demonstration. Firstly, the uniform gain control allows for operation under greater misalignment and is more robust under different vehicle chassis heights. Secondly, although the WPT system does not operate at the resonance frequency under uniform control, it does not mean the overall efficiency is low. Lower current operation and use of soft switching can decrease the power loss caused by switching devices. Hence, uniform gain control can have a higher efficiency compared to resonant operation under coupling variations.

The second part of this dissertation (Chapter 3) is about modeling a SS resonant converter for WPT. In Chapter 3, the proposed frequency-spacing model allows the unity-gain frequency of a SS IPT system to be computed in about 10ms. The unity-gain frequency is the frequency at which the SS IPT transfers power at its maximum efficiency. This process requires no measurement or finite element analysis to acquire the mutual inductance in IPT; it is a direct way to calculate the unity-gain frequency. The average gain value for all twenty-four configurations in the experiment is 0.98, and the gain stability at any air gap is within 3% under three different loads.

The third part of the dissertation (Chapter 4 &5) solves the vehicle misalignment issues by introducing a magnetic alignment system which can assist an EV driver in parking to allow both coils to be well aligned. The system applies four auxiliary coils to detect the direction and relative position and reduces system complexity and cost by sharing the wireless charging platform. The measurement principle of Chapter 4 is that the coupling coefficient and resonance frequency correspond to the position and it can achieve an accuracy of 1.2cm when the detection range is <15cm. Since the circulating current can be huge for a weak coupling between the two coils, this approach has limited detection range (<25cm). To address this issue, Chapter 5 illustrates a three dimensional alignment system by measuring output voltages of the four auxiliary coils and the relation between the four outputs and coordinate in 3D was derived in the chapter. In Chapter 5, 92.5% of the tested samples have an error of less than 2cm and 98% have an error of less than 3cm. The air gap estimation also shows high accuracy, with maximum error of 0.6cm and mean error of 0.25cm. The proposed 3D positioning system is a highly valuable approach to aligning coils for efficient wireless EV charging.

The fourth part of the dissertation (Chapter 6) investigates safety concerns associated with a 3kW wireless charging prototype. The concern about human exposure to EM fields was tested on the prototype. A distance of at least 75cm is recommended to be kept between humans and the WC system during charging (this distance is obtained at a power level of 2kW, and should be adjusted based on the power level). Considering the vehicle width is normally more than 2m, the EM emission is within safe range for the same power level. The testing results also recommend that patients with medical implants should consult their doctor/surgeon/device specialist before using wireless charging. Since the magnetic field between coupled coils is strong (mT level), electronic devices should not be placed between the charging coils to avoid possible damage.

7.2 FUTURE WORK

7.2.1 Uniform gain control

Chapter 2 demonstrates a uniform gain control method for a series-parallel WPT topology that improves the system performance in terms of efficiency and power delivery for coupling variations compared with fixed and resonant frequency control. The future work can be studying other circuit topologies such as LCL and LCC and exploring their potentials from the perspective of power control, efficiency, load, and coupling coefficient. Since two identical circular coils are employed in this chapter, an asymmetrical coil setup or symmetrical coils with different separations among the turns can be investigated as the future work. These two coil configurations might have better performance and coupling than the circular pad under air gap change and misalignment.

7.2.2 Frequency-spacing modeling

The theoretical relation between IPT frequency and spatial distribution of coils is derived in this dissertation, which shows faster speed than FEA simulation for calculation of coupling coefficient and frequency. However, the model assumes that the two coupled coils are circular in shape and are in parallel with each other, which means that it will not function for noncircular coils. Thus, the future work should be making the model be compatible with rectangular coils and taking coil orientation into account. In addition, Chapter 3 does not include simulation results for the three-dimensional modeling. Therefore, further experiment and FEA simulation can be conducted to validate the model.

7.2.3 Magnetic alignment for EVWC

This dissertation describes a conceptual design of a 3D magnetic approach by applying existing wireless charging hardware. Further study should be testing the prototype on an EV to see whether the vehicle body and jitter can affect its accuracy. Moreover, since the prototype uses circular coils, the following research can take rectangular coils into consideration. The current prototype applies four auxiliary minor coils for positioning the secondary. Hence, another interesting research direction would be optimization of the auxiliary coil configuration by investigating the influence of the number of auxiliary coils on the positioning accuracy.

7.2.4 Safety concerns in EVWC

Chapter 6 presents magnetic emissions and safety concerns with wireless EV chargers. The following work can be coordination with safety science institutes to investigate the possibility how it can be referenced in industry.

REFERENCES

[1] C. L. Ogden and N. C. f. H. Statistics, *Mean body weight, height, and body mass index: United States 1960-2002*: Department of Health and Human Services, Centers for Disease Control and Prevention, National Center for Health Statistics, 2004.

[2] G. C. Corazza, "Marconi's history [radiocommunication]," *Proceedings of the IEEE,* vol. 86, pp. 1307-1311, 1998.

[3] J. Miller and A. Daga, "Elements of Wireless Power Transfer Essential to High Power Charging of Heavy Duty Vehicles," *Transportation Electrification, IEEE Transactions on,* vol. 1, pp. 26 - 39, 2015.

[4] J. Dai and D. C. Ludois, "A survey of wireless power transfer and a critical comparison of inductive and capacitive coupling for small gap applications," *Power Electronics, IEEE Transactions on,* vol. 30, pp. 6017-6029, 2015.

[5] W. C. Brown, "The history of power transmission by radio waves," *Microwave Theory and Techniques, IEEE Transactions on,* vol. 32, pp. 1230-1242, 1984.

[6] S. Li and C. C. Mi, "Wireless power transfer for electric vehicle applications," *Emerging and Selected Topics in Power Electronics, IEEE Journal of,* vol. 3, pp. 4-17, 2015.

[7] G. A. Covic and J. T. Boys, "Modern trends in inductive power transfer for transportation applications," *Emerging and Selected Topics in Power Electronics, IEEE Journal of,* vol. 1, pp. 28-41, 2013.

[8] F. Musavi and W. Eberle, "Overview of wireless power transfer technologies for electric vehicle battery charging," *Power Electronics, IET,* vol. 7, pp. 60-66, 2014.

[9] S. Y. R. Hui, W. Zhong, and C. K. Lee, "A critical review of recent progress in mid-range wireless power transfer," *Power Electronics, IEEE Transactions on,* vol. 29, pp. 4500-4511, 2014.

[10] N. Shinohara, *Wireless power transfer via radiowaves*: John Wiley & Sons, 2014.

[11] T. Sun, X. Xie, and Z. Wang, *Wireless power transfer for medical microsystems*: Springer, 2013.

[12] J. I. Agbinya, *Wireless power transfer*: River Publishers, 2012.

[13] P. Jaffe, J. Hodkin, and F. Harrington, "Development of a sandwich module prototype for space solar power," in *Aerospace Conference, 2012 IEEE*, 2012, pp. 1-9.

[14] W. Zhong, X. Liu, and S. R. Hui, "A novel single-layer winding array and receiver coil structure for contactless battery charging systems with free-positioning and localized charging features," *Industrial Electronics, IEEE Transactions on,* vol. 58, pp. 4136-4144, 2011.

[15] W. Zhong, C. K. Lee, and S. R. Hui, "General analysis on the use of Tesla's resonators in domino forms for wireless power transfer," *Industrial Electronics, IEEE Transactions on,* vol. 60, pp. 261-270, 2013.

[16] T. M. Fisher, K. B. Farley, Y. Gao, H. Bai, and Z. T. H. Tse, "Electric vehicle wireless charging technology: a state-of-the-art review of magnetic coupling systems," *Wireless Power Transfer,* vol. 1, pp. 87-96, 2014.

[17] P. Si, A. P. Hu, S. Malpas, and D. Budgett, "A frequency control method for regulating wireless power to implantable devices," *Biomedical Circuits and Systems, IEEE Transactions on,* vol. 2, pp. 22-29, 2008.

[18] V. Talla, B. Kellogg, B. Ransford, S. Naderiparizi, S. Gollakota, and J. R. Smith, "Powering the next billion devices with wi-fi," *arXiv preprint arXiv:1505.06815*, 2015.

[19] R. S. Y. Hui and S. C. Tang, "Planar printed-circuit-board transformers with effective electromagnetic interference (EMI) shielding," ed: Google Patents, 2002.

[20] P. Jaffe and J. McSpadden, "Energy conversion and transmission modules for space solar power," *Proceedings of the IEEE*, vol. 101, pp. 1424-1437, 2013.

[21] X. Lu, P. Wang, D. Niyato, D. I. Kim, and Z. Han, "Wireless Charging Technologies: Fundamentals, Standards, and Network Applications," 2015.

[22] P. Kale, A. Bothra, A. Jangid, L. Goski, and N. Harwande, "Wireless Power Transmission using Wi-Fi Signals," *channels*, 2016.

[23] M. Kline, I. Izyumin, B. Boser, and S. Sanders, "Capacitive power transfer for contactless charging," in *Applied Power Electronics Conference and Exposition (APEC), 2011 Twenty-Sixth Annual IEEE*, 2011, pp. 1398-1404.

[24] S. Hasanzadeh and S. Vaez-Zadeh, "A Review of Contactless Electrical Power Transfer: Applications, Challenges and Future Trends," *Automatika–Journal for Control, Measurement, Electronics, Computing and Communications*, vol. 56, 2015.

[25] A. Kumar, S. Pervaiz, C.-K. Chang, S. Korhummel, Z. Popovic, and K. K. Afridi, "Investigation of power transfer density enhancement in large air-gap capacitive wireless power transfer systems," in *Wireless Power Transfer Conference (WPTC), 2015 IEEE*, 2015, pp. 1-4.

[26] B. Lenaerts and R. Puers, *Omnidirectional inductive powering for biomedical implants*: Springer, 2009.

[27] Z. Yuwei, H. Xueliang, T. Linlin, B. Yang, and Z. Jianhua, "Current research situation and developing tendency about wireless power transmission," in *Electrical and Control Engineering (ICECE), 2010 International Conference on*, 2010, pp. 3507-3511.

[28] N. Tesla, "Apparatus for transmitting electrical energy," ed: Google Patents, 1914.

[29] H. H. Wu, A. Gilchrist, K. Sealy, P. Israelsen, and J. Muhs, "A review on inductive charging for electric vehicles," in *Electric Machines & Drives Conference (IEMDC), 2011 IEEE International*, 2011, pp. 143-147.

[30] J. T. Boys and A. W. Green, "Inductive power distribution system," ed: Google Patents, 1994.

[31] I. Systems Control Technology, "Roadway Powered Electric Vehicle Project Track Construction And Testing Program Phase 3D," ed, 1994.

[32] S. E. Shladover, "Path at 20-history and major milestones," *IEEE Transactions on intelligent transportation systems*, vol. 8, pp. 584-592, 2007.

[33] G. A. Covic and J. T. Boys, "Inductive power transfer," *Proceedings of the IEEE,* vol. 101, pp. 1276-1289, 2013.

[34] S. Lee, J. Huh, C. Park, N.-S. Choi, G.-H. Cho, and C.-T. Rim, "On-line electric vehicle using inductive power transfer system," in *Energy Conversion Congress and Exposition (ECCE), 2010 IEEE*, 2010, pp. 1598-1601.

[35] I.-S. Suh and J. Kim, "Electric vehicle on-road dynamic charging system with wireless power transfer technology," in *Electric Machines & Drives Conference (IEMDC), 2013 IEEE International*, 2013, pp. 234-240.

[36] A. Brecher and D. Arthur, "Review and Evaluation of Wireless Power Transfer (WPT) for Electric Transit Applications," 2014.

[37] N. P. Suh, "Design of wireless electric power transfer technology: shaped magnetic field in resonance (SMFIR)," in *Proceedings of the 2011 CIRP Design Conference at KAIST, Korea*, 2011.

[38] C. Zheng, J.-S. Lai, R. Chen, W. E. Faraci, Z. Ullah Zahid, B. Gu, *et al.*, "High-efficiency contactless power transfer system for electric vehicle battery charging application," *Emerging and Selected Topics in Power Electronics, IEEE Journal of,* vol. 3, pp. 65-74, 2015.

[39] N. Liu and T. G. Habetler, "Design of a Universal Inductive Charger for Multiple Electric Vehicle Models," *Power Electronics, IEEE Transactions on,* vol. 30, pp. 6378 - 6390, 2015.

[40] K. Colak, M. Bojarski, E. Asa, and D. Czarkowski, "A constant resistance analysis and control of cascaded buck and boost converter for wireless EV chargers," in *Applied Power Electronics Conference and Exposition (APEC), 2015 IEEE*, 2015, pp. 3157-3161.

[41] K. Colak, E. Asa, M. Bojarski, D. Czarkowski, and O. C. Onar, "A Novel Phase-Shift Control of Semibridgeless Active Rectifier for Wireless Power Transfer," *Power Electronics, IEEE Transactions on,* vol. 30, pp. 6288-6297, 2015.

[42] C. Zheng, H. Ma, J.-S. Lai, and L. Zhang, "Design Considerations to Reduce Gap Variation and Misalignment Effects for the Inductive Power Transfer System," *Power Electronics, IEEE Transactions on,* vol. 30, pp. 6108-6119, 2015.

[43] S. Li, W. Li, J. Deng, T. D. Nguyen, and C. C. Mi, "A double-sided LCC compensation network and its tuning method for wireless power transfer," *Vehicular Technology, IEEE Transactions on,* vol. 64, pp. 2261-2273, 2015.

[44] J. Deng, W. Li, T.-D. Nguyen, S. Li, and C. Mi, "Compact and Efficient Bipolar Pads for Wireless Power Chargers: Design and Analysis," *Power Electronics, IEEE Transactions on,* vol. 20, pp. 6130 - 6140, 2015.

[45] M. Bojarski, E. Asa, M. T. Outeiro, and D. Czarkowski, "Control and analysis of multi-level type multi-phase resonant converter for wireless EV charging," in *Industrial Electronics Society, IECON 2015-41st Annual Conference of the IEEE*, 2015, pp. 005008-005013.

[46] J. C. Quinn, B. J. Limb, Z. Pantic, P. Barr, and R. Zane, "Techno-economic feasibly and environmental impact of wireless power transfer roadway electrification," in *Wireless Power Transfer Conference (WPTC), 2015 IEEE*, 2015, pp. 1-3.

[47] J. M. Miller, P. Jones, J.-M. Li, and O. C. Onar, "ORNL Experience and Challenges Facing Dynamic Wireless Power Charging of EV's," *Circuits and Systems Magazine, IEEE,* vol. 15, pp. 40-53, 2015.

[48] J. M. Miller, O. C. Onar, and M. Chinthavali, "Primary-Side Power Flow Control of Wireless Power Transfer for Electric Vehicle Charging," *Emerging and Selected Topics in Power Electronics, IEEE Journal of,* vol. 3, pp. 147-162, 2015.

[49] O. C. Onar, J. M. Miller, S. L. Campbell, C. Coomer, C. White, and L. E. Seiber, "A novel wireless power transfer for in-motion EV/PHEV charging," in *Applied Power Electronics Conference and Exposition (APEC), 2013 Twenty-Eighth Annual IEEE*, 2013, pp. 3073-3080.

[50] Y. Zhang, K. Chen, F. He, Z. Zhao, T. Lu, and L. Yuan, "Closed-Form Oriented Modeling and Analysis of Wireless Power Transfer System With Constant-Voltage

Source and Load," *Power Electronics, IEEE Transactions on,* vol. 31, pp. 3472-3481, 2016.

[51] J. M. Miller, C. P. White, O. C. Onar, and P. M. Ryan, "Grid side regulation of wireless power charging of plug-in electric vehicles," in *Energy Conversion Congress and Exposition (ECCE), 2012 IEEE*, 2012, pp. 261-268.

[52] M. Chinthavali, O. C. Onar, S. L. Campbell, and L. Tolbert, "Integrated charger with wireless charging and boost functions for PHEV and EV applications," in *Transportation Electrification Conference and Expo (ITEC), 2015 IEEE*, 2015, pp. 1-8.

[53] Y. SUZUKI, M. MIZUTANI, T. SUGIURA, N. SAKAI, and T. OHIRA, "Prototype Experiments on a 1/32-Scale Model Via-Wheel Power Transfer Electric Vehicle," *Electrical Engineering in Japan,* vol. 195, pp. 63-71, 2016.

[54] Y. Suzuki, T. Sugiura, N. Sakai, M. Hanazawa, and T. Ohira, "Dielectric coupling from electrified roadway to steel-belt tires characterized for miniature model car running demonstration," in *Microwave Workshop Series on Innovative Wireless Power Transmission: Technologies, Systems, and Applications (IMWS), 2012 IEEE MTT-S International*, 2012, pp. 35-38.

[55] J. Schneider, "SAE J2954 overview and path forward," ed, 2013.

[56] Y. Gao, K. B. Farley, A. Ginart, and Z. T. H. Tse, "Safety and efficiency of the wireless charging of electric vehicles," *Proceedings of the Institution of Mechanical Engineers, Part D: Journal of Automobile Engineering,* p. 0954407015603863, 2015.

[57] H. Shoki, "Issues and initiatives for practical deployment of wireless power transfer technologies in Japan," *Proceedings of the IEEE,* vol. 101, pp. 1312-1320, 2013.

[58] J. B. Kenney, "Dedicated short-range communications (DSRC) standards in the United States," *Proceedings of the IEEE,* vol. 99, pp. 1162-1182, 2011.

[59] A. Gil and J. Taiber, "A Literature Review in Dynamic Wireless Power Transfer for Electric Vehicles: Technology and Infrastructure Integration Challenges," in *Sustainable Automotive Technologies 2013*, ed: Springer, 2014, pp. 289-298.

[60] C. Duan, C. Jiang, A. Taylor, and K. Bai, "Design of a zero-voltage-switching large-air-gap wireless charger with low electrical stress for Plugin Hybrid Electric Vehicles," in *Transportation Electrification Conference and Expo (ITEC), 2013 IEEE*, 2013, pp. 1-5.

[61] C. Duan, C. Jiang, A. Taylor, and K. H. Bai, "Design of a zero-voltage-switching large-air-gap wireless charger with low electric stress for electric vehicles," *IET Power Electronics*, vol. 6, pp. 1742-1750, 2013.

[62] C.-S. Wang, O. H. Stielau, and G. A. Covic, "Design considerations for a contactless electric vehicle battery charger," *Industrial Electronics, IEEE Transactions on,* vol. 52, pp. 1308-1314, 2005.

[63] H. H. Wu, A. Gilchrist, K. D. Sealy, and D. Bronson, "A high efficiency 5 kW inductive charger for EVs using dual side control," *Industrial Informatics, IEEE Transactions on*, vol. 8, pp. 585-595, 2012.

[64] C.-Y. Huang, J. T. Boys, and G. A. Covic, "LCL pickup circulating current controller for inductive power transfer systems," *Power Electronics, IEEE Transactions on,* vol. 28, pp. 2081-2093, 2013.

[65] H. Hao, G. A. Covic, and J. T. Boys, "An Approximate Dynamic Model of LCL--Based Inductive Power Transfer Power Supplies," *Power Electronics, IEEE Transactions on*, vol. 29, pp. 5554-5567, 2014.

[66] T.-D. Nguyen, S. Li, W. Li, and C. C. Mi, "Feasibility study on bipolar pads for efficient wireless power chargers," in *Applied Power Electronics Conference and Exposition (APEC), 2014 Twenty-Ninth Annual IEEE*, 2014, pp. 1676-1682.

[67] M. Budhia, J. T. Boys, G. A. Covic, and C.-Y. Huang, "Development of a single-sided flux magnetic coupler for electric vehicle IPT charging systems," *Industrial Electronics, IEEE Transactions on*, vol. 60, pp. 318-328, 2013.

[68] M. Chigira, Y. Nagatsuka, Y. Kaneko, S. Abe, T. Yasuda, and A. Suzuki, "Small-size light-weight transformer with new core structure for contactless electric vehicle power transfer system," in *Energy Conversion Congress and Exposition (ECCE), 2011 IEEE*, 2011, pp. 260-266.

[69] H. Takanashi, Y. Sato, Y. Kaneko, S. Abe, and T. Yasuda, "A large air gap 3 kW wireless power transfer system for electric vehicles," in *Energy Conversion Congress and Exposition (ECCE), 2012 IEEE*, 2012, pp. 269-274.

[70] N. Liu and T. G. Habetler, "Design of an on-board charger for universal inductive charging in electric vehicles," in *Energy Conversion Congress and Exposition (ECCE), 2015 IEEE*, 2015, pp. 4544-4549.

[71] Y. Gao, K. B. Farley, and Z. T. H. Tse, "A Uniform Voltage Gain Control for Alignment Robustness in Wireless EV Charging," *Energies*, vol. 8, pp. 8355-8370, 2015.

[72] Y. Gao, A. Ginart, K. B. Farley, and Z. T. H. Tse, "Uniform-Gain Frequency Tracking of Wireless EV Charging for Improving Alignment Flexibility," presented at the Applied Power Electronics Conference and Exposition (APEC), Long Beach, CA, USA, 2016.

[73] Y. Gao, A. Ginart, K. B. Farley, and Z. T. H. Tse, "Misalignment Effect on Efficiency of Wireless Power Transfer for Electric Vehicles " presented at the Applied Power Electronics Conference and Exposition (APEC), Long Beach, CA, USA, 2016.

[74] N. S. Pearre, W. Kempton, R. L. Guensler, and V. V. Elango, "Electric vehicles: How much range is required for a day’s driving?," *Transportation Research Part C: Emerging Technologies,* vol. 19, pp. 1171-1184, 2011.

[75] C. Botsford and A. Szczepanek, "Fast charging vs. slow charging: Pros and cons for the new age of electric vehicles," in *International Battery Hybrid Fuel Cell Electric Vehicle Symposium*, 2009.

[76] J. Channegowda, V. K. Pathipati, and S. S. Williamson, "Comprehensive review and comparison of DC fast charging converter topologies: Improving electric vehicle plug-to-wheels efficiency," in *Industrial Electronics (ISIE), 2015 IEEE 24th International Symposium on*, 2015, pp. 263-268.

[77] A. Ashtari, E. Bibeau, S. Shahidinejad, and T. Molinski, "PEV charging profile prediction and analysis based on vehicle usage data," *Smart Grid, IEEE Transactions on,* vol. 3, pp. 341-350, 2012.

[78] M. Yilmaz and P. T. Krein, "Review of battery charger topologies, charging power levels, and infrastructure for plug-in electric and hybrid vehicles," *Power Electronics, IEEE Transactions on,* vol. 28, pp. 2151-2169, 2013.

[79] V. E. I. Corporation, "Electric Vehicle Charging Station Guidebook," 2014.

[80] R. W. Carlson and B. Normann, "Test Results of the PLUGLESS™ Inductive Charging System from Evatran Group, Inc," SAE Technical Paper2014.

[81] A. K. RamRakhyani, S. Mirabbasi, and M. Chiao, "Design and optimization of resonance-based efficient wireless power delivery systems for biomedical implants," *Biomedical Circuits and Systems, IEEE Transactions on*, vol. 5, pp. 48-63, 2011.

[82] C. Park, S. Lee, G.-H. Cho, S.-Y. Choi, and C. T. Rim, "Two-Dimensional Inductive Power Transfer System for Mobile Robots Using Evenly Displaced Multiple Pickups," *Industry Applications, IEEE Transactions on*, vol. 50, pp. 558-565, 2014.

[83] Y. Gao, K. B. Farley, and Z. T. H. Tse, "Investigating safety issues related to Electric Vehicle wireless charging technology," in *Transportation Electrification Conference and Expo (ITEC), 2014 IEEE*, 2014, pp. 1-4.

[84] A. Berger, M. Agostinelli, S. Vesti, J. A. Oliver, J. A. Cobos, and M. Huemer, "A wireless charging system applying phase-shift and amplitude control to maximize efficiency and extractable power," *Power Electronics, IEEE Transactions on*, vol. 30, pp. 6338-6348, 2015.

[85] B. Esteban, M. Sid-Ahmed, and N. C. Kar, "A Comparative Study of Power Supply Architectures in Wireless EV Charging Systems," *Power Electronics, IEEE Transactions on*, vol. 30, pp. 6408-6422, 2015.

[86] A. P. Sample, D. A. Meyer, and J. R. Smith, "Analysis, experimental results, and range adaptation of magnetically coupled resonators for wireless power transfer," *IEEE Transactions on Industrial Electronics*, vol. 58, pp. 544-554, 2011.

[87] V. Jiwariyavej, T. Imura, and Y. Hori, "Coupling Coefficients Estimation of Wireless Power Transfer System via Magnetic Resonance Coupling using Information from Either Side of the System," *Emerging and Selected Topics in Power Electronics, IEEE Journal of*, vol. 3, pp. 191-200, 2015.

[88] C. Zheng, R. Chen, E. Faraci, Z. U. Zahid, M. Senesky, D. Anderson, *et al.*, "High efficiency contactless power transfer system for electric vehicle battery charging," in *Energy Conversion Congress and Exposition (ECCE), 2013 IEEE*, 2013, pp. 3243-3249.

[89] S. Aldhaher, P.-K. Luk, and J. F. Whidborne, "Electronic tuning of misaligned coils in wireless power transfer systems," *Power Electronics, IEEE Transactions on,* vol. 29, pp. 5975-5982, 2014.

[90] J. Han, Y. Kim, and N.-H. Myung, "Efficient performance optimisation of wireless power transmission using genetic algorithm," *Electronics Letters,* vol. 50, pp. 462-464, 2014.

[91] D. Kar, P. Nayak, S. Bhuyan, and S. Panda, "Automatic frequency tuning wireless charging system for enhancement of efficiency," *Electronics Letters,* vol. 50, pp. 1868-1870, 2014.

[92] I. Nam, R. Dougal, and E. Santi, "Novel Unity Gain Frequency Tracking Control of Series-Series Resonant Converter to Improve Efficiency and Receiver Positioning Flexibility in Wireless Charging of Portable Electronics," 2015.

[93] F. W. Grover, *Inductance calculations: working formulas and tables*: Courier Corporation, 1946.

[94] T. C. Beh, M. Kato, T. Imura, S. Oh, and Y. Hori, "Automated impedance matching system for robust wireless power transfer via magnetic resonance coupling," *Industrial Electronics, IEEE Transactions on,* vol. 60, pp. 3689-3698, 2013.

[95] Q. Zhu, Y. Guo, L. Wang, C. Liao, and F. Li, "Improving the Misalignment Tolerance of Wireless Charging System by Optimizing the Compensate Capacitor," *IEEE TRANSACTIONS ON INDUSTRIAL ELECTRONICS,* vol. 62, pp. 4832-4836, 2015.

[96] M. Suma, A. Bohori, R. Somakumar, and A. Raghunathan, "Misalignment-compensated resonant power transfer system," in *Wireless Power Transfer Conference (WPTC), 2015 IEEE*, 2015, pp. 1-4.

[97] S. A. Birrell, D. Wilson, C. P. Yang, G. Dhadyalla, and P. Jennings, "How driver behaviour and parking alignment affects inductive charging systems for electric vehicles," *Transportation Research Part C: Emerging Technologies*, 2015.

[98] A. Ravisankar, A. Agarwal, A. Kulkarni, M. Kumar, B. B. Ram, S. Sivasubramaniam, *et al.*, "A GPS-less Navigation System," in *India Educators' Conference (TIIEC), 2013 Texas Instruments*, 2013, pp. 290-294.

[99] W. Ni, I. B. Collings, X. Wang, R. P. Liu, A. Kajan, M. Hedley, *et al.*, "Radio Alignment for Inductive Charging of Electric Vehicles," *Industrial Informatics, IEEE Transactions on*, vol. 11, pp. 427-440, 2015.

[100] C. Shuwei, L. Chenglin, and W. Lifang, "Research on positioning technique of wireless power transfer system for electric vehicles," in *Transportation Electrification Asia-Pacific (ITEC Asia-Pacific), 2014 IEEE Conference and Expo*, 2014, pp. 1-4.

[101] "Wireless Electric Vehicle Charging - Plugless Power by Evatran Group, Inc," https://www.pluglesspower.com/.

[102] W. Li, H. Zhao, S. Li, J. Deng, T. Kan, and C. C. Mi, "Integrated Compensation Topology for Wireless Charger in Electric and Plug-in Electric Vehicles," *Industrial Electronics, IEEE Transactions on*, vol. 62, pp. 4215-4225, 2015.

[103] Z. Pantic, S. Bai, and S. Lukic, "ZCS-Compensated Resonant Inverter for Inductive-Power-Transfer Application," *Industrial Electronics, IEEE Transactions on*, vol. 58, pp. 3500-3510, 2011.

[104] W. Zhang, J. C. White, A. M. Abraham, and C. C. Mi, "Loosely Coupled Transformer Structure and Interoperability Study for EV Wireless Charging Systems," *Power Electronics, IEEE Transactions on,* vol. 30, pp. 6356-6367, 2015.

[105] L. Chen, G. R. Nagendra, J. T. Boys, and G. A. Covic, "Double-coupled systems for IPT roadway applications," *Emerging and Selected Topics in Power Electronics, IEEE Journal of,* vol. 3, pp. 37-49, 2015.

[106] A. Kamineni, G. A. Covic, and J. T. Boys, "Analysis of Coplanar Intermediate Coil Structures in Inductive Power Transfer Systems," *Power Electronics, IEEE Transactions on,* vol. 30, pp. 6141-6154, 2015.

[107] Y. Gao, A. A. Oliveira, K. B. Farley, and Z. T. H. Tse, "Magnetic Alignment Detection Using Existing Charging Facility in Wireless EV Chargers," *Journal of Sensors*, vol. 501, p. 5670510, 2016.

[108] A. K. Lewis and M. Naserian, "Utilizing dedicated short range communications (DSRC) in high power grid connected electric drive vehicle (GCEDV) wireless charging applications," in *Connected Vehicles and Expo (ICCVE), 2014 International Conference on*, 2014, pp. 416-420.

[109] H. Jabbar, Y. S. Song, and T. T. Jeong, "RF energy harvesting system and circuits for charging of mobile devices," *Consumer Electronics, IEEE Transactions on*, vol. 56, pp. 247-253, 2010.

[110] N. Liu and T. G. Habetler, "A study of designing a universal inductive charger for Electric Vehicles," in *Industrial Electronics Society, IECON 2013-39th Annual Conference of the IEEE*, 2013, pp. 4528-4533.

[111] T. Imura, T. Uchida, and Y. Hori, "Flexibility of contactless power transfer using magnetic resonance coupling to air gap and misalignment for EV," *World Electric Vehicle Journal,* vol. 3, pp. 24-34, 2009.

[112] C. Duan, W. Guo, K. H. Bai, Z. Nie, M. Zhang, F. Householder, *et al.*, "Design of a 2.5 kW 400V→ M2V high-efficiency DC/DC converter using a novel synchronous rectification control for electric vehicles," in *Energy Conversion Congress and Exposition (ECCE), 2013 IEEE*, 2013, pp. 1082-1086.

[113] Z. Nie, W. D. Williams, C. Duan, W. Guo, and K. H. Bai, "System optimization of a high-power and high-step-down accessory power module for electric vehicles," in *Applied Power Electronics Conference and Exposition (APEC), 2014 Twenty-Ninth Annual IEEE*, 2014, pp. 1926-1931.

[114] A. Y. Saber and G. K. Venayagamoorthy, "One million plug-in electric vehicles on the road by 2015," in *Intelligent Transportation Systems, 2009. ITSC'09. 12th International IEEE Conference on*, 2009, pp. 1-7.

[115] Y. Hori, "Future vehicle society based on electric motor, capacitor and wireless power supply," in *Power Electronics Conference (IPEC)*, 2010, pp. 2930-2934.

[116] S. Chopra and P. Bauer, "Driving range extension of EV with on-road contactless power transfer—A case study," *Industrial Electronics, IEEE Transactions on,* vol. 60, pp. 329-338, 2013.

[117] H. Jiang, P. Brazis, M. Tabaddor, and J. Bablo, "Safety considerations of wireless charger for electric vehicles—A review paper," in *Product Compliance Engineering (ISPCE), 2012 IEEE Symposium on*, 2012, pp. 1-6.

[118] H. Jiang, W. Li, M. Tabaddor, and C. Mi, "Optimization and safety evaluation of a 3.3 kW wireless EV charger," in *Transportation Electrification Conference and Expo (ITEC), 2015 IEEE*, 2015, pp. 1-5.

[119] A. R. Protection, "Nuclear Safety Agency (ARPANSA) 2002," *Recommendations for limiting exposure to ionizing radiation (1995)*, 2006.

[120] M. Budhia, G. A. Covic, and J. T. Boys, "Design and optimization of circular magnetic structures for lumped inductive power transfer systems," *Power Electronics, IEEE Transactions on*, vol. 26, pp. 3096-3108, 2011.

[121] J. Boys, G. Covic, and A. W. Green, "Stability and control of inductively coupled power transfer systems," *IEE Proceedings-Electric Power Applications*, vol. 147, pp. 37-43, 2000.

[122] C.-S. Wang, G. A. Covic, and O. H. Stielau, "General stability criterions for zero phase angle controlled loosely coupled inductive power transfer systems," in *Industrial Electronics Society, 2001. IECON'01. The 27th Annual Conference of the IEEE*, 2001, pp. 1049-1054.

[123] "Guidelines for Limiting Exposure to Time-Varying Electric, Magnetic, and Electromagnetic Fields (Up to 300 GHz)," *Health Physics* vol. 74, pp. 494-522, 1998.

[124] "Guidelines for limiting exposure to time-varying electric, magnetic and electromagnetic fields (1 kHz to 100 kHz)," *Health Physics*, vol. 99, pp. 818-836, 2010.

[125] S. Obayashi and H. Tsukahara, "EMC issues on wireless power transfer," in *Electromagnetic Compatibility, Tokyo (EMC'14/Tokyo), 2014 International Symposium on*, 2014, pp. 601-604.

[126] R. P. Standard, "Maximum Exposure Levels to Radiofrequency Fields—3 KHz to 300 GHz," *Radiation Protection Series*.

[127] C. Durney, M. Iskander, H. Massoudi, and C. Johnson, "An empirical formula for broad-band SAR calculations of prolate spheroidal models of humans and animals," *Microwave Theory and Techniques, IEEE Transactions on*, vol. 27, pp. 758-763, 1979.

[128] S. Fukuda, H. Nakano, Y. Murayama, T. Murakami, O. Kozakai, and K. Fujimaki, "A novel metal detector using the quality factor of the secondary coil for wireless power transfer systems," in *Microwave Workshop Series on Innovative Wireless Power Transmission: Technologies, Systems, and Applications (IMWS), 2012 IEEE MTT-S International*, 2012, pp. 241-244.

[129] S. Verghese, M. P. Kesler, K. L. Hall, and H. T. Lou, "Foreign object detection in wireless energy transfer systems," ed: Google Patents, 2012.